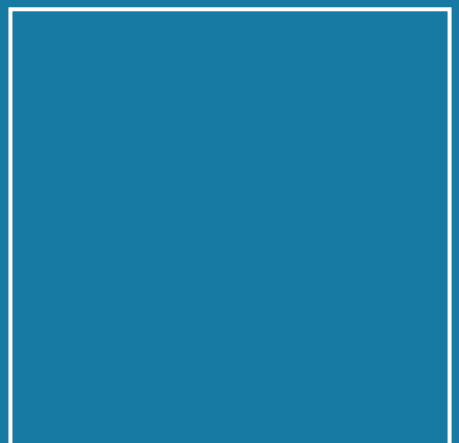
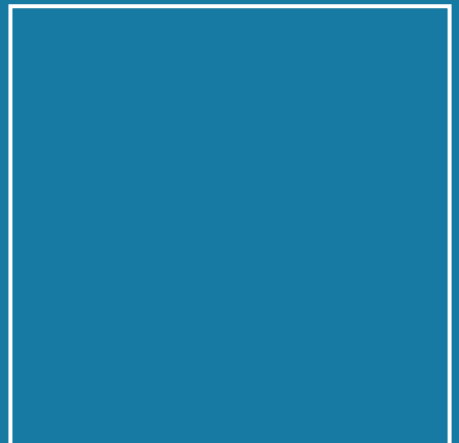




Dissertation

Richard Lange

High-Precision Frequency Comparisons and Searches for New Physics with Yb^+ Optical Clocks



ISSN 0341-6712
ISBN 978-3-95606-623-8

Physikalisch-Technische Bundesanstalt

Optik

PTB-Opt-93

Braunschweig, September 2021

Richard Lange

High-Precision Frequency Comparisons and Searches for New Physics with Yb⁺ Optical Clocks

Herausgeber:

Physikalisch-Technische Bundesanstalt

ISNI: 0000 0001 2186 1887

Presse und Öffentlichkeitsarbeit

Bundesallee 100

38116 Braunschweig

Telefon: (05 31) 592-93 21

Telefax: (05 31) 592-92 92

www.ptb.de

High-Precision Frequency
Comparisons and
Searches for New Physics
with Yb^+ Optical Clocks

Von der Fakultät für Mathematik und Physik
der Gottfried Wilhelm Leibniz Universität Hannover

zur Erlangung des akademischen Grades
Doktor der Naturwissenschaften
Dr. rer. nat.

genehmigte Dissertation von

Richard Lange, M.Sc.

2021

Referent: PD Dr. Ekkehard Peik
Korreferent: Prof. Dr. Piet O. Schmidt
Korreferent: Assoc. Prof. Dr. Hartmut Häffner
Tag der Promotion: 30.06.2021

Abstract

State-of-the-art optical atomic clocks are based on laser-cooled trapped atoms or ions featuring forbidden transitions. A laser with sub-Hertz linewidth is frequency stabilized to such a transition, which permits frequency measurements with relative systematic uncertainties in the low 10^{-18} range. The performance of optical atomic clocks is continuously improved by more efficient detection and suppression of external perturbations that cause shifts of the atomic transition frequency, and by enhancing the coherent interaction between atom and laser oscillator.

In this thesis, advances of the $^{171}\text{Yb}^+$ single-ion optical clocks at the national metrology institute of Germany (PTB) are reported, realizing the frequencies of both an electric quadrupole (E2) and an electric octupole (E3) transition. Two Yb^+ (E3) clocks are compared and an agreement within their combined fractional uncertainty of 4.2×10^{-18} is found. An analysis of the data for potential frequency oscillations improves the limits on Lorentz violating parameters for electrons by about two orders of magnitude. A long-term comparison of the E3/E2 transition frequency ratio tightens the limit on potential temporal variations of the fine structure constant α by about a factor of 20 to $(1/\alpha)(d\alpha/dt) = 1.0(1.1) \times 10^{-18}/\text{yr}$. Comparisons of an Yb^+ (E3) clock and two caesium fountain clocks yields $\nu_{\text{E3}} = 642\,121\,496\,772\,645.10(8)$ Hz, the most accurate determination of an optical transition frequency to date.

Relevant atomic parameters of the E3 transition are investigated in more detail: From the transition strength and laser intensity, the excited state natural lifetime is determined as 1.58(7) years. For a characterization of the light shift of the E3 transition, the zero-crossing point of the scalar differential polarizability is measured at 681.2(5) nm, which is called a magic wavelength. Precision measurements of the electric quadrupole moments of the excited states of both the E2 and E3 transition, $\Theta(^2\text{D}_{3/2}) = 1.95(1)ea_0^2$ and $\Theta(^2\text{F}_{7/2}) = -0.0297(5)ea_0^2$, with e the elementary charge and a_0 the Bohr radius, indicate the different electronic structure of the excited states and the different sensitivities of the two transitions to shifts induced by electric field gradients.

The characterization of an advanced single-ion Yb^+ trap system employing gold-coated endcap electrodes is presented. A reduction of the ion motional heating rate by a factor of 25 compared to previous trap versions is obtained, facilitating longer interaction times between ion and laser. First frequency comparisons to the other Yb^+ clocks at PTB yield agreements at the low 10^{-17} level, presumably limited by photoelectric stray fields.

Novel interrogation methods for the control or suppression of specific frequency shifts are discussed: A coherent suppression scheme for tensorial frequency shifts is introduced, relying on a rotation of the magnetic field vector during the dark time of a Ramsey sequence, and a suppression of the electric quadrupole shift by a factor of 260 is demonstrated. Autobalanced Ramsey spectroscopy is presented that provides universal immunity to frequency shifts related to aberrations of the pulses in a Ramsey sequence. Finally, excitation of an E3 transition using twisted light, i.e. with the ion placed in the dark center of a Laguerre-Gaussian beam featuring orbital angular momentum, is demonstrated for the first time, permitting a reduction of the light shift.

Key words: optical frequency standard, precision spectroscopy, local Lorentz invariance, local position invariance, natural lifetime, magic wavelength, twisted light

Contents

1	Atomic clocks in a nutshell	1
1.1	The main ingredients	2
1.2	A clock's performance: Accuracy and stability	5
1.3	Current state-of-the-art	6
1.4	Building an ion clock	8
1.4.1	Trapping an ion	8
1.4.2	Laser spectroscopy of a trapped particle	13
1.4.3	Cooling a trapped ion	15
1.4.4	Spectroscopy on clock transitions	19
1.4.5	A stable laser source	21
1.4.6	Spectroscopy sequence	22
1.5	The ion of choice	25
1.6	$^{171}\text{Yb}^+$ ion clocks at PTB: A status report	27
2	Yb3 - A new clock with reduced uncertainty	29
2.1	Trap setup and clock control	31
2.2	opticlock - the industrial twin	36
2.3	Evaluation of the uncertainty contributions	37
2.3.1	Quadratic Stark shift	37
2.3.2	Blackbody radiation shift	38
2.3.3	Second-order Doppler and quadratic dc Stark shift	43
2.3.4	Ion motion	45
2.3.5	Variation of dc electric fields	52
2.3.6	Second-order dc Zeeman shift	54
2.3.7	Second-order ac Zeeman shift	57
2.3.8	Electric quadrupole shift	59

2.3.9	Background gas collisions	63
2.3.10	Gravitational redshift	66
2.3.11	Probe shifts	67
2.3.12	Uncertainty budget	70
2.4	Evaluation of the frequency instability	71
2.4.1	Comparison of Yb1 and Yb3	71
2.4.2	Probe light stabilization with a reference fiber	75
3	Clock comparisons and searches for new physics	79
3.1	Experimental infrastructure	81
3.2	Direct comparison of the E3 transition and test of local Lorentz invariance	84
3.3	Measurement of the E3/E2 transition ratio and test of α variation	89
3.4	Absolute frequency measurement of the E3 transition and test of μ variation	93
3.5	Frequency ratio of $^{171}\text{Yb}^+$ and ^{87}Sr	96
3.6	Spectroscopy of the $^2\text{F}_{7/2}$ $F = 3$ to $F = 4$ hyperfine transition .	98
3.7	Yb3 measurements	101
4	Advanced interrogation methods	107
4.1	Magnetic field rotation for coherent suppression of tensor frequency shifts	108
4.2	Autobalanced Ramsey spectroscopy	113
4.3	Towards light shift-suppressed sympathetic cooling: Magic wavelength measurement	116
4.4	E3 transition light shift and $^2\text{F}_{7/2}$ state lifetime	121
4.5	Excitation of the E3 transition using twisted light	124
4.5.1	Generation of vortex beams	125
4.5.2	Light shift suppression	129
4.5.3	Angular dependence of the excitation probability	130
5	Summary and outlook	133

Chapter 1

Atomic clocks in a nutshell

The measurement of periodic events, or frequencies, has a long tradition in the history of mankind, dating back to the earliest reports on calendars. Today, frequencies are the most accurately measurable physical quantities. For instance, the SI unit second is realized with 16 digits of accuracy, outperforming the second most accurate SI unit meter by five orders of magnitude [1]. The precision reached in frequency measurements enables the search for new physics such as dark matter with low-energy tabletop experiments, which compete in this endeavor with city-sized facilities for high-energy particle physics [2]. In the pursuit of improving accuracy, stability, robustness and scalability of frequency standards even further, many different research areas related to the control and manipulation of quantum systems are rapidly progressing. One of the most prominent examples is the field of quantum computers, which nowadays are on the verge of outperforming their classical counterparts [3, 4].

At the heart of measuring frequencies with highest accuracy, there are atomic clocks. Since the first caesium clock was brought into service in 1955, they have become an essential part of today's global infrastructure. Not only the realization of various time scales, but also global navigation satellite systems, telecommunication and trading rely on frequencies provided by atomic clocks. To gain an insight into this comprehensive field of study, the principles and different types of atomic clocks will be discussed within this introduction, before focusing on a specific atomic species for the rest of the thesis.

1.1 The main ingredients

To build any kind of clock, three ingredients are needed. It all starts with a *periodically repeating event* provided for example by an oscillator, such as a pendulum reaching its maximum angular displacement. A *counter* records each event and keeps track of the number of cycles that have passed, turning the periodic into an incremental signal. Finally, the oscillator frequency needs to be controlled by a *universal reference* to enable the coordination of time scales and the meaningful comparison of different clocks.

For most of human history, astronomical observations provided this universal reference and formed the basis for timekeeping. This includes assessment of the Earth's rotation, for example directly readable from sun dials, or its orbital motion around the Sun, leading to the definition of ephemeris time [5]. In fact, even today's time scales acknowledge astronomical effects by introducing leap seconds and days. But already long before the advent of atomic clocks, the need for more fundamental references that “keep their significance for all times and for all [...] cultures” had been raised by Max Planck in 1900 [6]. In 1967, this idea was implemented by referencing the second to the ground state hyperfine splitting of the ^{133}Cs atom, and in 2019 it was extended to the other SI base units.

The basic idea of the atomic clock is shown in figure 1.1 (A). With the reference provided by a microwave transition as in the case of caesium clocks, a microwave signal generated by the local oscillator, in this case a quartz crystal, is used to probe a cloud of ^{133}Cs atoms. The reference transition, in the following also referred to as clock transition, needs to be measured with high accuracy. In particular, this requires a small width of the transition line and in turn a long lifetime of the excited clock transition state. With coherent interrogation between atoms and local oscillator, a discriminator signal is generated that is fed back to the oscillator for closed-loop control. Using electronics, the oscillator signal can be converted to a different frequency, for example to produce a pulse-per-second signal.

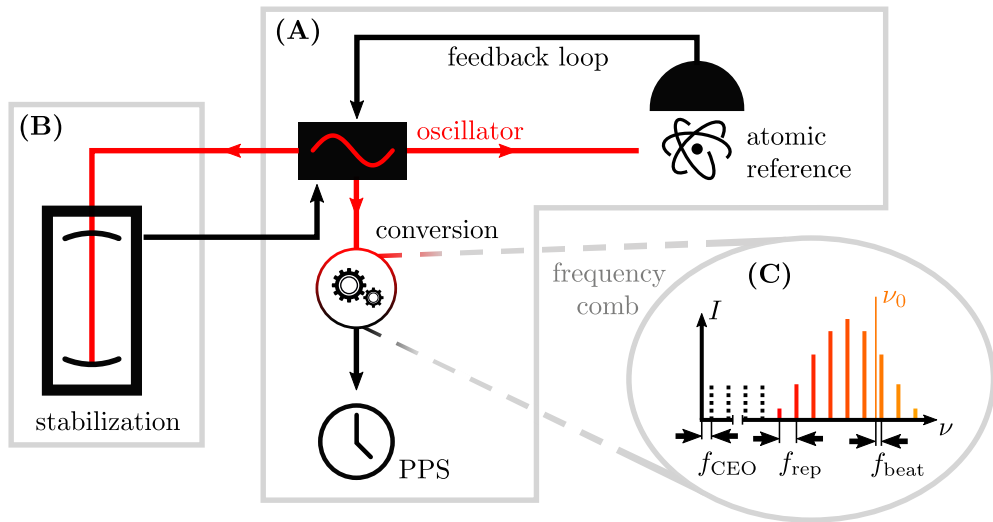


Figure 1.1: **Principle of an atomic clock.** (A) An atomic reference is interrogated by the radiation from an oscillator (e.g. a quartz crystal or a laser) and the spectroscopic signal is used to control the oscillator in a closed loop. The frequency of the oscillator can be converted, for example to provide a pulse-per-second (PPS) signal. (B) For an optical atomic clock employing a laser as the oscillator to interrogate the atomic transition, the laser frequency is stabilized to an optical cavity with high finesse in order to provide a small laser linewidth of below 1 Hz. (C) For an optical atomic clock, the laser frequency needs to be downconverted to an electronically countable signal using a frequency comb that provides several comb teeth, a discrete spectrum of equally spaced frequencies in the optical regime. The frequencies have a spacing f_{rep} and the lowest frequency has an offset to zero f_{CEO} . Measuring the beat frequency f_{beat} between the oscillator frequency ν_0 and the closest comb tooth, the absolute frequency of the oscillator can be extracted.

This general concept, controlling a local oscillator through coherent interrogation of a reference transition, is inherent to all atomic clocks, but there is large variety in the atomic species used as the reference. Profiting from developments in laser technology, in particular from the development of optical frequency combs, a new class called optical atomic clocks has emerged within the last thirty years. Here, an ultrastable laser (clock laser) is used as the local oscillator to probe clock transitions that feature five orders of magnitude higher frequencies compared to microwave transitions. To achieve narrow-linewidth excitation of the clock transition, the laser frequency is stabilized with an optical high-finesse cavity as shown in figure 1.1 (B). Furthermore, the atoms are tightly confined to avoid Doppler broadening of the reference transition, typically by removing kinetic energy on a fast-cycling, so-called cooling transition. This transition is electric dipole-allowed and typically has a linewidth of several MHz. To avoid trapping in a longer living state, additional lasers are employed to return the atom to the cooling cycle on the cooling transition.

While optical signals can not be processed directly with electronics, frequency combs provide access to the absolute laser frequencies [7] as shown in figure 1.1 (C). The most popular comb version relies on a precisely timed train of laser pulses generated by a mode-locked laser, resulting in a discrete frequency spectrum in the optical regime with constant spacing of a few hundred MHz between the comb teeth. The frequency spacing f_{rep} is determined by the repetition rate. The zero-offset f_{CEO} of the (virtual) peak closest to zero is commonly known as carrier-envelope offset (CEO) resulting from phase- and group-velocity differences induced by dispersion, and it is assessed by comparing part of the spectrum to its harmonic (self-referencing). The difference f_{beat} between the clock transition frequency ν_0 and the frequency of a specific comb tooth is found in a beat measurement. Using the equation

$$\nu_0 = m f_{\text{rep}} + f_{\text{CEO}} + f_{\text{beat}} \quad (1.1)$$

with m the number of teeth from zero to the one used for the beat, ν_0 can be measured only relying on the electronically processable radio frequency signals f_{rep} , f_{CEO} and f_{beat} .

1.2 A clock's performance: Accuracy and stability

There are two main features that characterize an atomic clock: accuracy and stability. Accuracy describes how well the unperturbed transition frequency can be realized, taking into account that external perturbations cause frequency shifts. These shifts and their uncertainties are summarized in an uncertainty budget. Comparing two clocks employing the same atomic transition to test their agreement, the individual shifts and uncertainties are taken into account. Possible common-mode shift effects also need to be considered.

Stability describes how the statistical uncertainty of the transition frequency evolves over time and is commonly analyzed in the comparison of the clock frequency to the frequency of an oscillator with equal or better stability using the Allan deviation [8]. If two clocks probe the transition frequency ν_0 , the fractional frequency differences $y_k = (f_1 - f_2)/\nu_0$ for frequencies f_1 and f_2 of clock 1 and 2 are measured for non-overlapping time intervals $[k\tau, (k+1)\tau)$, with τ the length of the interval. It is assumed that there is no dead time between successive intervals. If different transition frequencies ${}^1\nu_0$ and ${}^2\nu_0$ are probed, the relative frequency ratio $y_k = \frac{f_1/f_2}{{}^1\nu_0/{}^2\nu_0}$ is observed. The clock stability is given by analyzing the time intervals using the Allan deviation

$$\sigma_y(\tau) = \sqrt{\frac{1}{2M-1} \sum_{k=1}^{M-1} (y_{k+1} - y_k)^2}. \quad (1.2)$$

Depending on the type of noise, the scaling characteristics for the Allan deviation are different. The most important cases for the analysis of atomic clock data are listed here:

White frequency noise yields $\sigma_y(\tau) \propto 1/\sqrt{\tau}$ and is exhibited for uncorrelated measurements. It describes random frequency excursions of a signal with equal amplitude on all frequencies. For optical atomic clock comparisons with individual, uncorrelated interrogations of the atom, this is the typical noise observed on timescales larger than the bandwidth of the atomic signal feedback loop, which is on the order of 10 s to 100 s. Individual measurement periods separated by breaks can be combined

into a single data set, assuming that they are uncorrelated.

White phase noise yields $\sigma_y(\tau) \propto 1/\tau$. It describes random phase excursions of a signal with equal amplitude on all frequencies. It can only be measured as long as the phase information is preserved, i.e. while the signal is tracked continuously without missing any cycles, such as during the atom-oscillator interaction within the Ramsey dark time.

Flicker frequency noise yields $\sigma_y(\tau) \propto 1$, i.e. the Allan deviation is constant. It describes excursions of a signal with random frequency f , for which the amplitude decreases with $1/f$ in the frequency spectrum. This is observed on timescales of seconds to several minutes for a laser locked to a reference cavity that is subject to thermal noise [9].

Frequency drifts yield $\sigma_y(\tau) \propto \tau$, as experienced for the lasers locked to a reference cavity that shows a constant change in length due to a temperature drift.

In most cases, the stability of atomic clocks is limited by quantum projection noise [10] that leads to white frequency noise behavior of the clock's stability.

1.3 Current state-of-the-art

There is a large variety of atomic species suitable for the realization of an optical atomic clock, with very different strengths and weaknesses: accessibility of clock and cooling transitions, immunity to external perturbations, sensitivity in searches for new physics, and lifetime of the clock state are just a few aspects of relevance in characterizing an atomic clock [11]. Two main approaches for optical atomic clocks are pursued: While lattice clocks operate with thousands of neutral atoms in an optical dipole trap, ion clocks rely on only a few particles trapped by a radio frequency electric field. Both types are realized by research facilities all over the world. An overview over the most advanced systems that have been evaluated to a relative uncertainty below 10^{-17} is presented in table 1.1, together with relative frequency differences and ratios obtained employing these clocks, with uncertainties in the 10^{-17} range and below.

Recently, the most accurate comparison of two different atomic species has been performed in the United States at the National Institute of Standards

and Technology (NIST) in Boulder, Colorado, with both an Yb lattice and an Al⁺ ion clock [12]. The measurements have been performed together with JILA, located in Boulder as well and operating Sr lattice clocks. Sr is also investigated in Japan at the RIKEN institute [13]. Several other groups are working with lattice clocks based on Sr [14–16] and Yb [17–19], and ion clocks based on Al⁺ [20], Sr⁺ [21] and Yb⁺ [22]. Many additional promising clock candidates such as Lu⁺ [23], In⁺ [24], Hg [25], Mg [26], Ca⁺ [27] or Tm [28] are pushed towards the same accuracy regime; the large number of research groups investigating various optical atomic clock candidates illustrates that this is an innovative and comprehensive field of research far too extensive to be dealt with in every detail within this thesis. Therefore, the following discussions are focused on the ¹⁷¹Yb⁺ single-ion clocks operated at the Physikalisch-Technische Bundesanstalt (PTB) in Germany.

year	institute	system	$\frac{u_{\text{sys}}}{\nu_0}$	$\frac{\Delta\nu}{\nu_0} \left(\frac{u_{\text{tot}}}{\nu_0} \right)$	$\frac{u_{\text{tot}}}{R_0}$	ref.
2010	NIST	Al ⁺	8.6	18(25)		[29]
2014	JILA	Sr	6.4	28(54)		[30]
2015	RIKEN	Sr	7.2	1.1(4.7)		[31]
2015	JILA	Sr	2.1			[32]
2016	PTB	Yb ⁺ (E3)	3.2			[33]
2016	RIKEN	Yb/Sr	35/5.8		46	[34]
2018	NIST	Yb	1.4	0.7(0.9)		[35]
2019	PTB	Yb ⁺ (E3)	2.7	2.8(4.2)		[36]
2019	NIST	Al ⁺	0.9			[37]
2020	RIKEN	Sr	5.5	0.3(4.7)		[13]
2021	NIST, JILA	Al ⁺ /Yb	1.7/1.4		5.9	[12]
2021	NIST, JILA	Yb/Sr	1.4 /5.0		6.8	[12]
2021	NIST, JILA	Al ⁺ /Sr	1.5/4.8		8.0	[12]
2021	PTB	Yb ⁺ (E3)/Sr	2.7/15		25	[38]
2021	PTB	Yb ⁺ (E3/E2)	2.7/33		34	[39]

Table 1.1: **Optical clock performances at the 10⁻¹⁸ level.** State-of-the-art optical clock systems with relative systematic uncertainties u_{sys}/ν_0 below 10⁻¹⁷ are listed. In case of a frequency ratio measurement, also the systematic uncertainty of the second clock is given. Relative frequency differences $\Delta\nu/\nu_0$ and corresponding uncertainties u_{tot}/ν_0 of are shown for comparisons of two systems employing the same transition. Relative uncertainties u_{tot}/R_0 of frequency ratios are obtained if two different transitions are compared. For Yb⁺, two clock transitions (E2 and E3) are used. All values are given in 10⁻¹⁸.

1.4 Building an ion clock

This section provides a broad overview over the main elements needed to operate an optical ion clock, including trapping in an electromagnetic potential, cooling the ion, exciting different atomic transitions and providing a stable laser for precision spectroscopy. The explanations are supported by a few mathematical derivations that mainly follow the approaches presented in the literature [8, 40–42], where the individual topics are discussed in greater detail. Special attention is paid to estimates in the context of Yb^+ for the variables derived here in order to give an idea about the size of important parameters.



Such a box indicates an explicit example for a formula or variable just derived. The values used are always geared towards the single-ion $^{171}\text{Yb}^+$ experiments described within this thesis, in particular by choosing the ion mass $m = m_{\text{Yb}} = 171u$ (u the unified atomic mass unit) and the charge $Q = e$ (elementary charge).

1.4.1 Trapping an ion

To investigate a single ion in a well controlled environment, it first needs to be trapped. The electric charge of the ion facilitates trapping in electric fields. According to the Laplace equation

$$\Delta\Phi = \frac{\partial^2\Phi}{\partial^2x} + \frac{\partial^2\Phi}{\partial^2y} + \frac{\partial^2\Phi}{\partial^2z} = 0 \quad (1.3)$$

for an electric potential Φ , there is no static electric field $\mathbf{E} = \nabla\Phi$ that provides an attractive force $\mathbf{F}(r_i) = q\mathbf{E}(r_i)$ for all directions r_i , $i \in x, y, z$, simultaneously. Instead, the trapping field is generated using an oscillating potential of the form

$$\Phi(t) = (U + V \cos(\Omega_{\text{rf}}t)) \frac{(1 + \epsilon)r_x^2 + (1 - \epsilon)r_y^2 - 2r_z^2}{\kappa} \quad (1.4)$$

with U and V the amplitude of the constant and the radio frequency (rf) voltage, Ω_{rf} the oscillation frequency, and ϵ the deviation from cylindrical symmetry around the z axis. The trap-dependent dimension $\kappa = -d_0^2/\zeta$ is related to

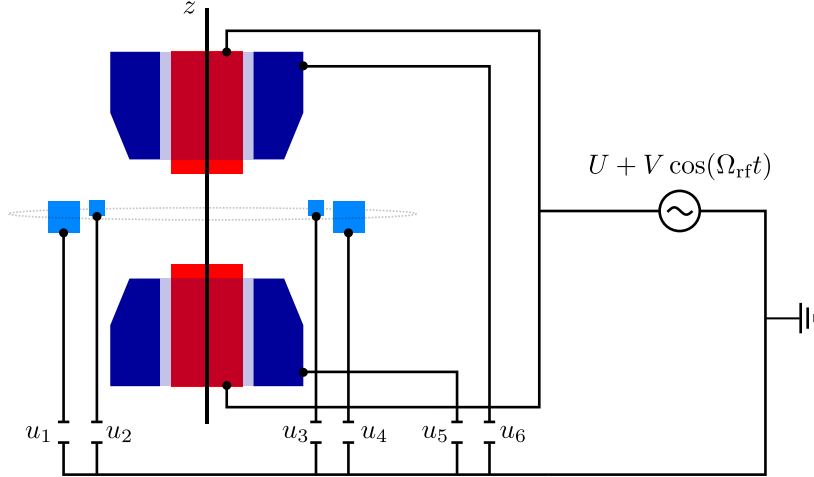


Figure 1.2: **Schematic of the rf endcap trap design.** The red and dark blue rf electrodes are rotationally symmetric around the z axis and are connected to the voltage V oscillating at the trap drive frequency Ω_{rf} . A constant voltage U supplied to the rf electrodes changes the electric potential according to equation (1.4). Additionally, there are four compensation electrodes in the xy -plane, at equal distance to each other and symmetric around the trap center (illustrated by the gray dotted ring). Employing the voltages u_1 to u_6 , changes of the ion equilibrium position due to stray electric fields can be compensated.

the distance d_0 of the electrodes on the z -axis, with $\zeta \leq 1$. For the original Paul trap design [43] using electrodes matching a hyperbolic equipotential surface, $\zeta = 1$ and $\kappa = -d_0^2$ [44]. For commonly employed traps with simplified electrode geometries, the potential is well described by equation (1.4) only near the nodal point and $0.2 \lesssim \zeta \lesssim 0.9$. The endcap trap design with $\zeta \approx 0.7$ [44] in figure 1.2 is an example of such a simplified trap geometry. The equations of motion of a charged particle moving in the potential $\Phi(t)$ are of the form of Mathieu equations [45]. Solutions of these equations can be expressed by

$$\begin{aligned}
 r_i(t) &= (r_{e,i} + r_{0,i} \cos(\omega_i t + \phi_i)) \left(1 + \frac{q_i}{2} \cos(\Omega_{\text{rf}} t) \right) \\
 &= \underbrace{r_{e,i}}_{\text{ion position}} + \underbrace{r_{0,i} \cos(\omega_i t + \phi_i)}_{\text{secular motion}} + \underbrace{r_{0,i} \cos(\omega_i t + \phi_i) \frac{q_i}{2} \cos(\Omega_{\text{rf}} t)}_{\text{intrinsic micromotion}} + \underbrace{r_{e,i} \frac{q_i}{2} \cos(\Omega_{\text{rf}} t)}_{\text{excess micromotion}}.
 \end{aligned} \tag{1.5}$$

The ion motion depends on two frequencies. The secular motion is determined by the secular frequency¹ ω_i ,

$$\omega_i = \frac{\Omega_{\text{rf}}}{2} \sqrt{a_i + \frac{q_i^2}{2}}. \quad (1.6)$$

The two variables a_i and q_i are called stability parameters of the trap. They can be expressed by [47]

$$a_i = \frac{8\alpha_i Q U}{m\kappa\Omega_{\text{rf}}^2}, \quad (1.7)$$

$$q_i = -\frac{4\alpha_i Q V}{m\kappa\Omega_{\text{rf}}^2}, \quad (1.8)$$

with $\alpha_x = 1 + \epsilon$, $\alpha_y = 1 - \epsilon$, $\alpha_z = -2$, and Q the ion charge. Equation (1.5) is valid under the assumption that $|a_i| \ll q_i \ll 1$, i.e. the potential is switching fast compared to the ion motion and no large dc fields are distorting the rf potential. The second relevant frequency for the ion motion is called micromotion frequency Ω_{rf} . The micromotion splits into the intrinsic part directly coupled to the secular motion, and an excess micromotion proportional to the distance $r_{e,i}$ of the ion from the trap center. The ion displacement arises from stray electric fields, for example due to patch charges on the trap surface, and the excess micromotion can be minimized by applying dc electric fields to compensating electrodes as shown in figure 1.2.



With $\Omega_{\text{rf}} = 2\pi \times 13$ MHz, $V = 500$ V and $\kappa = -1$ mm², one finds $q_x \approx 0.17$. Typically $U = 0$ and accordingly $a_x = 0$. This results in $\omega_x \approx 2\pi \times 778$ kHz and $\omega_z = 2\omega_x$. U can be changed from about +20 V to about -40 V, outside of this region one of the sideband frequencies quickly goes to zero and becomes imaginary. With a small sideband frequency corresponding to a low trap potential along that axis, the ion does not remain trapped.

¹Equation (1.6) is an approximation valid for $|a_i|, q_i \ll 1$. A more general expression is given in [46].

The average kinetic energy along one direction due to the ion motion can be calculated from equation (1.5):

$$E_{\text{kin},i} = \frac{1}{2}m \langle \dot{r}_i^2 \rangle = \frac{1}{4}mr_{0,i}^2 \left(\omega_i^2 + \frac{1}{8}q_i^2\Omega_{\text{rf}}^2 \right) + \frac{1}{16}mr_{e,i}^2q_i^2\Omega_{\text{rf}}^2 \quad (1.9)$$

$$= \frac{1}{4}mr_{0,i}^2\omega_i^2 \left(1 + \frac{q_i^2}{q_i^2 + 2a_i} \right) + \frac{1}{16}mr_{e,i}^2q_i^2\Omega_{\text{rf}}^2. \quad (1.10)$$

Using the relation [48]

$$k_B T_i = \frac{1}{2}mr_{0,i}^2\omega_i^2, \quad (1.11)$$

the approximation $a_i \ll q_i$, and writing the excess micromotion in terms of its amplitude $a_{e,i} = r_{e,i}q_i/2$, this can be further simplified to

$$E_{\text{kin},i} = \frac{1}{2}k_B T_i + \frac{1}{2}k_B T_i + \frac{1}{4}ma_{e,i}^2\Omega_{\text{rf}}^2. \quad (1.12)$$

It is worth stressing again that the first term is related to secular motion, the second term to intrinsic and the third to excess micromotion. When specifying the ion temperature, for example the Doppler temperature as discussed in section 1.4.3, the contribution to the energy due to excess micromotion is not considered. The total mean kinetic energy takes the form

$$E_{\text{kin}} = \sum_i k_B T_i + \frac{1}{4}ma_{e,i}^2\Omega_{\text{rf}}^2. \quad (1.13)$$

This equation will be used for the derivation of the uncertainty contribution due to ion motion in section 2.3.4.

A different approach for the treatment of the ion energy can be followed by taking the average position on timescales larger than $1/\Omega_{\text{rf}}$, for which the micromotion oscillation vanishes, and having the ion not displaced ($r_{e,i} = 0$). In this case equation (1.5) can be simplified to

$$r_i(t) = r_{0,i} \cos(\omega_i t + \phi_i), \quad (1.14)$$

which is the motion of a harmonic oscillator in the pseudo-potential of the trap with energy

$$E_{\text{pot}} = \sum_i \frac{m}{2} \omega_i^2 r_i^2. \quad (1.15)$$



For the trap depth $D(d_0/2) = E_{\text{pot}}(d_0/2)$ with distance d_0 between the endcap electrodes, one finds $D(d_0/2) \approx 21$ eV with $\omega_z = 2\pi \times 1556$ kHz and $d_0 = 1$ mm. This is much larger than the kinetic energy of an atom evaporated from a sample: From a Maxwell-Boltzmann distribution, the mean thermal velocity $\langle v \rangle = \sqrt{(8k_B T)/(\pi m)}$ can be calculated. With $T \approx 600$ K, one finds $\langle v \rangle \approx 270$ m/s and $E_{\text{kin}} < 100$ meV. Thus for the given trap depth, an ion can be trapped reliably after ionization.

The trapped ion can now be described by the standard harmonic oscillator Hamiltonian of the form

$$H_{\text{HO}} = \sum_i \frac{p_i^2}{2m} + \frac{1}{2} m \omega_i^2 r_i^2 = \sum_i \hbar \omega_i \left(a_i^\dagger a_i + \frac{1}{2} \right) \quad (1.16)$$

where a_i^\dagger and a_i are the creation and annihilation operators that follow

$$r_i = \sqrt{\frac{\hbar}{2m\omega_i}} (a + a^\dagger), \quad p_i = i\sqrt{\frac{\hbar m \omega_i}{2}} (a^\dagger - a),$$

$$a^\dagger a |n\rangle = n |n\rangle, \quad a^\dagger |n\rangle = \sqrt{n+1} |n+1\rangle, \quad a |n\rangle = \sqrt{n} |n-1\rangle.$$

The reduced Planck constant is defined as $\hbar = h/2\pi$, with h the Planck constant, and the energy eigenstate $|n\rangle$ has the quantum number n . The energy of the harmonic oscillator is given by

$$E_{\text{HO}} = \sum_i \hbar \omega_i \left(n_i + \frac{1}{2} \right). \quad (1.17)$$

The spatial expectation value, corresponding to the spread of the ground state wave packet, is given by

$$r_{0,i} = \sqrt{\langle 0 | r_i^2 | 0 \rangle} = \sqrt{\frac{\hbar}{2m\omega_i}}. \quad (1.18)$$



For the ion in the ground state and with $\omega_x = 2\pi \times 778$ kHz, one finds $r_{0,x} \approx 6$ nm.

1.4.2 Laser spectroscopy of a trapped particle

Having the ion trapped, the next step is to gain control over it [40, 41]. To do so, it is exposed to an electromagnetic field (with amplitude E_0) of the form

$$\mathbf{E}(\mathbf{r}, t) = E_0 \boldsymbol{\epsilon} \left(e^{i(\mathbf{k}\mathbf{r} - \omega_L t + \phi_L)} + e^{-i(\mathbf{k}\mathbf{r} - \omega_L t + \phi_L)} \right) \quad (1.19)$$

provided by a laser with polarization $\boldsymbol{\epsilon}$, wave vector \mathbf{k} , angular frequency $\omega_L = 2\pi\nu_L$ and phase ϕ_L . In 1D and for a two-level system, the interaction can be described by the Hamiltonian [49]

$$H = H_0 + H_1, \quad (1.20)$$

$$H_0 = \hbar\omega \left(a^\dagger a + \frac{1}{2} \right) + \frac{1}{2} \hbar\omega_0 \sigma_z, \quad (1.21)$$

$$H_1 = \hbar\Omega (\sigma^+ + \sigma^-) \left(e^{i(kx - \omega_L t + \phi_L)} + e^{-i(kx - \omega_L t + \phi_L)} \right), \quad (1.22)$$

with x the ion position, $\omega_0 = 2\pi\nu_0$ the angular frequency corresponding to the energy difference of the two states, and σ the Pauli matrices defining the two-level system. The coupling strength Ω between ion and electromagnetic field is called Rabi frequency and is defined as

$$\Omega = \frac{|M|E_0}{\hbar}, \quad (1.23)$$

with the matrix element M depending on the type of atomic transition and the energy difference between the states, as will be explained later in this chapter. For now, the focus is kept on the motional energy of the ion.

The interaction Hamiltonian H_1 can be expressed in terms of the creation and annihilation operators, and with the Lamb-Dicke factor

$$\eta = kx_0 \cos \phi = k \sqrt{\frac{\hbar}{2m\omega}} \cos \phi \quad (1.24)$$

a relation between the wavelength of the laser and the ground state expansion of the wavepacket is provided. For convenience, here and in the following $i_0 = r_{0,i}$ with $i \in x, y, z$ is used, with $r_{0,i}$ as defined in equation (1.18). The angle between the laser and the direction of motion is described by ϕ . Furthermore, the rotating-wave-approximation is employed, which states that for

laser radiation close to the atomic resonance, $\omega_L \approx \omega_0$, fast oscillating terms of the form $e^{i(\omega_0 + \omega_L)t}$ can be neglected. Using the relation $H_I = e^{-iH_0 t/\hbar} H_1 e^{iH_0 t/\hbar}$ to go into the interaction picture, one finds

$$H_I = \hbar\Omega \left(\sigma^+ e^{i\eta(\hat{a} + \hat{a}^\dagger - \delta t + \phi)} + \sigma^- e^{-i\eta(\hat{a} + \hat{a}^\dagger - \delta t + \phi)} \right), \quad (1.25)$$

with $\delta = \omega_L - \omega_0$ and $\hat{a} = ae^{-i\omega_x t}$, where ω_x is the frequency of the ion in the harmonic potential. When solving the Schrödinger equation $i\hbar\partial_t\Psi = H\Psi$ for a state

$$\Psi(t) = \sum_n (c_n(t) |g, n\rangle + d_n(t) |e, n\rangle), \quad (1.26)$$

which is a linear combination of ground (g) and excited (e) states with time-dependent amplitudes c_n and d_n and vibrational quantum numbers n , one finds the coupling strengths

$$\Omega_{n+m,n} = \Omega \langle n+m | e^{i\eta(\hat{a} + \hat{a}^\dagger)} | n \rangle, \quad (1.27)$$

dependent on a change of the motional state. If the ion is well localized within the laser beam wavelength, i.e. $\sqrt{n}\eta \ll 1$, the ion is in the Lamb-Dicke regime [50] and the expression for the Rabi frequency can be well approximated using the Taylor expansion

$$e^{i\eta(\hat{a} + \hat{a}^\dagger)} = 1 + i\eta(\hat{a} + \hat{a}^\dagger) + \mathcal{O}(\eta^2). \quad (1.28)$$

Under these circumstances, changes of the vibrational quantum number n by more than one are largely suppressed and simple expressions for the Rabi frequencies can be given. On the carrier transition, for which n is not changing,

$$\Omega_{n,n} = \Omega(1 - \eta^2 n). \quad (1.29)$$

On the blue or red sideband transition with an increase or decrease of the vibrational quantum number by one during absorption,

$$\Omega_{n+1,n} = \Omega\eta\sqrt{n+1}, \quad (1.30)$$

$$\Omega_{n-1,n} = \Omega\eta\sqrt{n}. \quad (1.31)$$

For the simple example of starting in the ground state, $\Psi(0) = |g, n\rangle$ and applying radiation at the carrier frequency, the wave function in equation (1.26) evolves as [40]

$$\Psi(t) = \cos(\Omega_{n,n}t) |g, n\rangle - ie^{i\xi} \sin(\Omega_{n,n}t) |e, n\rangle, \quad (1.32)$$

with ξ a phase factor. The excited state population is given by

$$|\langle e, n | \Psi(t) | e, n \rangle|^2 = \sin^2(\Omega_{n,n}t). \quad (1.33)$$

For small values of $\Omega_{n,n}t$, this yields the transition rate

$$W = (\Omega_{n,n}t)^2 = \left(\frac{|M|E_0}{\hbar} (1 - \eta^2 n) t \right)^2. \quad (1.34)$$

Changing from the 1D case to the 3D trap, η needs to be replaced by an effective Lamb-Dicke parameter η_{eff} . Assuming thermal equilibrium and efficient cooling on all axes, $x_0 = y_0 = \sqrt{2}z_0$. Furthermore, assuming no fixed phase relation between the three individual directions of motion due to the isotropic spontaneous emission of photons, the average ion motion is described by a spheroid rotationally symmetric around z and with extension x_0 and z_0 along x and z , respectively. For an angle ϕ between laser and z axis, the effective Lamb-Dicke parameter can be described by

$$\eta_{\text{eff}} = k \sqrt{\frac{z_0^2}{1 - \frac{x_0^2 - z_0^2}{x_0^2} \sin^2 \phi}} = k \frac{z_0}{\sqrt{1 - \frac{1}{2} \sin^2 \phi}} = k \sqrt{\frac{\hbar}{2m\omega_z (1 - \frac{1}{2} \sin^2 \phi)}}. \quad (1.35)$$



For $\omega_z = 2\pi \times 1556$ kHz, a laser wavelength of $\lambda = 436$ nm, and $\phi = 45^\circ$, the effective Lamb-Dicke factor is $\eta_{\text{eff}} \approx 0.072$.

1.4.3 Cooling a trapped ion

For the ion to be in the Lamb-Dicke regime, it first needs to be cooled, for example by employing Doppler cooling [8] on an electric dipole-allowed transition that typically has an excited state lifetime of a few tens to hundreds of nanoseconds. This facilitates a cooling rate faster than the heating of the

ion and the detection of tens of thousands of photons per second from the ion fluorescence, providing a reliable signal for the presence of the ion. Since the radiative decay rate γ is much faster than the secular motion of the ion, $\omega_i \ll \gamma$, the motional sidebands are not resolved and the ion can be treated as a free particle. This is called the weak binding regime. From the optical Bloch equations, one finds the excited state probability in the limit of low saturation ($\Omega \ll \gamma$),

$$p_e = \frac{\Omega^2}{\gamma^2 + 4\delta^2}, \quad (1.36)$$

with $\delta = \omega_L - \omega_0$. If the ion is moving at a velocity v with respect to the laser beam, a first-order Doppler shift

$$\frac{\Delta\omega_D}{\omega_0} = \frac{v}{c} \rightarrow \Delta\omega_D = kv \quad (1.37)$$

leads to a detuning $\delta = \omega_L - \omega_0 - kv$. A radiation pressure force $F = \hbar k \gamma p_e$ is slowing the ion down, yielding a cooling rate $\dot{E}_c = \langle Fv \rangle$. It is counteracted by a heating rate $\dot{E}_h = (\hbar k)^2 \gamma p_e / m$ resulting from spontaneous emission and discrete absorption processes, which lead to the steady-state condition $\dot{E}_c + \dot{E}_h = 0$. For small velocities v , one finds

$$k_B T = -(1 + \alpha) \frac{\hbar(\gamma^2 + 4\delta^2)}{16\delta}, \quad (1.38)$$

with k_B the Boltzmann constant and α taking into account corrections. For spontaneous emission in 1D, $\alpha = 1$, and for the 3D case, $\alpha = 1/3$. For $\delta = -\gamma/2$, the lowest temperature, called the Doppler temperature, is given by

$$T_D = (1 + \alpha) \frac{\hbar\gamma}{4k_B}. \quad (1.39)$$

For $k_B T \gg \hbar\omega$, the mean quantum number is described by $\hbar\omega\bar{n} = k_B T$, resulting in $\bar{n}_D = (1 + \alpha)\gamma/(4\omega)$.



The typical cooling transition in Yb^+ has a linewidth of $\gamma \approx 2\pi \times 20$ MHz, corresponding to $T_D \approx 0.32$ mK and $\bar{n}_D \approx 8.5$, with $\alpha = 1/3$ and $\omega = 2\pi \times 780$ kHz. For this temperature, $k_B T \approx 30$ neV.

With the ion cooled to the Lamb-Dicke regime, more evolved cooling schemes can be deployed, such as the resolved sideband cooling technique [8]. Here, absorption of a photon on the red sideband ω_i removes one quantum of motion. The following spontaneous emission does not change the vibrational quantum number most of the time, since Rabi frequencies for the sideband transitions are largely suppressed, as demonstrated by equations (1.29) to (1.31). Consequently, the ion is cooled, but emission on the red sideband every now and then, which has a higher probability than emission on the blue sideband, heats the ion and leads to an equilibrium quantum number \bar{n}_{SB} :

$$\begin{aligned}\bar{n}_{\text{SB}} &= \frac{\gamma^2}{4\omega_i^2} \left(\frac{1}{4} + \frac{\eta_e^2}{\eta^2} \right), \\ \eta_e^2 &= \alpha\eta^2, \quad \alpha < 1,\end{aligned}\tag{1.40}$$

with η_e^2 the Lamb-Dicke parameter for spontaneous emission taking into account that the scattering is only partially along the axis of motion.

To address an individual sideband, the laser linewidth needs to be sufficiently narrow, i.e. $\omega_i \gg \gamma$, which is called the strong binding regime. Therefore, sideband cooling is typically performed on a clock transition. The cooling cycle time can be sped up by employing a repump laser that brings the ion from the excited clock state back to the ground state via an auxiliary level of shorter lifetime and with linewidth γ_{aux} that yields an effective linewidth of the sideband cooling transition

$$\gamma' = \frac{\Omega_{\text{aux}}^2 \gamma_{\text{aux}}}{4\delta_{\text{aux}}^2 + (\gamma_{\text{aux}} + \gamma)^2}.\tag{1.41}$$

The linewidth γ' can be tuned with the detuning δ_{aux} and the laser power of the repump laser. It is assumed that the line broadening remains small compared to the sideband splitting.



Sideband cooling is performed on a transition with a linewidth of $\gamma \approx 2\pi \times 3$ Hz that is broadened using an auxiliary level to an effective linewidth of $\gamma' = 10 \dots 100$ kHz, which enables $\bar{n} \ll 1$ with $\omega_x = 2\pi \times 778$ kHz.

In order to measure the mean population of the harmonic oscillator levels of the ion, two methods are employed in the course of this thesis. The first one is called carrier-sideband method and relies on a measurement of the relative strength between the excitation probability of the red sideband and the carrier transition, yielding

$$\frac{p(\delta = -\omega)}{p(\delta = 0)} = \sum_n p_n \frac{(\Omega\eta\sqrt{n})^2}{\Omega^2} = \eta^2 \bar{n} \quad (1.42)$$

for a thermal state distribution with p_n the probability for occupation of n . Alternatively, the damping of a Rabi-flopping experiment on the carrier transition can be used to infer the mean motional state. With a Rabi-flopping experiment, the cycling of the population between ground and excited clock state is resolved in time. The excitation probability as a function of time can be written as

$$p_{\bar{n}}(t) = \sum_n p_n \sin^2(\Omega_{n,n}t/2) = \frac{1}{2} \left(1 - \sum_n p_n \cos(\Omega_{n,n}t) \right) = \frac{1}{2}(1 - \text{Re}(X(t))),$$

where $X(t) = \sum_n p_n e^{i\Omega_{n,n}t}$. For a thermal state distribution, the probabilities take the form

$$p_n = \frac{1}{\bar{n} + 1} \left(\frac{\bar{n}}{\bar{n} + 1} \right)^n = \frac{1}{\bar{n} + 1} x^n, \quad x = \frac{\bar{n}}{\bar{n} + 1}.$$

Using $\Omega_{n,n} = \Omega(1 - \eta^2 n)$, $X(t)$ can be written as

$$X(t) = \frac{e^{i\Omega t}}{\bar{n} + 1} \sum_n x^n e^{-i\Omega t \eta^2 n} = \frac{e^{i\Omega t}}{\bar{n} + 1} \frac{1}{1 - x e^{-i\Omega t \eta^2}} \approx \frac{e^{i\Omega t}}{1 + i\Omega t \eta^2 \bar{n}}$$

with $e^{-i\Omega t \eta^2} \approx 1 - i\Omega t \eta^2$. Consequently, cycling of the population between ground and excited clock state of the form

$$p_{\bar{n}}(t) = \frac{1}{2} \left(1 - \frac{\cos(\Omega t) + \Omega t \eta^2 \bar{n} \sin(\Omega t)}{1 + (\Omega t \eta^2 \bar{n})^2} \right) \quad (1.43)$$

can be observed.

With the carrier-sideband method, a specific sideband and therefore a distinct motional mode of the ion is probed. It should be noted that for the

ideal trap, the radial modes are degenerate. In practice however, small deviations from cylindrical symmetry lead to a nonzero splitting of the radial modes. With the Rabi-flopping method, all modes are probed that have a spatial overlap with the laser direction as described by equation (1.35).

1.4.4 Spectroscopy on clock transitions

Different atomic transitions are employed in an optical clock with trapped ions. First of all, the ion needs to be Doppler cooled on an electric dipole-allowed transition in order to reach the Lamb-Dicke regime. Then, the carrier transition of an electric dipole-forbidden transition provides the reference of the atomic clock. Such transitions have an excited state lifetime of milliseconds to years that correspond to small linewidths in the range of several hertz to nanohertz. To detect the successful excitation of the clock transition, the fluorescence signal of the ion resulting from excitation of the cooling transition is measured. Once the ion is excited to the long living clock state, the fluorescence signal vanishes. This method [51] is known as electron shelving.

Mathematically, the different types of transitions are expressed by the transition moment M introduced for the Rabi frequency in equation (1.23). It arises from a coupling of the atom's electrons with the electromagnetic field. The Born-Oppenheimer approximation is employed, which recognizes that electrons move much faster than the nucleus, i.e. the motions are on different timescales and can be discussed separately. The exponential describing the electron-light interaction can be expanded in a Taylor series [52]

$$e^{i\mathbf{k}\mathbf{r}_i} = 1 + i\mathbf{k}\mathbf{r}_i - \frac{1}{2}(\mathbf{k}\mathbf{r}_i)^2 + \dots \quad (1.44)$$

if the wavelength is large compared to the atomic structure, with \mathbf{r}_i the distance of the i -th electron to the nucleus. Taking into account only the zero-order term is called the dipole approximation and the electric dipole (E1) matrix element takes the form

$$D = \epsilon \langle e|q \sum_i \mathbf{r}_i|g\rangle. \quad (1.45)$$

Expanding to first order and implicitly summing over the Greek indices labeling

the Cartesian coordinates, the electric quadrupole (E2) matrix element

$$Q_{\alpha\beta} = \frac{1}{2} k_{\alpha} \epsilon_{\beta} \langle e | q \sum_i r_{i,\alpha} r_{i,\beta} | g \rangle \quad (1.46)$$

is found, which is relevant in electric quadrupole transitions. The second-order expansion yields the electric octupole (E3) matrix element

$$O_{\alpha\beta\gamma} = \frac{1}{6} k_{\alpha} k_{\beta} \epsilon_{\gamma} \langle e | q \sum_i r_{i,\alpha} r_{i,\beta} r_{i,\gamma} | g \rangle \quad (1.47)$$

used for the description of electric octupole transitions. Additionally to the electric multipole transitions, there are magnetic multipole transitions, which will not be further discussed within the thesis.

Higher-order multipole transitions are called forbidden as they are not allowed by the dipole selection rules [53]. In turn, a dipole-allowed transition may also be allowed in terms of higher-order multipole transitions, but these are suppressed due to their significantly weaker rates as demonstrated by the following examples. Approximating the electron-nucleus distance by the Bohr radius a_0 and using equation (1.34) in combination with the definitions for the matrix elements above, rough estimates for the relative rates of the higher-order multipole transitions compared to the dipole transition can be found:

$$\frac{W_{E2}}{W_{E1}} = \frac{|Q|^2}{|D|^2} \approx \frac{k^2 a_0^4}{4a_0^2} = \frac{k^2 a_0^2}{4}, \quad (1.48)$$

$$\frac{W_{E3}}{W_{E1}} = \frac{|O|^2}{|D|^2} \approx \frac{k^4 a_0^6}{36a_0^2} = \frac{k^4 a_0^4}{36}. \quad (1.49)$$

Since $k^2 a_0^2 \ll 1$, the higher-order multipole transitions have much lower transition rates and need to be driven by high laser intensity or long laser-ion interaction time.



With $\lambda_{E2} \approx 436$ nm and $\lambda_{E3} \approx 467$ nm for the E2 and E3 transition, respectively, one finds $W_{E2}/W_{E1} \approx 1 \times 10^{-7}$ and $W_{E3}/W_{E1} \approx 6 \times 10^{-15}$. The transition rate on the E2 transition is about seven orders of magnitude stronger compared to the E3 transition. A rough comparison of the required intensities to drive a 30 ms π -pulse, $I_{E2} \approx 0.5$ W/m² and $I_{E3} \approx 3$ MW/m², yields a very similar result.

1.4.5 A stable laser source

Clock transitions permit long coherence times, in principle limited by the lifetime of the excited state. For optical transitions, coherence times of up to 10 s between ions have been demonstrated [54], even in two separated trap setups [55]. In order to obtain similar coherence times between local oscillator and the atom, the laser has to be stabilized accordingly. Typically, the Pound-Drever-Hall locking technique [56, 57] is employed to stabilize the laser frequency to a longitudinal mode of an optical cavity, a Fabry-Pérot etalon consisting of two highly-reflective mirrors optically contact bonded to a spacer.

Several technical challenges need to be overcome for the cavity to become ultra-stable [9], including active and passive temperature stabilization, vibrational decoupling and careful alignment of the laser mode. Typical ULE (ultra-low expansion) glass cavities operated at room temperature have a length of about 100 mm and are limited by thermomechanical noise to a fractional frequency instability of a few 10^{-16} for about 100 ms to a few seconds. On larger timescales, length changes of the cavity lead to long-term frequency fluctuations on the order of tens to hundreds of millihertz per second. In particular, aging of the material and settling of optical contacts result in frequency drifts, and temperature changes cause slow frequency variations. State-of-the-art cryogenically cooled single-crystal silicon cavities [58] show fractional frequency instabilities of 5×10^{-17} for tens of seconds and frequency drift rates of less than a millihertz per second. The linewidth of a laser stabilized to such a cavity is on the order of 10 mHz.

For the experiments conducted in this thesis, the E2 and E3 transition clock lasers are stabilized with high bandwidth of about 500 kHz to ULE cavities next to the laser setup, with relative frequency instabilities of better than 2×10^{-15} [59] and about 5×10^{-16} [42], respectively. Using a frequency comb, the stability of the silicon cavity Si-2 [58], provided by the department “unit of length” at PTB, is transferred to the clock lasers, enhancing their short-term stability. The clock instability is investigated in more detail in section 2.4 and the transfer scheme is discussed in section 3.1.

1.4.6 Spectroscopy sequence

With the ion well under control and a stable laser at hand, precision spectroscopy of a clock transition can be performed. One interrogation cycle consists of a train of laser pulses with the state of the ion detected by observing fluorescence (no excitation of the reference transition) or no fluorescence (successful excitation of the clock transition) in the cooling cycle according to the electron shelving technique. As shown in figure 1.3, a single cycle starts with a cooling period on a fast-cycling transition, bringing the ion close to the motional ground state. Next, it is prepared in the electronic ground state of the clock transition. A settling time allows for the decay of magnetic fields, that are switched after the cooling period, and the closing of mechanical shutters to block cooling laser light. Single or multiple laser pulses on the clock transition are employed to compare the atomic reference to the frequency of the local oscillator. In the detection period, the cooling laser light is reintroduced to probe the successful excitation of the clock transition with the electron shelving technique. Afterwards, additional laser light for fast depopulation of the clock state starts the cooling period again.

While a single interrogation cycle only gives the binary information whether the clock transition has been driven successfully, the combination of multiple interrogation cycles generates spectroscopic information. At least one experimental parameter is varied in between the cycles, such as the clock pulse sequence, the local oscillator frequency detuning Δf from the transition frequency ν_0 , the time of the atom-oscillator interaction τ , or the settling time t_s . Furthermore, interrogation cycles with the same set of parameters are repeated in order to reduce the statistical uncertainty due to quantum projection noise [10]. In the following, a few examples for experiments conducted in the course of this thesis are given.

Clock pulse sequences of different types can be employed, with the most prominent examples of a single Rabi pulse or two pulses of a Ramsey sequence separated by a dark time T_{dark} [60, 61] as shown in the inset of figure 1.3. For a π -pulse, the Rabi pulse time is chosen to maximize the population transfer from ground to excited state on resonance. For a Ramsey sequence, a $\pi/2$ -pulse first initiates the maximum coherence between both atomic states of the clock transition. After T_{dark} , a second

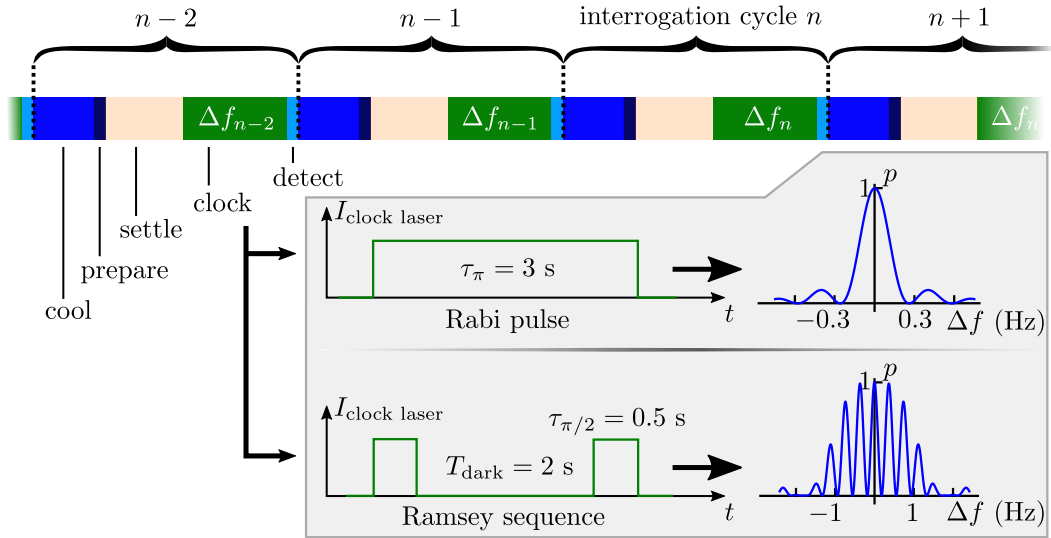


Figure 1.3: **Example of the spectroscopic sequence.** Each interrogation cycle consists of an ion cooling and preparation phase, a settling time, the atom-laser interaction (clock) sequence and a detection period. During the cooling times the clock laser detuning Δf is changed in equal frequency steps, yielding spectroscopic signals as shown in the inset. There, the excitation probability of the clock transition p in dependence of the detuning for both Rabi and Ramsey experiments with π - and $\pi/2$ -pulse times τ_π and $\tau_{\pi/2}$ are depicted, obtained from the solution of the optical Bloch equations with coupling strengths $\Omega_{\text{Rabi}} = 2\pi \times \frac{1}{6}$ Hz and $\Omega_{\text{Ramsey}} = 2\pi \times \frac{1}{2}$ Hz. The corresponding Rabi and Ramsey fringes have a full width at half maximum of 0.27 Hz and 0.19 Hz.

$\pi/2$ -pulse transfers the phase difference between laser and atom into a population difference of ground and excited state. More evolved schemes such as hyper-Ramsey spectroscopy [62] are used to provide immunity to external perturbations such as ac Stark shifts due to the laser light probing the ion, also known as light shifts. Interleaving Rabi pulses and the (hyper-)Ramsey scheme during clock operation, these light shifts can be further suppressed: The frequency shift is measured with the Rabi excitation and applied as a frequency correction during the Ramsey pulses [63]. In the following, this will be referred to as Rabi-controlled (hyper-)Ramsey.

The oscillator frequency ν_L is changed in a detuning scan in equally spaced steps within a frequency interval, probing the transition multiple times on each detuning Δf from the transition frequency ν_0 . The principle scheme of a detuning scan experiment is shown in figure 1.3, with

the outcome both depicted for a single π -pulse and a Ramsey sequence, obtained from numerically solving the optical Bloch equations [64].

The atom-oscillator interaction time τ can be varied at a fixed detuning Δf . If $\Delta f = 0$ and a Rabi pulse of variable length is employed, this yields a Rabi-flopping experiment as derived in equation (1.43). Alternatively, for a Ramsey experiment with variable T_{dark} and $\Delta f \neq 0$, a signal similar to Rabi flopping is observed, as will be discussed in section 2.4.

The settling time t_s is changed in between different Rabi-flopping experiments in order to measure the motional heating of the ion, as discussed in section 2.3.4.

Using the information from the atomic reference to control the local oscillator in a feedback loop, clock operation can be realized. This is explained here for the simplest clock pulse sequence, a single π -pulse. The atomic transition with frequency ν_0 is interrogated by the laser at the frequencies $\nu_L \pm \Delta f_c$. The constant detuning Δf_c is chosen such that for $\nu_L = \nu_0$, the excitation probability p shows the highest sensitivity to changes of ν_L . This corresponds to the excitation probability $p_{\pm} = 0.5$ for both positive and negative detunings Δf_c , which are the points at the full width at half maximum of the Rabi pulse signal shown in figure 1.3. The difference $\Delta p = p_+ - p_-$ serves as the discriminator signal (or error signal) yielding

$$\Delta p < 0 \longrightarrow \nu_L > \nu_0,$$

$$\Delta p > 0 \longrightarrow \nu_L < \nu_0,$$

$$\Delta p = 0 \longrightarrow \nu_L = \nu_0.$$

The error signal is fed back to a digital servo controlling the laser and correcting ν_L , thereby locking it to the atomic reference. More sophisticated sequences are based on the same principle but include multiple servos and additional detunings. With a scheme for coherent suppression of tensorial shifts [65] and with the autobalanced Ramsey scheme [66], two such examples are presented in chapter 4.

1.5 The ion of choice

$^{171}\text{Yb}^+$ was already experimentally investigated in a Paul trap in the early 1980s [67] and its potential as a frequency standard recognized, first for microwave but then for optical transitions as well [68, 69]. The large ion mass yields low ion velocities, corresponding to low motional shifts. With a nuclear spin of $1/2$, the ion provides a simple hyperfine structure with clock transitions between $m_F = 0$ levels that are insensitive to the linear Zeeman effect. All relevant transitions shown in figure 1.4 (A) can be driven by light generated with diode lasers that are easy to handle and permit robust clock operation. A fast-cycling cooling transition is provided at 370 nm, with an excited state lifetime $\tau = 8.12(2)$ ns [70] that yields a natural linewidth $\gamma = 2\pi \times 19.60(5)$ MHz. The ion is typically stored in the trap for several months, the only relevant chemical reaction occurring at times is the formation of YbH^+ molecules with hydrogen atoms from the background gas, which can be photodissociated again by photons from the cooling laser [71].

However, the most important advantage of Yb^+ is given by the available clock transitions of different multipolarity: The atom features both the $^2\text{S}_{1/2} \rightarrow ^2\text{D}_{3/2}$ electric quadrupole (E2) [72, 73] and the $^2\text{S}_{1/2} \rightarrow ^2\text{F}_{7/2}$ electric octupole (E3) [74, 75] transition. With an excited state lifetime of about 53 ms [76] and a natural linewidth of $2\pi \times 3.0$ Hz, a π -pulse time of 30 ms can be achieved with an intensity of about 0.5 W/m^2 for the E2 transition. In contrast, the $^2\text{F}_{7/2}$ state natural lifetime² is 1.58(7) years (as measured in section 4.4) and the highly forbidden E3 transition with a natural linewidth in the nanohertz range is driven by an intensity of about 3 MW/m^2 for a transition rate comparable to that of the E2 transition. The resulting light shift of about 100 Hz can be corrected during clock operation, for example by employing the Rabi-controlled hyper-Ramsey scheme explained in the previous section.

As indicated by the different lifetimes, electronic configurations of the excited clock states shown in figure 1.4 (B) differ significantly. There are also large differences in the sensitivities to external perturbations, with the E2 transition frequency in general much more sensitive to external fields: The electric

²In experimental realizations, the $^2\text{F}_{7/2}$ state is quenched by excitation of repumping transitions through thermal radiation and by background gas collisions, resulting in an effective lifetime on the order of one hour as discussed in section 2.3.9.

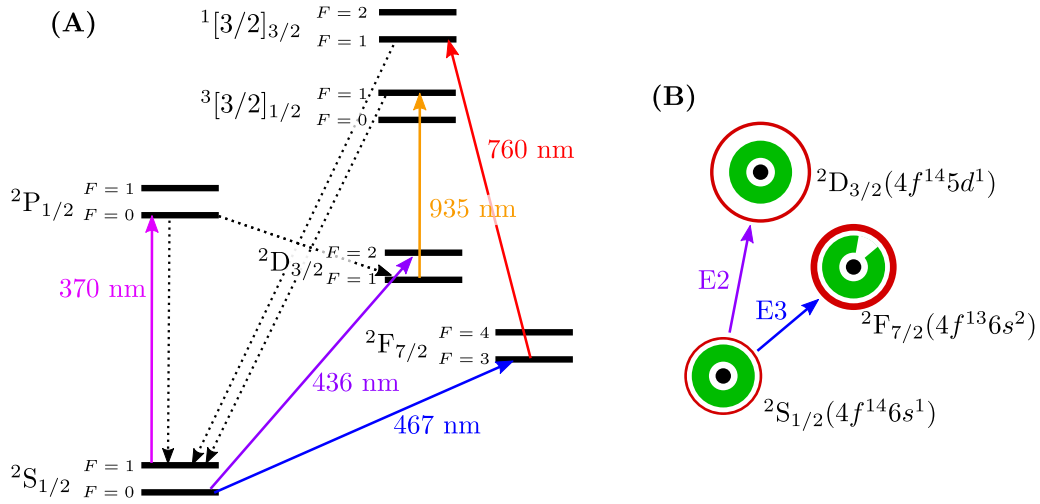


Figure 1.4: **Level structure of $^{171}\text{Yb}^+$.** (A) Sketched are the cooling transition at 370 nm, the E2 clock transition at 436 nm and the E3 transition at 467 nm. Repump lasers at 935 nm and 760 nm are used to depopulate the excited clock state and to facilitate a closed cooling cycle. (B) The excited clock states exhibit very different electronic structures: While the $2D_{3/2}$ state features a single valence electron in an outer shell, the $2F_{7/2}$ state has a single hole in a shell close to the nucleus, surrounded by a filled shell. The differences in the electronic structures are related to the very different characteristics of the two clock transitions, including the excited state lifetimes and the sensitivities to external perturbations.

quadrupole shift, discussed in section 2.3.8, is by a factor of 68, the second-order Zeeman shift, discussed in section 2.3.6, by a factor of 25 larger on the E2 transition. The two very different clock transitions provide versatility that can be exploited in high precision spectroscopy. Environmental conditions at the ion position are assessed with the more sensitive E2 transition, i.e. it is used as a sensor for perturbing fields. With knowledge of the shift proportionality factor between the clock transitions, the strength of the perturbation can be inferred on the E3 transition for high-accuracy clock operation.

There is one particular exception in terms of the sensitivity: The $2F_{7/2}$ state possesses a single hole in the $4f$ shell and its proximity to the heavy nucleus makes large relativistic contributions for the E3 transition energy plausible. Indeed, this is presently the most sensitive transition to variations of the fine structure constant α in an operational optical clock [77]. Consequently, the E3 transition is a suitable candidate to search for new physics as will be discussed in chapter 3.

1.6 $^{171}\text{Yb}^+$ ion clocks at PTB: A status report

The status quo ante.

Since 2016, two $^{171}\text{Yb}^+$ single-ion clocks are evaluated and operable at PTB. The first one, referred to as Yb1, was originally set up in the mid-1990s and comprises a traditional Paul trap with a ring and two endcap electrodes. The suppression of light shift on the E3 transition has been studied in detail in this trap [63], as well as other contributions to the systematic uncertainty [75], making it the most accurate ion clock in 2016 [33]. For the second system, Yb2, extensive studies of different trap geometries were performed [47] that converged to an endcap-trap design set up in 2008. Both experiments are located in a laboratory at PTB called the clock hall, together with a frequency comb, two caesium beam and two caesium fountain clocks. A detailed schematic and discussion of the infrastructure is given in section 3.1.

Progress reported within this thesis.

For the E3 transition, the two ion trap setups Yb1 and Yb2 have been evaluated with a fractional systematic frequency uncertainty of about 3×10^{-18} . In a long-term comparison over 6 months in 2017, an agreement within the combined uncertainty has been found [36]. Evaluating the acquired data for a test of fundamental physics, the limits on a violation of local Lorentz invariance (LLI) have been tightened by about two orders of magnitude. Furthermore, measurements of the ratio of the E2 and E3 transition have been performed with the two trap systems over a period of more than four years, starting in 2016. The mean value improves upon knowledge of the ratio by an order of magnitude. Additionally, the absolute frequency of the E3 transition has been obtained in comparisons with the caesium fountain clocks, providing the most accurate measurement of an optical transition frequency to date. Both the frequency ratio and the absolute frequency measurements are used for stringent tests of local position invariance (LPI) [39]. Further comparisons have been performed between Yb1 on the E3 transition and the ^{87}Sr lattice clock on the

$(5s^2)^1S_0 \rightarrow (5s5p)^3P_0$ transition at PTB. These are the first measurements reported for the direct comparison of this pair of clock species, yielding an optical frequency ratio with a fractional uncertainty of 2.5×10^{-17} [38]. All these comparisons are described in chapter 3.

The experimental investigation of Yb1 and Yb2 have revealed the potential for further improvements. To go beyond the 10^{-18} relative uncertainty limit, the leading contributions of the systematic uncertainty, blackbody radiation and second-order Doppler shift, need to be reduced. To achieve this goal, a third trap system called Yb3 has been set up and partially evaluated. The new designs of vacuum chamber and ion trap show promising results regarding trap temperature, ion heating and optical access. An update in the control soft- and hardware enables better automation of experimental routines and a closer surveillance of critical parameters, improving upon the robustness of the clocks. In chapter 2, the Yb3 system is introduced and the different contributions to the systematic uncertainty are discussed. A detailed investigation of the frequency stability is performed. First results on comparisons of the clock transition frequencies realized with Yb3 and with the other systems are presented in chapter 3.

Improvements of atomic clocks is not only achieved by more evolved experimental setups, but also by developing advanced interrogation schemes that provide increased robustness to external perturbations or improve the clocks' frequency stability. Such schemes are discussed in chapter 4. Due to the high intensity of the probe laser, interrogation schemes for the E3 transition need to control or suppress a significant light shift. The dependence between Rabi frequency and light shift is investigated, from which the lifetime of the $^2F_{7/2}$ state is inferred. The light shift can be reduced by employing twisted light instead of a plane wave to drive the transition. Twisted light consists of Laguerre-Gaussian modes featuring orbital angular momentum. The first excitation of an E3 transition with twisted light is reported in chapter 4, and the changes in the excitation properties of the transition are compared to theoretical predictions. A summary of the results in combination with an outlook on experiments planned in the near future, including investigations of co-trapping $^{171}\text{Yb}^+$ and $^{88}\text{Sr}^+$ ions in a linear Paul trap, concludes this thesis.

Chapter 2

Yb³⁺ - A new clock with reduced uncertainty

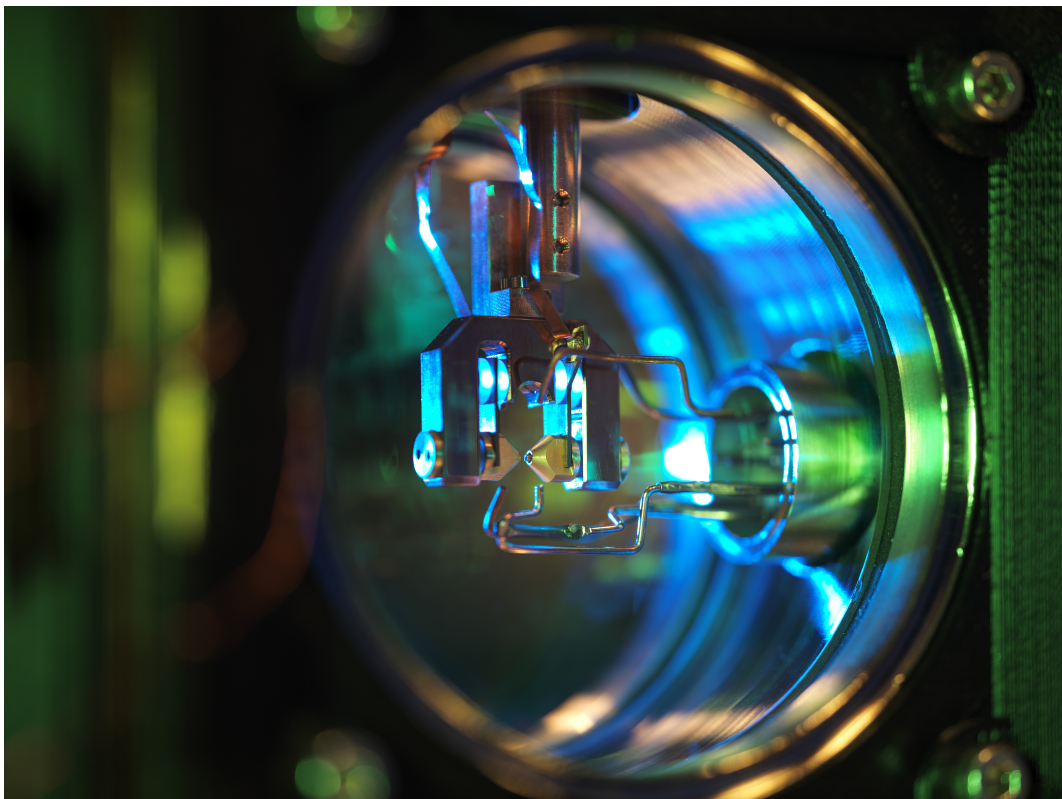


Figure 2.1: Yb³⁺ ion trap.

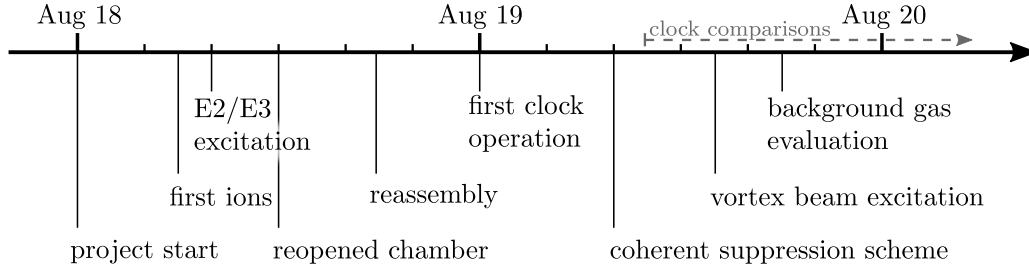


Figure 2.2: **Milestones in the Yb3 setup.** Assembly of the system started in August 2018. Main achievements so far include the demonstration of a coherent suppression scheme and the excitation of vortex beams, discussed in section 4.1 and section 4.5. Since the beginning of 2020, the clock is compared regularly to the other Yb^+ systems at PTB.

Yb3 is the third-generation trap system for an optical atomic clock based on a single $^{171}\text{Yb}^+$ ion operated at PTB. With this trap generation, a fractional systematic uncertainty below 10^{-18} is pursued. Yb3 incorporates improvements with respect to the previous systems Yb1 and Yb2 and is integrated in the same laboratory infrastructure, e.g. using the same clock lasers. As can be seen in figure 2.2, the Yb3 project started in August 2018, one year later clock operation was first established. By August 2020, detailed evaluations of various shift effects as well as comparisons to other clock systems have been performed. In parallel, an almost identical trap system has been set up in the clock hall within a project called opticlock and in collaboration with academic and industry partners. The large similarities between the traps of opticlock and Yb3 permit direct comparisons of various properties. This chapter will first provide an overview over the Yb3 setup and a short introduction to the opticlock system, followed by a detailed investigation of the uncertainty contributions for Yb3 and an analysis of the clock stability.

2.1 Trap setup and clock control

With respect to the Yb2 endcap trap design [47], the trap of Yb3 has been further optimized [44], with plane endcap electrode faces and flattened tops on the outer electrodes, facilitating more precise fabrication. The trap electrodes are made from molybdenum for high machining accuracy that is on the order of 0.01 mm. To further enhance the accuracy, the electrode positions are determined by well-defined and precisely machined contact points with the trap holder that is made from a CuCrZr alloy.

The endcap electrode surface has been polished and sputtered with a gold layer of a few micrometer thickness. This procedure is performed to investigate anomalous heating [78] related to electric field noise, attributed to impurities adsorbed on the electrodes [44]: For gold-coated traps, low motional heating of 1 phonon/s and less has been reported [79, 80]. In contrast, ions in the Yb1 and Yb2 traps with bare molybdenum electrodes experience heating rates on the order of 100 phonons/s. To analyze the effect of the gold layer, heating rates of the Yb3 and the optically clocked trap are compared, since the traps are identical apart from the gold-coating for Yb3. Indeed a reduction of the heating rate for Yb3 by a factor 25 is found, as will be discussed in section 2.3.4.

Instead of MACOR¹ insulators as mounted in Yb1 and Yb2, low-loss insulators made from fused silica are installed between the rf voltage and ground. This facilitates a lower and more homogeneous trap temperature, reducing the uncertainty in the blackbody radiation shift as explained in section 2.3.2. A vacuum feedthrough connects the trap to a helical resonator for a narrow-band rf drive.

The trap is installed in a stainless steel vacuum chamber with a volume of about 1 l. With an SAES Getters NEX Torr Z100 ion getter pump, an ultra high vacuum at the 10^{-9} Pa level is reached. Details on the vacuum quality assessment will be given in section 2.3.9. The vacuum chamber has two circular fused silica viewports with a diameter of 70 mm in about 25 mm distance from the trap center for large optical access. This enables laser paths at nearly arbitrary angles with respect to the trap axes, important for example for 3D monitoring of the photon correlation signal explained in section 2.3.4.

¹MACOR is a machinable glass ceramic developed by Corning Incorporated: <https://www.corning.com/specialtymaterials/macor> (accessed September 7, 2021)

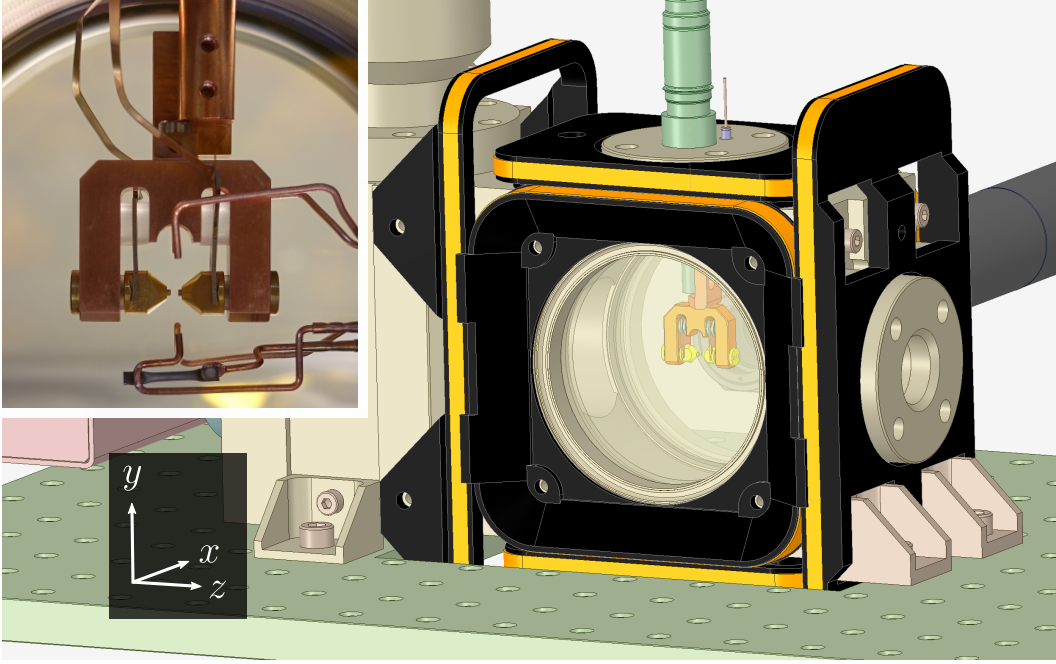


Figure 2.3: **CAD model** of the vacuum chamber and trap, with three pairs of 3D printed coils mounts in black attached to provide a precise magnetic field at the ion position that is generated by the coil currents. The coordinate system is oriented such that the z axis corresponds to the axial trap direction. The inset shows a picture of the trap.

Pairs of copper coils wound on 3D printed coil mounts are attached to the outside of the chamber and generate magnetic fields along the three principal axes as defined in figure 2.3. A current supply provides a maximum current of about 10 mA, leading to a magnetic field of about 20 μT at the ion position. This corresponds to a first-order Zeeman shift $\Delta\nu_{Z1} \approx 300$ kHz for the ${}^2\text{S}_{1/2} |F = 0, m_F = 0\rangle \rightarrow {}^2\text{D}_{3/2} |F = 2, m_F = 2\rangle$ transition. Along the x direction, an additional pair of coils provides a large magnetic field yielding $\Delta\nu_{Z1} \approx 6$ MHz for the cooling period. The magnetic fields produced will be discussed in greater detail in section 2.3.6.

Mounted on an aluminum breadboard of 450 mm by 300 mm size standing on 75 mm long posts, the vacuum chamber is placed inside a double-layer μ -metal shielding box for suppression of external magnetic fields by three orders of magnitude. Holes in the shielding provide optical access to the trap. Fibers and optics are placed inside as well as outside of the shielding to guide the laser beams to the ion, as shown in figures 2.4 and 2.5. At the ion position,

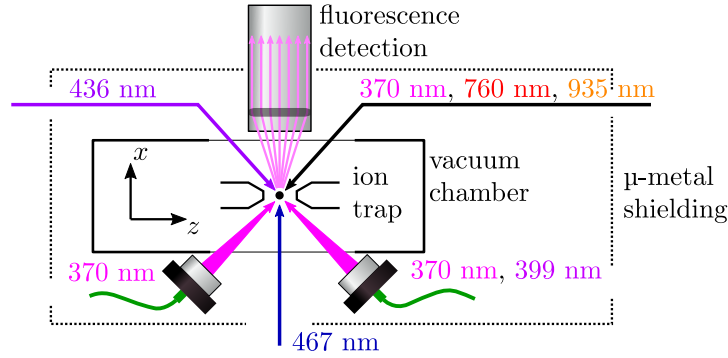


Figure 2.4: **Laser beam layout of Yb3.** Light for cooling (370 nm) and photoionization (399 nm) is guided by optical fibers (green) into the μ -metal shielding and focused to the ion with partial projection along the y -direction. All other laser beams travel through free space into the μ -metal shielding, within the xz -plane. Beams for cooling (370 nm) and repumping (760 nm, 935 nm) are overlapped and focused by a triplet lens. Clock laser light (436 nm, 467 nm) is projected onto the ion from different directions. Ion fluorescence is collected by a lens and imaged either on a camera or a photomultiplier tube.

the beams have approximately the following propagation vectors \mathbf{k} , with the coordinate system defined in figure 2.3:

370 nm cooling is employed from three directions with \mathbf{k} approximately along $[1, -1, 1]$, $[1, -1, -1]$, and $[-1, 0, -1]$, providing a projection of cooling laser light to all three axes of the ion motion,

399 nm photoionization is fiber-coupled to the $[1, -1, -1]$ cooling laser beam,

760 nm and 935 nm repumper are overlapped with the $[-1, 0, -1]$ cooling laser beam and focused with a triplet lens,

435 nm E2 clock is projected along the $[-1, 0, 1]$ direction onto the ion,

467 nm E3 clock is projected along the $[1, 0, 0]$ direction onto the ion.

Additionally, the imaging system is installed to guide the ion fluorescence along the $[1, 0, 0]$ direction to either a CCD camera or a photomultiplier tube. The full setup is placed on a 1200 mm by 1000 mm honeycomb structure breadboard.

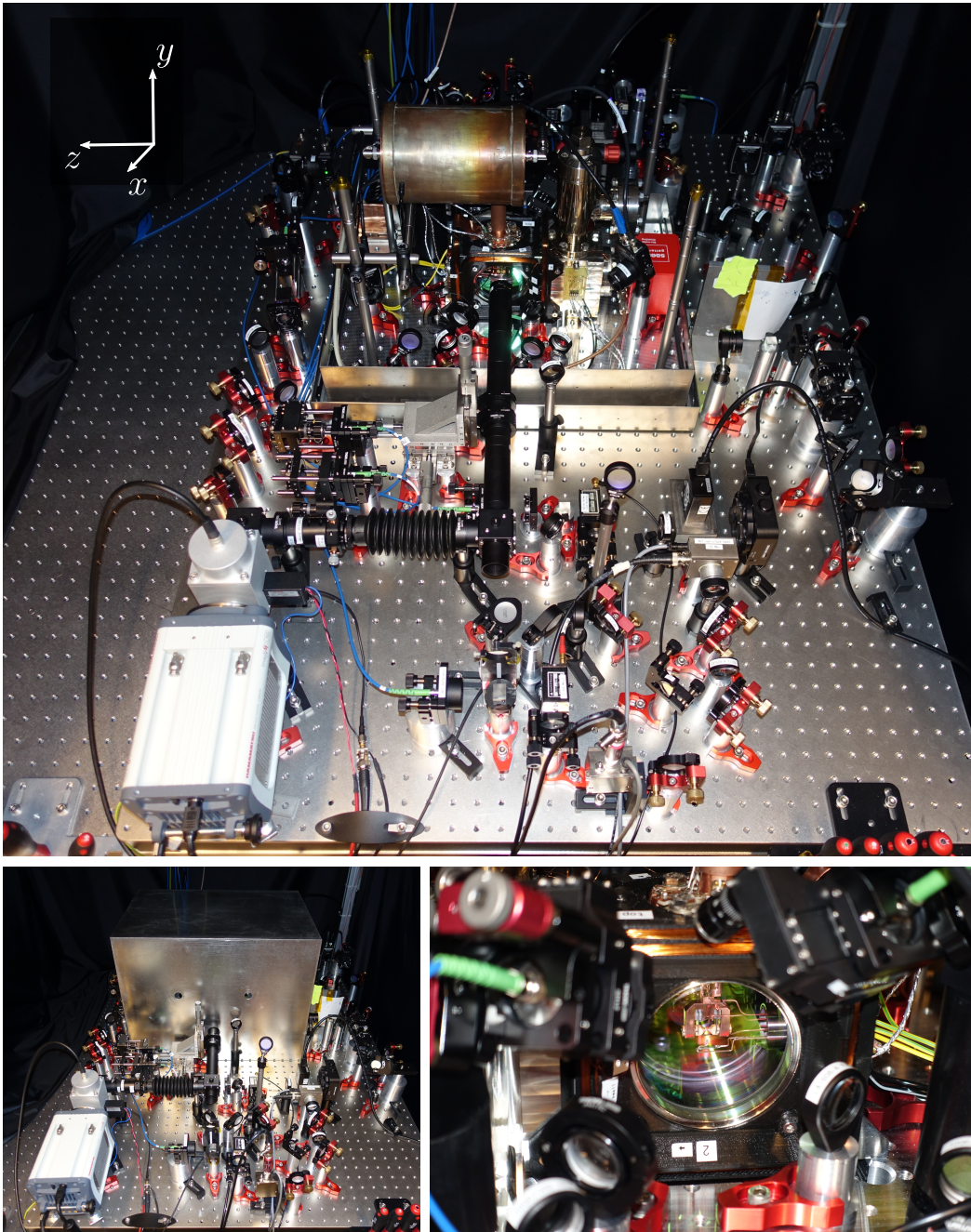


Figure 2.5: **Yb3 setup.** The top picture shows the fully operable experiment with the trap at its center. Optics are placed inside and around the two-layer μ -metal shielding box that surrounds the vacuum chamber and from which only the bottom part is installed. The coordinate system in the top left corner is oriented as defined in figure 2.3. The bottom left picture shows the same perspective with the entire μ -metal shielding in place. The bottom right picture is taken from the opposite side of the vacuum chamber. There, two cooling laser ports directed onto the trap are visible in the front.

All laser light is guided via fibers to the trap setup and each laser head is installed on an individual breadboard. This modular concept enables maintenance and modification of individual components of the experiment without major interferences of the remaining parts, minimizing perturbations and enhancing flexibility. Laser heads, optical transfer cavities and other infrastructure are stored separately, saving space in the laboratory: A $1\text{ m} \times 1\text{ m} \times 2\text{ m}$ cabinet shown in figure 2.6 provides five stacked, individually extractable platforms and can house about ten individual optical breadboards. Featuring doors and a laminar flow hood, the cabinet is kept free of dust. All necessary electronics are stored in a separate rack. The modular concept facilitates a well-arranged laboratory and clearly separated experiments.



Figure 2.6: **Laser cabinet** with individually extractable platforms for optical breadboards.

An organized structure is not only aimed for in the setup, but also in the control of the experiment. Yb3 is using the Sinara hardware controlled by the Artiq software². Code for the experiments is written using the programming language Python. As both optclock and Yb1 feature the same control platform, routines can be exchanged and adapted between the systems. For the organization of the experimental code and their different versions, a GitLab³ server is used. Single experimental results are stored in hdf5-files. Supervision of environmental conditions such as lab temperature or laser power, as well as monitoring of clock operation is handled by an InfluxDB⁴ database connected

²M-Labs 2021, <https://m-labs.hk/experiment-control/artiq> (accessed September 7, 2021)

³GitLab 2021, <https://gitlab.com> (accessed September 7, 2021)

⁴InfluxData 2021, <https://www.influxdata.com> (accessed September 7, 2021)

to a Grafana⁵ server for visualization. Alarm routines with email notifications have been set up and a VPN connection to the PTB network makes remote access possible. The permanent surveillance of the clocks vastly improves their robustness, enables fast troubleshooting and facilitates large uptime windows during clock operation.

2.2 opticlock - the industrial twin



Figure 2.7: **Setup of opticlock.** Top left is a picture of the trap, identical to the Yb3 design but without the gold-coating on the endcap electrodes. Bottom left shows the vacuum chamber with installed trap. The right hand side picture is a view of the full setup. The left rack houses the electronic components, the right rack contains lasers, cavity and the physics package.

Parallel to the early stages of setting up Yb3, a pilot project of quantum technology in Germany called opticlock⁶ started that included the assembly of another clock in the clock hall. A collaboration of six companies, two universi-

⁵Grafana Labs 2021, <https://grafana.com> (accessed September 7, 2021)

⁶opticlock consortium, <https://www.opticlock.de/en> (accessed September 7, 2021)

ties, one research and one federal institute has been developing a robust, highly available and easy-to-use optical clock that is meant to be operated outside a specialized laboratory. The clock is based on the E2 transition in $^{171}\text{Yb}^+$ and the identical trap design as in Yb3 is used, with one significant difference: The molybdenum trap electrodes are not gold-coated but only polished, as shown in figure 2.7 on the upper left side. Since mid-2020, the standalone clock is operational. It consists of two 19 inch racks as shown in figure 2.7 right hand side. First comparisons between opticlock and the laboratory systems have been performed, details for the Yb3-opticlock comparison will be given in section 3.7.

2.3 Evaluation of the uncertainty contributions

In the pursuit of the ideal, unperturbed atomic reference, a meticulous investigation of the experimental conditions affecting the ion has to be performed. This includes an assessment of the rf fields for trapping, the laser light for the atom interrogation, and the thermal environment. The frequency realized by the local oscillator can only be an estimate of the unperturbed transition frequency, based on the evaluation of known frequency shift effects. These shifts along with their estimated uncertainty are combined in an uncertainty budget that provides a measure for the accuracy of the atomic clock. In the following, the individual contributions to the Yb3 uncertainty budget will be discussed in detail before a summary is given at the end of this section.

2.3.1 Quadratic Stark shift

The Stark effect describes the interaction of an atom with an electric field, a situation encountered several times when dealing with an ion clock: It plays a role for the blackbody radiation shift, the dc Stark shift of the trapping field, and the light shift related to laser excitation, all of which will be discussed in this section. As the Stark effect is the basis for all of these perturbations, it is introduced here in a separate paragraph. The interaction is described by the Stark Hamiltonian

$$H_S = -\mathbf{p}\mathbf{E}, \quad (2.1)$$

with \mathbf{p} the electric dipole moment operator and \mathbf{E} the electric field. Since there is no linear Stark effect for atomic levels of defined parity, in lowest order the quadratic Stark effect has to be considered. Treatment in second-order perturbation theory leads to the expression of the quadratic Stark shift [81, 82]

$$\begin{aligned} \Delta W_{\text{QS}} &= -|\mathbf{E}|^2 \left[\frac{\alpha_S}{2} + \gamma(F, m_F) \frac{\alpha_T}{4} (3 \cos^2 \beta - 1) \right], \\ \gamma(F, m_F) &= \frac{3m_F^2 - F(F+1)}{F(2F-1)} \end{aligned} \quad (2.2)$$

for the energy of an individual atomic level, with $\alpha_S(\lambda)$ and $\alpha_T(\lambda)$ the wavelength-dependent scalar and tensorial polarizability, and β the angle between the ion's quantization axis defined by an external magnetic field and the electric field vector. The prefactor $\gamma(F, m_F)$ depends on the quantum numbers of the state and one finds $\gamma(0, 0) = 0$, $\gamma(2, 0) = 1$ and $\gamma(3, 0) = 4/5$ for the $^2\text{S}_{1/2}$, $^2\text{D}_{3/2}$ and $^2\text{F}_{7/2}$ state, respectively. The polarizability of an atomic state a can be expressed by

$$\alpha_a \propto \sum_b \frac{f_{ab}}{\omega_{ab}^2 - \omega^2}, \quad (2.3)$$

where the dimensionless weighting factor f_{ab} is called the oscillator strength of the transition $a \rightarrow b$, ω_{ab} is the corresponding frequency, and ω denotes the frequency of the applied electric field [83]. For $^{171}\text{Yb}^+$, a detailed discussion of the oscillator strengths can be found in [42]. The shift of the clock transition frequencies is calculated from the differential polarizabilities $\Delta\alpha_S$ and $\Delta\alpha_T$ of the two involved states. A first example of a quadratic Stark shift relevant for the ion clock is given in the following.

2.3.2 Blackbody radiation shift

The largest frequency correction for the Yb^+ clocks at PTB is attributed to the blackbody radiation (BBR) shift resulting from the room temperature environment. For Yb^+ , it also leads to the largest contribution for the systematic uncertainty. Using equation (2.2) and assuming an isotropic perturbation, i.e. the tensorial part to average out, the electromagnetic blackbody radiation yields a frequency shift of the form

$$\Delta\nu_{\text{BBR}} = -\frac{1}{2h} \Delta\alpha_S^{\text{dc}} \langle E_{\text{BBR}}^2(T) \rangle (1 + \eta(T)). \quad (2.4)$$

Since the blackbody radiation spectrum is located in the mid-infrared with a peak around 10 μm at room temperature, the scalar differential polarizability is approximated by its dc value $\Delta\alpha_S^{\text{dc}}$ with a dynamic correction term η [84]. For the Yb^+ ion, $\eta_{\text{E}2}(298 \text{ K}) = 0.13(3)$ and $\eta_{\text{E}3}(298 \text{ K}) = 0.0025(2)$ are found [85]. The main contributions to the BBR shift uncertainty, given by the uncertainties of the mean squared field and of the static scalar differential polarizability, will be individually addressed in the following.

Mean squared field. The mean squared field, derived from Planck's radiation law, takes the form [86]

$$\langle E_{\text{BBR}}^2(T) \rangle = \frac{8\pi^5(k_B T)^4}{15c^3 h^3 \epsilon_0} = \left(831.94 \frac{\text{V}}{\text{m}}\right)^2 \left(\frac{T}{300 \text{ K}}\right)^4. \quad (2.5)$$

As can be seen by the fourth power dependence of the temperature T , the shift can be significantly reduced in a cryogenic setup, however, this poses different experimental challenges such as reduced optical access or vibrations from the cooling system. Instead, the shift is evaluated at room temperature, since the uncertainty can be kept small as long as the BBR field is homogeneous. For Yb1 and Yb2, MACOR spacers in the trap setup heat up due to dissipated rf power. For Yb3, fused silica spacers with lower dielectric loss are employed. The values for the loss tangent of MACOR and fused silica vary in the literature and depend on the frequency of the electric field. For typical ion trap conditions, $\tan \delta = 0.15 \times 10^{-4}$ for fused silica and $\tan \delta \approx 10 \times 10^{-4}$ for MACOR [87]. Installing fused silica instead of MACOR spacers results in a reduction of the dissipated thermal power and a lower trap temperature.

This has been experimentally verified using a thermographic camera and comparing the temperature of the Yb1 and Yb3 trap without and with the rf drive applied, as shown in figure 2.8. For Yb1, it is clearly visible that the insulators (marked by a white arrow) heat up significantly with respect to the other trap parts when the rf drive is applied. This observation has been confirmed in an FEM simulation performed for the specific trap geometry and materials [87], yielding a temperature rise due to the rf drive of 2.1(1.3) K.

In the analysis of these images, care needs to be taken of the high reflectivity (i.e. low emissivity) of metal surfaces, making them appear in reflected radiation rather than in their proper thermal emission. For Yb3, a massive

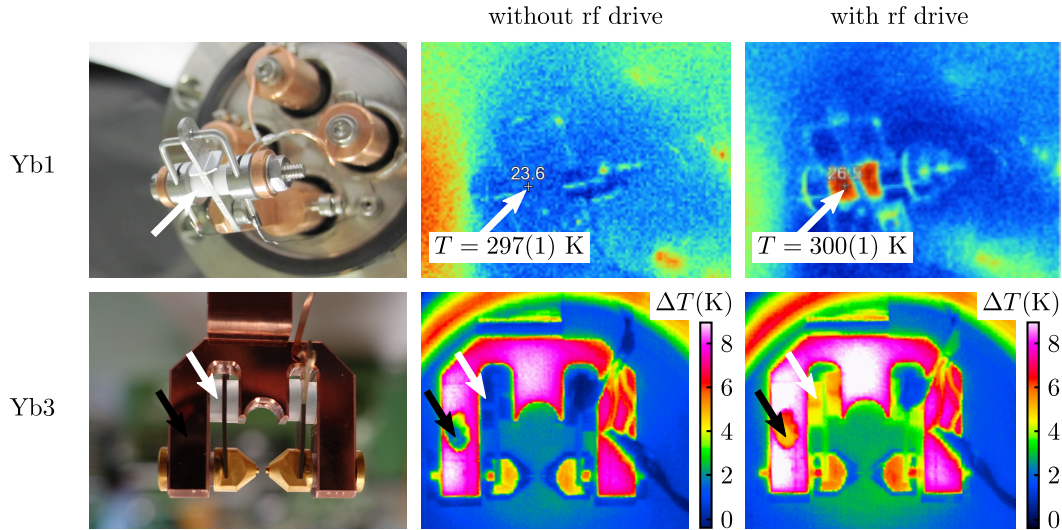


Figure 2.8: **Temperature of the ion traps.** Shown are infrared pictures of the Yb1 and Yb3 traps, both without and with the rf drive applied. White arrows mark the position of the insulators, which heat up significantly in the case of Yb1 when the rf drive is applied. For Yb3, a black dot of paint on the copper mount (marked by the black arrow) permits a comparison of the copper and insulator temperature, for which no significant temperature difference is observed. The right hand side insulators in Yb3 are partially obstructed by a thin copper plate.

copper mount is used to supply the rf trap voltage to the gold-coated endcap electrodes. A high emissivity coating has been applied on the left copper handle marked in the picture by a black arrow. Comparing the trap without and with the rf drive applied, a homogeneous temperature of copper mount and insulator is found. It should be noted that the insulator on the right hand side is partially obstructed by a copper ground connection. The temperature rise is estimated to be $1.0(0.5)$ K.

A temperature sensor placed inside the double-sided μ -metal shielding shows that the ambient temperature of the Yb3 physics package is $5.4(0.5)$ K higher compared to the laboratory temperature, which is typically at $296.4(0.5)$ K. The contributions to the BBR shift uncertainty resulting from the uncertainty in the temperature are $u_{\text{BBR (temp), E2}}/\nu_{\text{E2}} = 4.8 \times 10^{-18}$ for the E2 and $u_{\text{BBR (temp), E3}}/\nu_{\text{E3}} = 7 \times 10^{-19}$ for the E3 transition frequency. This corresponds to a reduction of about a factor of two in each case compared to Yb1. Several temperature sensors have been prepared to monitor the temperature at different positions of the system, which will even permit the detection of

temperature gradients. In particular, the temperature of the dc trap electrodes will be assessed outside the vacuum chamber with a PT100 sensor during clock operation in order to reduce the temperature contribution to the BBR shift uncertainty further.

Static scalar differential polarizability. As explained in the last section, the differential polarizability describes the coupling strengths of the clock transition levels to off-resonant dipole-allowed transitions. The polarizability can be assessed by introducing laser light at different wavelengths to the ion during the spectroscopy pulse and measuring the resulting light shift, as presented for $^{171}\text{Yb}^+$ in [33]. Such an experiment is explained in detail in section 4.3 for the measurement of the magic wavelength of the E3 transition. A main disadvantage of this method is the need for good knowledge of the laser intensity at the ion position, which in turn requires careful modeling of the beam profile and precise determination of the laser power. The corresponding uncertainty is limited to the percent level, as different groups have reported independently [33, 85, 88]. For the dc differential polarizabilities of the Yb^+ clock transitions, the values

$$\begin{aligned}\Delta\alpha_{S,E2}^{\text{dc}} &= 5.89(30) \times 10^{-40} \text{J m}^2 \text{V}^{-2}, \\ \Delta\alpha_{S,E3}^{\text{dc}} &= 0.888(16) \times 10^{-40} \text{J m}^2 \text{V}^{-2}\end{aligned}$$

are obtained [33, 85]. For the E3 transition, this results in a relative uncertainty contribution of $u_{\text{BBR (pol), E3}}/\nu_{\text{E3}} = 1.3 \times 10^{-18}$. For the E2 transition, a measurement of the differential polarizability at 7 μm wavelength is used to infer an estimate of the BBR shift at a temperature of 298 K in [85]: $\Delta\nu_{\text{BBR,E2}}(298 \text{ K}) = -338(12) \text{ mK}$. The shift uncertainty of about 3.5 % is attributed to the uncertainty in the polarizability. Typical room temperature shifts are given by

$$\Delta\nu_{\text{BBR,E2}}(T) = \Delta\nu_{\text{BBR,E2}}(298 \text{ K}) \left(\frac{T}{298 \text{ K}} \right)^4. \quad (2.6)$$

Combining the results for polarizability and trap temperature, the following fractional frequency shifts and uncertainty contributions due to blackbody

radiation are calculated for Yb3:

$$\frac{\Delta\nu_{\text{BBR, E2}}}{\nu_{\text{E2}}} = -517(18) \times 10^{-18},$$

$$\frac{\Delta\nu_{\text{BBR, E3}}}{\nu_{\text{E3}}} = -73.6(1.5) \times 10^{-18}.$$

The uncertainty of the E3 transition frequency is mainly limited by the uncertainty of the differential polarizability, which can be significantly reduced following an alternative approach: For atomic species with a negative differential polarizability, the static scalar differential polarizability can be assessed from the measurement of a so-called magic rf drive frequency, for which second-order Doppler shift due to excess micromotion and trap related quadratic Stark shift cancel each other [86]. Such a frequency measurement has been performed with one order of magnitude lower relative uncertainty in $^{88}\text{Sr}^+$ as compared to the intensity measurements presented above. An even lower uncertainty has been reported in $^{40}\text{Ca}^+$, with a fractional uncertainty of the differential static scalar polarizability of 2.9×10^{-4} [89].

Trapping both an Yb^+ and a Sr^+ ion in a linear trap, light shift measurements at the blackbody radiation spectrum around 10 μm can be performed with a CO_2 laser, with Sr^+ acting as a probe for the laser intensity. Shuffling the two ions separately in and out of the beam, the low fractional uncertainty of the polarizability for Sr^+ can be transferred to Yb^+ . Thereby, it is expected to reduce the relative uncertainty due to the polarizability by one order of magnitude, that would yield $u_{\text{BBR (pol), E3}}/\nu_{\text{E3}} = 2 \times 10^{-19}$. The total BBR shift uncertainty would then be limited by the current value of $u_{\text{BBR (temp), E3}}$, which is also expected to be further reduced with better assessment of the trap temperature.

In order to perform a measurement of the scalar differential polarizability, a linear trap is taken into operation in the clock hall at PTB. At the current status, Yb^+ and Sr^+ can be trapped and spectroscopy of the electric quadrupole transitions of both ions is performed.

2.3.3 Second-order Doppler and quadratic dc Stark shift

There are two frequency shift effects related to the motion of the ion within the trap: the Doppler shift and the quadratic dc Stark shift.

Second-order Doppler shift. The Doppler effect can be described as a relative difference of the laser frequency ν' in the rest frame of the ion and ν in the laboratory frame, for the velocity v_{\parallel} of the ion parallel to a probe laser beam:

$$\frac{\nu'}{\nu} = \gamma \left(1 - \frac{v_{\parallel}}{c}\right), \quad \gamma = \frac{1}{\sqrt{1 - v^2/c^2}}. \quad (2.7)$$

If no other shift effect is present and the probe laser is locked to the atomic reference, the laser frequency in the ion rest frame averaged over the probe duration is the unperturbed atomic transition frequency, $\langle \nu' \rangle = \nu_0$. Further it is assumed that $\nu = \langle \nu \rangle$, i.e. the laser frequency in the laboratory frame is constant over the probe duration, and $v_{\parallel} \ll c$. Then the Doppler shift can be written as [11]

$$\frac{\Delta\nu_D}{\nu_0} = \frac{\nu - \nu_0}{\nu_0} = \frac{\langle \nu \rangle}{\langle \nu' \rangle} - 1 = \frac{\langle v_{\parallel} \rangle}{c} - \frac{\langle v^2 \rangle}{2c^2} + \frac{\langle v_{\parallel} \rangle^2}{2c^2} + \mathcal{O}\left(\frac{v^3}{c^3}\right). \quad (2.8)$$

Slow drifts of the mean ion position with respect to the laser, for example due to thermal expansion or slowly varying electric fields, may lead to a non-vanishing first-order contribution, an effect discussed later in this section. For now, motion due to the trap drive at secular frequencies of hundreds of kHz and rf drive frequencies of several MHz are investigated. The oscillatory motion of the trapped ion is described by equation (1.5) and is at frequencies > 100 kHz. Consequently, on timescales of typical clock pulses (> 10 ms), $\langle v_{\parallel} \rangle = 0$ and only the second term needs to be taken into account. One finds with equation (1.13)

$$\frac{\Delta\nu_D}{\nu_0} = -\frac{E_{\text{kin}}}{mc^2} = -\sum_i \left(\frac{k_B T_i}{mc^2} + \frac{1}{4} \left(\frac{ka_{e,i} \Omega_{\text{rf}}}{kc} \right)^2 \right). \quad (2.9)$$

Further, one can introduce $\sum_i a_{e,i}^2 = a_e^2$ and the modulation index

$$\beta = \mathbf{k} \mathbf{a}_e = ka_e \cos \theta \quad (2.10)$$

with a_e the amplitude of excess micromotion and its orientation with respect to the laser propagation vector \mathbf{k} expressed by the angle θ . For thermal equilibrium and at the Doppler limit, $T_x = T_y = T_z = T_D$. This yields

$$\frac{\Delta\nu_D}{\nu_0} = - \left(\frac{3k_B T_D}{mc^2} + \frac{1}{4} \left(\frac{\beta\Omega_{\text{rf}}}{2\pi\nu_0 \cos\theta} \right)^2 \right). \quad (2.11)$$

Quadratic dc Stark shift. According to equation (1.4), the electric field at the trap center is zero. However, if the ion is displaced from the trap minimum, it is exposed to a time-dependent electric field. Due to the fast oscillatory motion of the ion in the trap, the electric field can be averaged on timescales of typical clock pulses (> 10 ms). For the mean electric field exposed to the ion, one finds [48]

$$\langle E^2 \rangle = \frac{3k_B T_D m \Omega_{\text{rf}}^2}{e^2} + 2 \left(\frac{\beta m \Omega_{\text{rf}}^2 c}{4\pi\nu_0 e \cos\theta} \right)^2, \quad (2.12)$$

which can be inserted into equation (2.2) for the quadratic dc Stark shift

$$\frac{\Delta\nu_{\text{QS}}}{\nu_0} = - \frac{\Delta\alpha_S^{\text{dc}}}{h\nu_0} \left(\frac{3k_B T_D m \Omega_{\text{rf}}^2}{2e^2} + \left(\frac{\beta m \Omega_{\text{rf}}^2 c}{4\pi\nu_0 e \cos\theta} \right)^2 \right). \quad (2.13)$$

There are two important things to point out about equations (2.11) and (2.13):

- (1) As noted in the last section, with some ions the differential static scalar polarizability can be measured through a magic rf drive experiment; this is easy to see here: If $\Delta\alpha_S^{\text{dc}} < 0$ as for example in $^{88}\text{Sr}^+$, Doppler and quadratic Stark shift have opposite sign and compensate each other for a specific Ω_{rf} .
- (2) The first term in both equations is the combination of secular motion and intrinsic micromotion, both of which contribute equally to the shift and are related to the temperature of the ion. The second term denotes excess micromotion, which is driven by the trapping field. As both terms are assessed by different experiments, they will be treated independently in the following section.

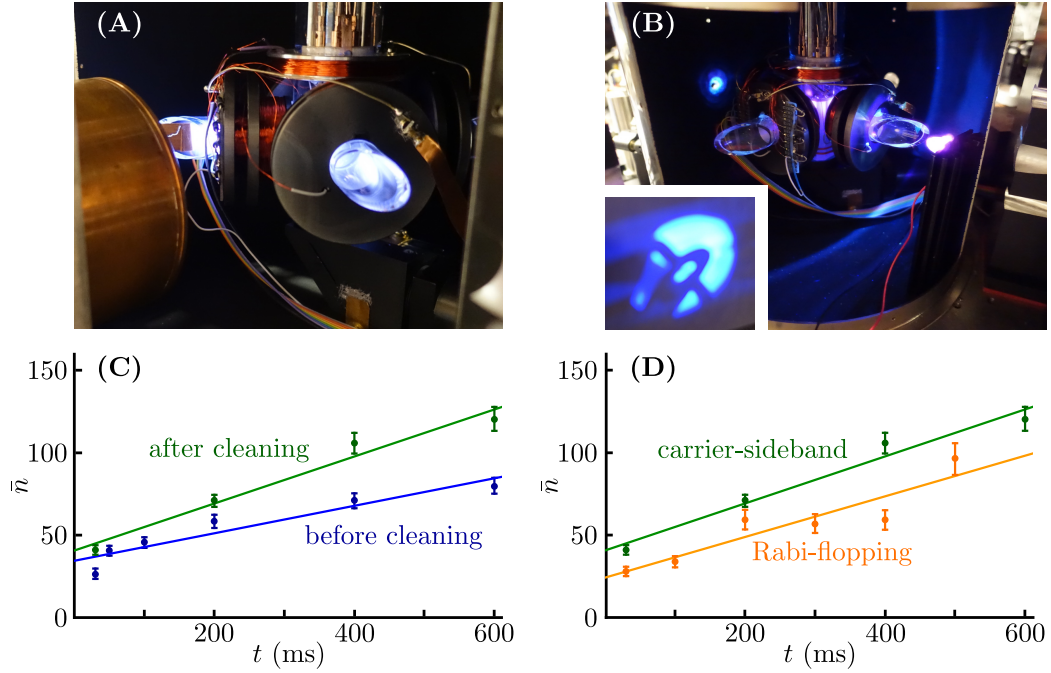


Figure 2.9: **Investigation of the Yb1 heating rate.** (A) Plasma cleaning of the trap electrodes. (B) Removing of patch charges on the electrode surfaces using UV light. The inset shows the trap shadow. (C) Heating rate before (blue) and after (green) the cleaning tests. The procedures did not lead to an improvement, the heating rate is even slightly higher afterwards. (D) A comparison of the Rabi-flopping (orange) and carrier-sideband (green) method for the heating rate assessment shows that both methods yield a similar rate with different offset. The offset is assumed to be related to only taking the sidebands ω_x and ω_y into account for the carrier-sideband method.

2.3.4 Ion motion

The equations for second-order Doppler and quadratic dc Stark shift derived in the last section can be used to quantify the shift effects due to ion motion.

Thermal motion is related to the ion temperature. In section 1.4, two experiments for the measurement of the ion temperature have been introduced, the carrier-sideband (c-s) and the Rabi-flopping (R-f) method. Both methods will be used to compare heating rates of Yb1, Yb3 and optclock.

For Yb1, attempts have been made to improve the heating rate by in-situ plasma cleaning using an argon-hydrogen gas mixture as shown in figure 2.9 (A). In order to reduce patch charges after the cleaning, the trap has been illuminated with UV light as shown in figure 2.9 (B). However, compari-

son of the heating rate before and after the treatment shows that the procedure was not successful and the heating rate even degraded:

$$\bar{n}_{\text{c-s, before}}(t) = 83(14) \times t/\text{s} + 35(4), \quad (2.14)$$

$$\bar{n}_{\text{c-s, after}}(t) = 143(18) \times t/\text{s} + 41(7). \quad (2.15)$$

Here, the carrier-sideband method has been employed for the combination of the first-order secular sidebands ω_x and ω_y which are at frequencies of $2\pi \times 605(5)$ kHz. A heating rate measurement performed seven months after the cleaning procedure using the Rabi-flopping method yields a similar result:

$$\bar{n}_{\text{R-f}}(t) = 123(26) \times t/\text{s} + 24(8). \quad (2.16)$$

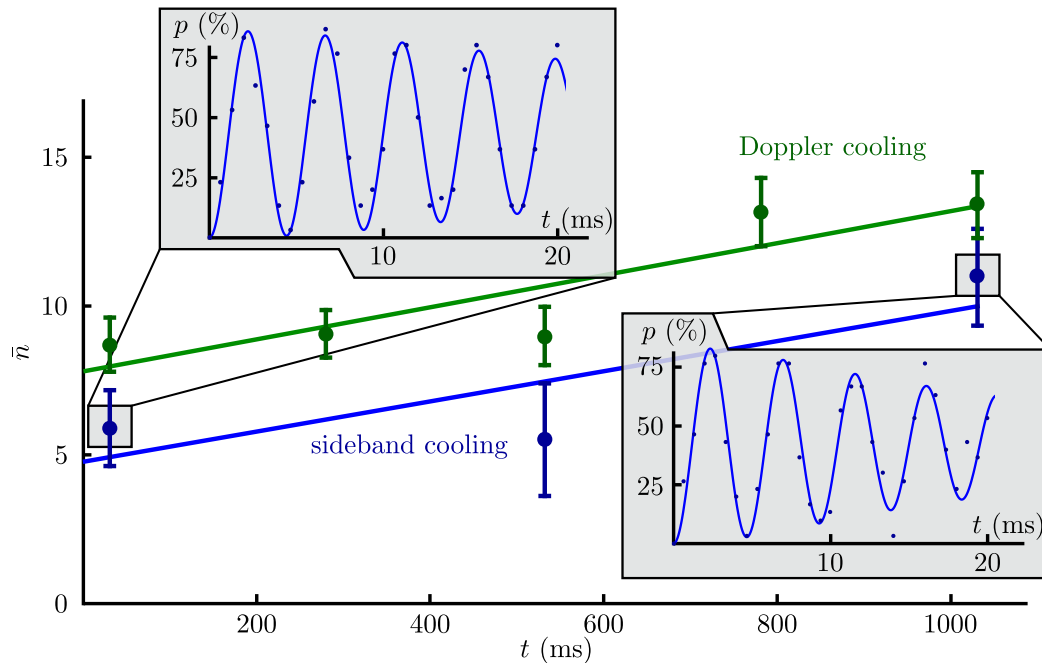
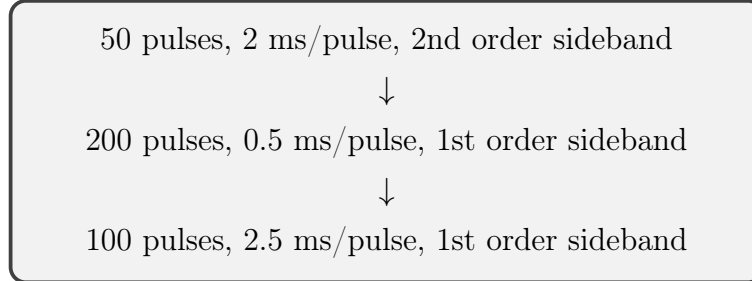


Figure 2.10: **Yb3 heating rate.** The heating rate of Yb3 is assessed using the Rabi-flopping method. The green data points are measured with Doppler cooling only, for the blue data points additional sideband cooling is introduced. The insets show Rabi-flopping signals at 30 ms and 1030 ms after the cooling.

For Yb3, heating rate measurements were only conducted using the Rabi-flopping method. As the heating rate has been found to be much lower, further improvements have been attempted by extending the Doppler cooling (D) to additional sideband cooling (SB) on the E2 clock transition. With a power

from the E2 transition clock laser of about 10 μW and the first-order secular sideband ω_x at about $2\pi \times 780$ kHz, the following pulse sequence has been used for the heating rate measurement:



The pulse lengths are chosen to yield a pulse area close to π at the beginning of each of the three steps of the sequence. The pulse duration is limited by the power of the E2 transition clock laser. The application of sideband cooling improves upon the lowest achievable motional quantum number:

$$\bar{n}_D(t) = 5.6(1.6) \times t/s + 7.7(1.0), \quad (2.17)$$

$$\bar{n}_{\text{SB}}(t) = 5.1(3.4) \times t/s + 4.8(2.3). \quad (2.18)$$

The Doppler cooling limit $\bar{n}_D(0)$ is in agreement with the theoretical Doppler limit $\bar{n}_D = 8.5$ derived in section 1.4.3. Compared to the other Yb^+ systems in the clock hall, the heating rate is much lower. This can be directly attributed to the gold coating of the electrodes, as the identical trap in the optically clock system employing polished molybdenum trap electrodes shows a much higher heating rate of

$$\bar{n}_{\text{optically clock}}(t) = 60(4) \times t/s + 19(3). \quad (2.19)$$

Using only Doppler cooling and with a typical clock cycle length of 70 ms for the E2⁷ and 450 ms for the E3⁸ transition, a mean quantum number of $\bar{n}_{\text{E2}} = 8.0(1.1)$ and $\bar{n}_{\text{E3}} = 9.0(1.9)$ during atom-laser interrogation is found for Yb^+ . The corresponding contributions to the second-order Doppler and quadratic dc Stark shift with the respective uncertainties are deduced from the first terms in equations (2.11) and (2.13) and are listed in table 2.1.

⁷A 40 ms clock pulse follows 30 ms settling time.

⁸After 30 ms settling time, a hyper-Ramsey sequence with $\tau_\pi = 60$ ms and $T_{\text{Dark}} = 300$ ms is employed.

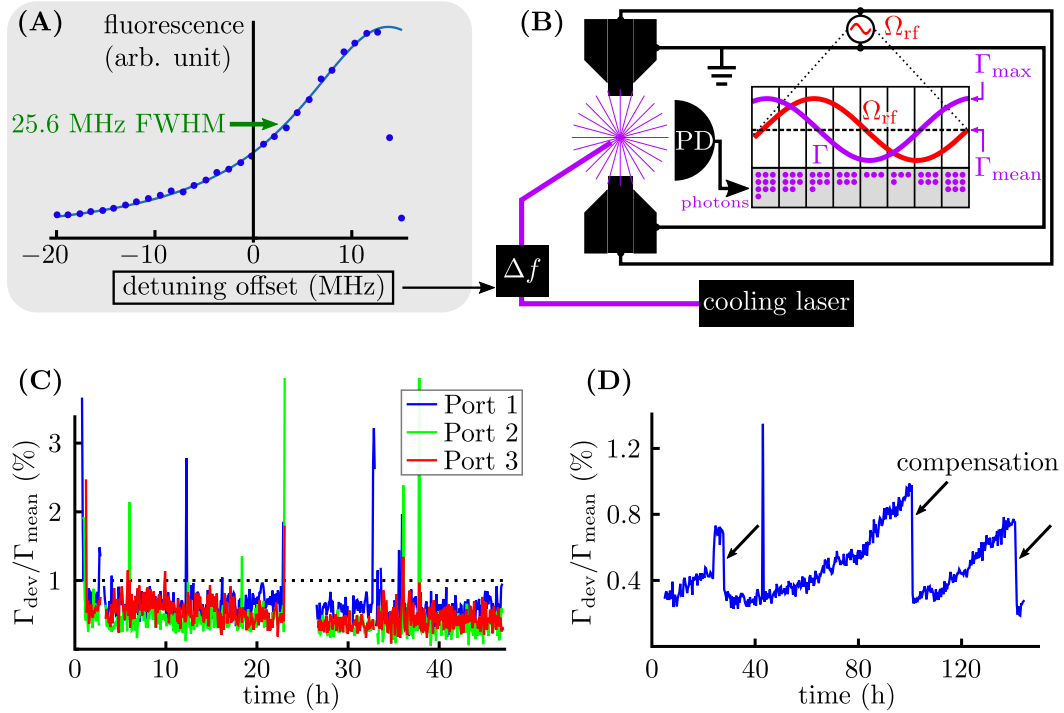


Figure 2.11: **Yb3 micromotion detection.** (A) Line profile of the cooling transition with a natural linewidth $\gamma = 2\pi \times 19.60(5)$ MHz [70]. For maximum cooling efficiency and highest sensitivity to ion motion, the frequency is locked to the full width at half maximum (FWHM) position. (B) Schematic of the micromotion assessment using the photon correlation method. The fluorescence signal picked up by the photodiode PD is measured and correlated to the trap drive frequency Ω_{rf} with a lock-in amplifier. A sinusoidal variation in the fluorescence signal Γ indicates a first-order Doppler shift of the ion with respect to the cooling laser beam, from which micromotion can be inferred. The mean photon number is Γ_{mean} , the maximum photon number is Γ_{max} and $\Gamma_{\text{dev}} = \Gamma_{\text{max}} - \Gamma_{\text{mean}}$. (C) Relative photon correlation signal amplitude $\Gamma_{\text{dev}}/\Gamma_{\text{mean}}$ monitored over several hours along all three cooling laser ports. The signal remains below 1%. The sharp peaks are related to loss of the fluorescence signal, when no reasonable photon correlation signal can be extracted. (D) Relative photon correlation signal amplitude monitored along one cooling laser direction for several days. The signal is slowly increasing over time and micromotion is compensated at times marked by the black arrows by adjusting the voltages on the compensation electrodes. The sharp peak at about 50 h is related to loss of the fluorescence signal.

	thermal motion		excess micromotion		total	
	E2	E3	E2	E3	E2	E3
2nd-order Doppler	-7(2)	-8(2)	-0.3(1.1)	-0.3(1.2)	-7(2)	-8(2)
quadratic dc Stark	-8(1)	-1.4(0.2)	-1.1(2.9)	-0.1(0.5)	-8(3)	-1.5(0.5)
total	-14(2)	-9(2)	-1.0(3.1)	-0.4 (1.3)	-15(4)	-10(2)

Table 2.1: **Contributions due to ion motion** to the E2 and E3 systematic uncertainty. All shifts are given in fractional frequency units divided by 10^{-19} .

Excess micromotion is described by the second term in both equations (2.11) and (2.13). It is motion of the ion at the frequency of the rf drive. On timescales of the trap drive frequency, a first-order Doppler effect arises which proves to be a useful tool to monitor the excess micromotion:

$$\frac{\Delta\nu_D}{\nu_0} = \frac{\Delta\omega_D}{\omega_0} = \frac{v_{\parallel}}{c}. \quad (2.20)$$

The term of the excess micromotion in equation (1.5) is used to determine

$$v_{\parallel} = \dot{r} \cos \theta = a_e \Omega_{\text{rf}} \cos(\Omega_{\text{rf}} t + \phi) \cos \theta. \quad (2.21)$$

The maximum frequency deviation $\Delta\omega_{D,\text{max}}$ is found at times $\cos(\Omega_{\text{rf}} t + \phi) = 1$:

$$\Delta\omega_{D,\text{max}} = \frac{\omega_0}{c} a_e \Omega_{\text{rf}} \cos \theta = k a_e \Omega_{\text{rf}} \cos \theta = \beta \Omega_{\text{rf}} \quad (2.22)$$

Furthermore, the photon count rate $\Gamma = \gamma p_e$ gives, in combination with equation (1.36),

$$\Gamma = \frac{\Omega^2 \gamma}{\gamma^2 \left(1 + \frac{4\delta^2}{\gamma^2}\right)}. \quad (2.23)$$

For optimal Doppler cooling, a detuning $\delta = -\gamma/2$ for the cooling laser is chosen, as derived in section 1.4.3. For a small periodic frequency shift with amplitude $\Delta\omega_{D,\text{max}}$ around that detuning, $\delta_{\text{max}} = -\gamma/2 + \Delta\omega_{D,\text{max}}$, the maximum change in the fluorescence rate is

$$\Gamma_{\text{max}} = \frac{\Omega^2}{2\gamma} \frac{1}{1 - 2\frac{\Delta\omega_{D,\text{max}}}{\gamma} + 2\left(\frac{\Delta\omega_{D,\text{max}}}{\gamma}\right)^2} \approx \frac{\Omega^2}{2\gamma} \left(1 + 2\frac{\Delta\omega_{D,\text{max}}}{\gamma}\right). \quad (2.24)$$

The geometric series expansion has been used and second and higher order contributions have been neglected since $\Delta\omega_{D,\text{max}} \ll \gamma$. The mean fluorescence

rate around which the fluorescence signal is modulated is given by

$$\Gamma_{\text{mean}} = \Gamma(\delta = -\gamma/2) = \frac{\Omega^2}{2\gamma}. \quad (2.25)$$

Γ_{mean} and Γ_{max} are visualized in figure 2.11 (B). The relative change in fluorescence is given by

$$\frac{\Gamma_{\text{max}}}{\Gamma_{\text{mean}}} = \left(1 + 2 \frac{\Delta\omega_{\text{D,max}}}{\gamma} \right) \quad (2.26)$$

and leads to

$$\Delta\omega_{\text{D,max}} = \left(\frac{\Gamma_{\text{max}}}{\Gamma_{\text{mean}}} - 1 \right) \frac{\gamma}{2}. \quad (2.27)$$

With $\Gamma_{\text{dev}} = \Gamma_{\text{max}} - \Gamma_{\text{mean}}$ and $\Delta\omega_{\text{D,max}} = \beta\Omega_{\text{rf}}$ from equation (2.22), a relation between variations of the fluorescence signal and the modulation index β is found [48]:

$$\frac{\Gamma_{\text{dev}}}{\Gamma_{\text{mean}}} = \frac{2\beta\Omega_{\text{rf}}}{\gamma}. \quad (2.28)$$

This result is valid for $\Omega_{\text{rf}} \ll \gamma$. However, in the case of the Yb single-ion clocks at PTB, $\Omega_{\text{rf}} \approx 2\pi \times 13$ MHz and $\gamma = 2\pi \times 19.6$ MHz. From a more generalized expression discussed in [90], deviations between the theoretical model derived above and the experimental conditions can be visualized as shown in figure 2.12: For $\Omega_{\text{rf}} \ll \gamma$ (blue dashed line), the maximum of the photon correlation signal is at $\delta = -\gamma/2$ and at that detuning, the generalized expression in [90] yields the same result as given in equation (2.28). For a trap frequency and a linewidth as employed in the Yb⁺ setups (red solid line), the maximum is shifted and at $\delta = -\gamma/2$, about 75 % of the maximum photon correlation amplitude is found. The theoretical prediction is confirmed by experimental data (red dots). Thus, equation (2.28) can still be used to calculate the modulation index, but the reduced photon correlation signal at $\delta = -\gamma/2$ needs to be taken into account.

By correlating the photon count rate with the rf trap drive, a sinusoidal signal with relative amplitude $\Gamma_{\text{dev}}/\Gamma_{\text{mean}}$ is retrieved as shown in figure 2.11, from which the modulation index can be assessed. The shift due to excess micromotion is calculated according to the equations (2.11) and (2.13). In Yb3, the large optical access enables the installation of three independent cooling beams to monitor and correct micromotion in 3D. Once micromotion is corrected, the amplitude of the photon correlation signal can stay below 1 % for

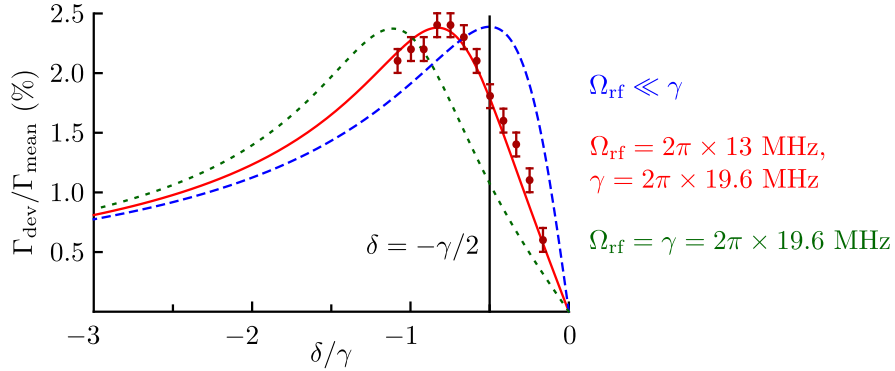


Figure 2.12: **Relative photon correlation signal at different trap frequencies.** The theoretical curves are derived from a model given in [90]. The cooling laser is placed at a detuning $\delta = -\gamma/2$ from resonance for optimal Doppler cooling. For $\Omega_{\text{rf}} \ll \gamma$ (blue dashed line), the model agrees with the theoretical prediction in [48]. The red solid line represents the experimental conditions in the Yb^+ traps at PTB, for which the maximum is shifted and at $\delta = -\gamma/2$, about 75 % of the maximum photon correlation signal is found. The experimental data points in red confirm the theoretical prediction. The green dotted line shows the behavior for $\Omega_{\text{rf}} = \gamma$. For the red curve, $\beta = 0.018$ is chosen to reproduce the relative photon correlation signal obtained experimentally. The amplitudes of the blue dashed and green dotted line are adapted to yield the same micromotion velocities in all three cases for better comparison.

several hours, as shown in figure 2.11 (C) and (D). When performing clock operation, excess micromotion is monitored by evaluating the fluorescence signal during the cooling periods. An automatic correction scheme ensures that micromotion is kept at that level. The scheme is based on changing the voltages on the compensation electrodes (introduced in figure 1.2) and measuring the resulting photon correlation signal to obtain the optimal compensation voltage setting. Clock operation is paused when this procedure is active.

The frequency contributions to both second-order Doppler and quadratic dc Stark shift are shown in table 2.1. The total shift due to secular and driven motion for the Yb^3 system amounts to

$$\frac{\Delta\nu_{\text{mot, E2}}}{\nu_{\text{E2}}} = -1.5(0.4) \times 10^{-18},$$

$$\frac{\Delta\nu_{\text{mot, E3}}}{\nu_{\text{E3}}} = -1.0(0.2) \times 10^{-18}$$

for the E2 and E3 transition, respectively.

2.3.5 Variation of dc electric fields

It has been observed that large amounts of UV light, as for example present in the fluorescent lamps of the room light, can lead to rapid changes of the micromotion, which might be attributed to charges moving on the vacuum viewport surfaces. This effect is shown in figure 2.13 (A), where the room light has been switched on at $t = 5$ min. With the chamber inside the double layer μ -metal shielding and the optical table covered by a black curtain, this effect can be completely suppressed. However, the cooling laser light at 370 nm causes a similar effect, which has been verified by introducing light from an LED at that wavelength to the trap, leading to rapid changes of the photon correlation signal.

This has significant consequences during clock operation, as shown in figure 2.13 (B). Here, the micromotion amplitude is optimized for clock operation. Before clock operation, the ion is constantly cooled without interruptions for clock interrogation. This leads to a high photon correlation signal (at $t = 0$ h). Once clock operation has started, the micromotion slowly creeps to the optimized level of below 1 % amplitude. If the ion is dark for some time and constant cooling is switched on again, the signal worsens as becomes measurable once the clock cycles restart.

The direct effect of the laser light on the electric field of the ion poses a large issue as it may lead to a first-order Doppler effect that is roughly estimated in the following: With equation (2.10) and the laser propagation vector as well as the micromotion oriented along the x axis, the modulation index can be expressed by

$$\beta = ka_e = kr_e \frac{q_x}{2}, \quad (2.29)$$

where r_e the ion displacement from the trap minimum and q_x the stability parameter (as described in section 1.4.1). The modulation index can be calculated from the photon correlation signal using equation (2.28). With figure 2.13 (B) a difference in the photon correlation signal of about 4 % is found between constant cooling and clock operation, where the cooling laser is switched off for about 90 % of the clock cycle. With the photon correlation signal obtained by the cooling laser ($\lambda = 370$ nm, $\gamma = 2\pi \times 19.6$ MHz) and with typical trapping parameters (rf voltage $V = 500$ V, $\Omega_{\text{rf}} = 2\pi \times 13$ MHz),

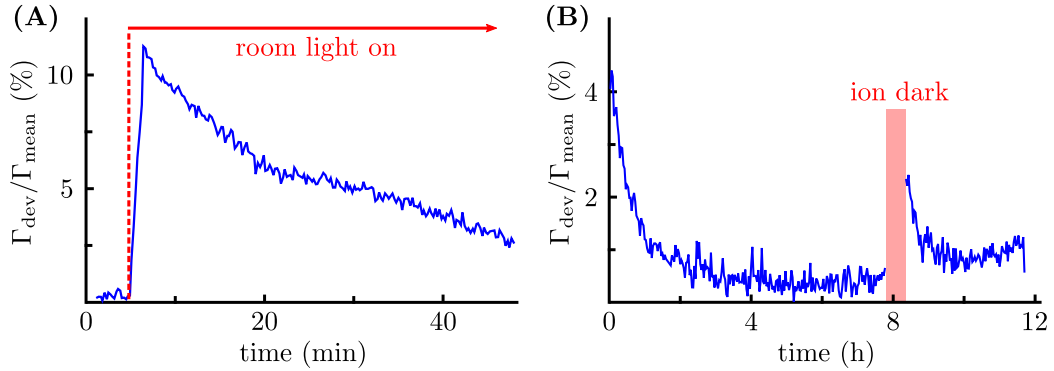


Figure 2.13: **Effect of light on the relative photon correlation amplitude.** (A) After compensation of micromotion, the fluorescent lamps of the room light have been switched on (at $t=5$ min), shining directly on the vacuum chamber viewports and leading to a large change in the photon correlation signal. With μ -metal shielding and additional covers, the physics package can be isolated from external light sources. (B) A similar effect is measurable when changing (at $t=0$ h) from constantly cooling the ion to clock operation, indicating a variation of the dc electric field due to the laser beams. After a running-in period, the signal stays constant. However, if the ion becomes dark and the constant cooling is activated (around $t=8$ h), the signal worsens again.

the ion displacement is calculated to $r_e \approx 35$ nm for 4 % of micromotion amplitude. The slow exponential decrease of the photon correlation signal in figure 2.13 (B) suggests that the ion position is drifting slowly (on timescales of minutes). However, it is the general observation that the dc electric fields vary on timescales of seconds. Therefore it is assumed that in figure 2.13 (B) only the change in the ion position averaged over the cooling period is measured, and that the actual ion motion within one clock cycle is significantly faster. To give an idea of the potential size of the first-order Doppler effect, it is assumed that during the E3 clock interrogation of 450 ms (during which the cooling laser is shut off), the ion moves by 10 % of r_e , i.e. by 3.5 nm. This yields an ion velocity $v = 8$ nm/s that appears cycle-synchronously. The corresponding first-order Doppler contribution for a laser parallel to the ion motion is about 3×10^{-17} , obtained with equation (2.8). This example demonstrates that first-order Doppler effects can severely influence clock comparisons at the 10^{-18} level.

The issues discussed are assumed to be related to difficulties during the Yb3 physics package assembly, during which solder has entered the vacuum

chamber, with the possibility of residues being deposited on the inner viewport side. To resolve the matter, it has been decided to replace the physics package since an identical system is used in optclock without observing these severe effects. The replacement has been fully prepared and is ready for installation into the setup. Further measures regarding first-order Doppler shifts can be taken by implementing shift suppression schemes such as providing clock laser light from different directions to the ion as performed in [37].

However, instead of investing time and effort into exchanging the physics package right away, it has been decided to first learn more about the new trap system and to focus on other experiments that can be conducted with the current setup despite the issues described. These experiments include tests of the tensorial shift suppression scheme explained in section 4.1 and the excitation of vortex beams discussed in section 4.5. Furthermore, first comparisons of Yb3 with the other systems have been performed as described in section 3.7.

2.3.6 Second-order dc Zeeman shift

A small magnetic field is applied externally to define the ion quantization axis. Great care needs to be taken to characterize the magnetic field strength and orientation at the ion position. The field is set by the currents of three pairs of coils oriented along the principal axes of the setup as shown in figure 2.3. Typically, a magnetic field with a strength of a few μT is employed. Another pair of coils provides a strong magnetic field of about 400 μT during the cooling period for appropriate splitting between the cooling transition Zeeman levels to avoid population trapping. A two-layer μ -metal shielding suppresses external influences on the magnetic field by three orders of magnitude. The magnetic field can be monitored precisely on the E2 transition: The ${}^2\text{S}_{1/2}(F=0)$ ground state energy with magnetic quantum number $m=0$ is first-order Zeeman insensitive, while the $m=1,2$ levels of the excited state ${}^2\text{D}_{3/2}(F=2)$ are first-order Zeeman sensitive and a frequency shift

$$\Delta\nu_{Z1} = \alpha_{Z1} B \times \Delta m, \quad (2.30)$$

$$\alpha_{Z1} = \frac{g_F \mu_B}{h} \quad (2.31)$$

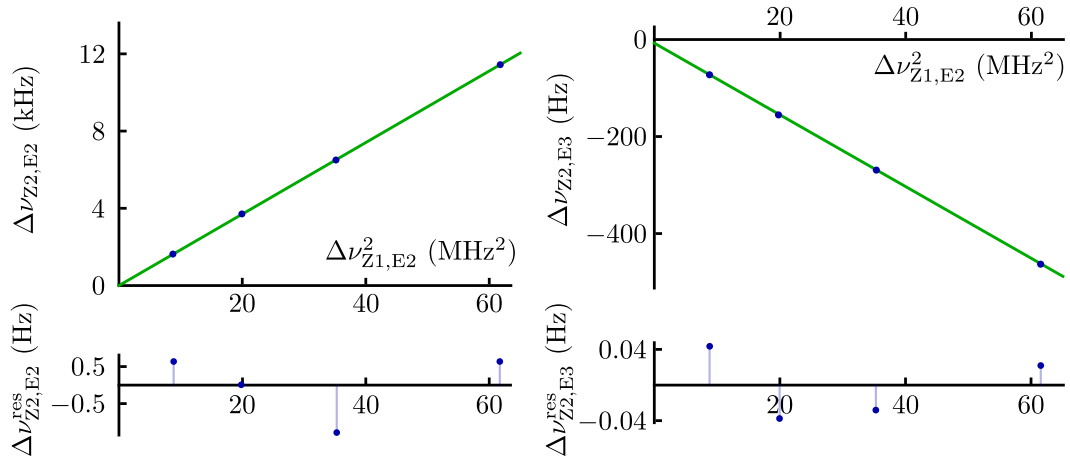


Figure 2.14: **Second-order Zeeman shift** $\Delta\nu_{Z2}$ of the $m_F = 0 \rightarrow m_F = 0$ magnetic sublevels, both for the E2 and E3 transition, in dependence of the first-order Zeeman shift $\Delta\nu_{Z1}$ of the $m_F = 0 \rightarrow m_F = 2$ sublevels of the E2 transition. The residuals $\Delta\nu_{Z2}^{\text{res}}$ are shown below.

is measurable when probing the $\Delta m = 1, 2$ transitions, with $g_F = 0.59930(9)$ the Landé g -factor of the $^2D_{3/2}(F=2)$ state [73] and μ_B the Bohr magneton. The clock transition with $\Delta m = 0$ is only second-order Zeeman sensitive,

$$\Delta\nu_{Z2} = \alpha_{Z2} B^2, \quad (2.32)$$

where α_{Z2} can be calculated using second-order perturbation theory [73]. With knowledge of the relative strength between first- and second-order Zeeman shift,

$$\frac{\Delta\nu_{Z2,k}}{\Delta\nu_{Z1,E2}^2} = \frac{1}{\Delta m^2} \frac{\alpha_{Z2,k}}{\alpha_{Z1,E2}^2} = \frac{1}{\Delta m^2} \alpha_{Z2/Z1,k}, \quad (2.33)$$

the shift of clock transition $k=E2, E3$ can be directly inferred from a measurement of the Zeeman frequency splitting on the E2 transition [91]. As shown in figure 2.14, the relative strengths

$$\alpha_{Z2/Z1,E2} = 7.410(4) \times 10^{-10} \frac{1}{\text{Hz}},$$

$$\alpha_{Z2/Z1,E3} = -2.959(2) \times 10^{-11} \frac{1}{\text{Hz}}$$

have been measured. With $\alpha_{Z1,E2} = 8.387(1)$ kHz/ μ T from equation (2.31), one finds the values

$$\alpha_{Z2,E2} = 52.14(3) \frac{\text{mHz}}{\mu\text{T}^2},$$

$$\alpha_{Z2,E3} = -2.082(2) \frac{\text{mHz}}{\mu\text{T}^2},$$

that show agreement with published data for the E2 transition [73, 91] and improve the uncertainty of the value by a factor of five for the E3 transition [91].

The applied magnetic field $\mathbf{B} = \mathbf{B}_0 + \mathbf{B}_1$ is composed of \mathbf{B}_0 that compensates residual external fields, and the term $\mathbf{B}_1 = \mathbf{J}\mathbf{I}$ generating a field along a defined direction, where \mathbf{I} contains three components I_n for the currents through the three pairs of coils. The element J_{mn} of the Jacobian matrix \mathbf{J} describes the effect of coil current I_n on the magnetic field component B_m . Measuring the Zeeman frequency splitting for different orientations of the quantization axis permits determination of \mathbf{J} and thereby calibration of the magnetic field [85]. The orthogonality of an arbitrary set of magnetic field orientations can be assessed from tensorial (i.e. orientation dependent) frequency shifts. As described in section 2.3.8, measurements of the electric quadrupole shift yield an uncertainty in the orthogonality below 0.1°.

Furthermore, the agreement between the magnetic field coordinate axes and the laboratory frame as defined in section 2.1, with the z axis corresponding to the axial trap direction, is verified from measurements of the electric quadrupole shift along different magnetic field orientations. The magnetic field orientation in the laboratory frame has an uncertainty of about 1°.

Magnetic field strength and orthogonality are constantly monitored during clock operation by measuring the Zeeman splitting frequency along three orthogonal directions of the magnetic field, as shown in figure 2.15. The uncertainty for a first-order Zeeman shift of 60 kHz on the E2 transition with $\Delta m = 2$ is estimated to 100 Hz from the measurement in figure 2.15. The corresponding second-order Zeeman shift of the clock transitions is

$$\frac{\Delta\nu_{Z(\text{dc}), E2}}{\nu_{E2}} = 969(7) \times 10^{-18},$$

$$\frac{\Delta\nu_{Z(\text{dc}), E3}}{\nu_{E3}} = -41.5(3) \times 10^{-18}.$$



Figure 2.15: **Visualization of clock operation using Grafana.** The Base graph shows the frequency offset in Hz for the E2 clock transition (with $\Delta m = 0$) along three orthogonal magnetic field directions in green, orange and blue, with the respective excitation probabilities Base ExProb on the right side. The Zeeman and Zeeman ExProb graphs show the frequency (in kHz) and excitation probability for the $m_F = 0 \rightarrow m_F = 2$ magnetic sublevels of the E2 clock transition, along the same three directions as for Base. Thus, in total six servos are running during operation of the E2 transition clock.

2.3.7 Second-order ac Zeeman shift

The radio frequency voltage of the trap drive can induce alternating currents in the trap mount that lead to an ac magnetic field at the ion position, resulting in a frequency shift. In the case of the Yb^+ clock transitions [92], the shift possesses both scalar and tensor contributions and the tensor term has an angular dependence of the form $3 \cos^2 \theta - 1$ with θ the angle between the ion quantization axis and the ac magnetic field direction, similar to the angular dependence of the quadratic Stark shift. Furthermore, there is an orientation dependence not canceled by averaging over three orthogonal orientations of the quantization axis. For the $^{171}\text{Yb}^+$ E2 and E3 transitions, the sensitivities $33.8 \text{ mHz}/\mu\text{T}^2$ and $2.28 \text{ mHz}/\mu\text{T}^2$ have been determined [92] for the dependence on the quadratic ac magnetic field $\langle B^2 \rangle$ averaged over time and three orientations of the quantization axis.

There are several methods to assess the strength of ac magnetic fields in the rf trap. One straightforward approach is given by changing the trap drive voltage that has a quadratic dependence on the shift: $\Delta\nu_{Z(\text{ac})} \propto \langle B^2 \rangle \propto V^2$.

Using equation (1.6), the trap voltage can be related to the secular sideband frequencies. Different trap drive voltages lead to a large change in the dc electric fields for Yb3, discussed in section 2.3.5. This requires a change of the compensation voltages by several tens of volts, and thereby an accurate assessment of the ac Zeeman shift can not be performed currently. For a preliminary assessment of the shift, the optclock setup is used that employs the same trap configuration. The experiment is performed at two different trapping potentials, with a radial secular frequency of about 500 kHz for the low and about 2 MHz for the high trap potential. Comparing the E2 transition frequencies of optclock and Yb3, a frequency difference of 9(27) mHz has been obtained for low and high trap depth in optclock, compatible with zero and limited by the statistical uncertainty. For typical trap operating conditions of $\omega_x \approx 750$ kHz, the shift uncertainty for the E2 transition is 11 mHz and for the E3 transition 0.8 mHz. Since the E3 transition frequency is not averaged over three orientations but only probed along one direction, an upper bound of 2.4 mHz for the shift uncertainty is inferred and relative uncertainties of

$$\frac{u_{Z(\text{ac}), \text{E2}}}{\nu_{\text{E2}}} = 16 \times 10^{-18},$$

$$\frac{u_{Z(\text{ac}), \text{E3}}}{\nu_{\text{E3}}} = 1.3 \times 10^{-18}.$$

are found. These results can be used as preliminary contributions to the systematic uncertainty of Yb3, but a more rigorous treatment will follow once the physics package has been replaced in order to eliminate the effect of varying dc electric fields.

The ac magnetic field components can also be measured directly [92]. By matching the Zeeman splitting frequency of the $^{171}\text{Yb}^+ \ ^2\text{S}_{1/2}$ ($F = 1$) state to the rf drive frequency, the $|F = 1, m_F = 0\rangle$ and $|F = 1, m_F = -1\rangle$ levels are coupled by a coupling strength Ω and can be described by dressed states. From the frequency of the resulting Autler-Townes splitting [93, 94], Ω can be inferred. For a linearly polarized ac magnetic field, the coupling strength is related to the magnetic field component orthogonal to the quantization axis via

$$\Omega = \frac{g_F \mu_B B_{\perp}}{\hbar \sqrt{2}}. \quad (2.34)$$

This experiment requires driving the microwave transition on the hyperfine sublevels. Regarding the Yb⁺ clocks at PTB, microwave precision spectroscopy has been performed for the ${}^2F_{7/2} |F = 3\rangle \rightarrow |F = 4\rangle$ transition as explained in section 3.6, thus it seems feasible to conduct direct measurements of the ac magnetic field in the near future.

2.3.8 Electric quadrupole shift

Even if the ion is well centered within the trap and dc electric fields are close to zero, there might be a considerable electric field gradient A coupling to the electric quadrupole moment Θ of the excited clock states and leading to an electric quadrupole shift (EQS). The ${}^2S_{1/2}$ ground state is spherically symmetric and does not possess an electric quadrupole moment. The EQS is discussed in detail in [65] for the Yb3 system. The shift is of the form

$$\Delta\nu_{\text{EQS}} = \frac{\alpha_k}{h} A\Theta[(3 \cos^2 \theta_1 - 1) - \epsilon \sin^2 \theta_1 (\cos^2 \theta_2 - \sin^2 \theta_2)]. \quad (2.35)$$

The angles θ_1 and θ_2 define the relation between magnetic field orientation and direction of the electric field gradient. An external electric field gradient can be generated by applying a dc voltage to the endcap trap electrodes:

$$A = \frac{U}{\kappa}. \quad (2.36)$$

The voltage U , the geometric factor κ and the deviation from cylindrical symmetry ϵ are defined according to equation (1.4). For such a field gradient, $\theta_1 = \angle(\mathbf{e}_z, \mathbf{B})$ with \mathbf{e}_z the unit vector of the trap symmetry axis. Furthermore, α_k contains the coupling terms of the Hamiltonian for transition k , with $\alpha_{E2} = 1$ and $\alpha_{E3} = 5/7$. Combining the prefactors, one finds the angle-independent frequency shift $\nu_{\text{quad}} = \alpha_k A\Theta/h$.

Equation (2.35) averages to zero for three orthogonal orientations of the magnetic field [82]. This can be used for a test of the orthogonality of the magnetic field directions. With the independent clock Yb1 serving as a stable frequency reference, a comparison of the frequency shift between small ($U = 0$ V) and large ($U = -60$ V) externally applied electric field gradient A is performed on the E2 clock transition of Yb3. After averaging over the

three orthogonal directions, a transition frequency difference of 0.02(4) Hz is found, with a shift $\nu_{\text{quad}} \approx 78$ Hz for the large field gradient. This yields an EQS suppression of about 2000 and verifies the orthogonality of the employed magnetic field directions for Yb3, with an uncertainty in the angle between two directions below 0.1° . Furthermore, the absolute orientation of the magnetic field vector with respect to the laboratory frame is deduced from the frequency shifts along the different directions, with an uncertainty of about 1° .

For a measurement of the electric quadrupole moment using an externally applied electric field gradient, the geometric factor κ needs to be assessed with high accuracy. Together with ϵ , it can be extracted from measurements of the secular sidebands ω_i according to equation (1.6) by varying the voltage U applied to the trap endcap electrodes. As shown in figure 2.16 for ω_x , the voltage is changed from -60 V to 30 V. From a fit to the general expression of equation (1.6) found in [46], the values

$$\begin{aligned}\kappa &= -1.0417(8)\text{mm}^2, \\ \epsilon &= 0.036(1)\end{aligned}$$

are determined. At $U = -60$ V, this yields $\nu_{\text{quad}} = 78.7(2)$ Hz for the E2 transition. Next, the electric quadrupole moments of the excited clock states $^2\text{D}_{3/2}$ and $^2\text{F}_{7/2}$ are assessed. Both clock transitions are measured with interleaved clock operation at the large externally applied field gradient, as shown in figure 2.17. The E3 transition of Yb1 provides a stable frequency reference. The measurement, running for more than four hours, has been compared to preceding long-term measurements of the unshifted frequency. The magnetic field orientation yields $\theta_1 = 1(1)^\circ$ and the second term in equation (2.35) becomes negligible. With $U = -60.0(3)$ V and $A = 57.6(3)$ V/mm², the following shifts and quadrupole moments are found:

$$\begin{aligned}\Delta\nu_{\text{E2}} &= 152.0(2) \text{ Hz} \longrightarrow \Theta(^2\text{D}_{3/2}) = 1.95(1) ea_0^2, \\ \Delta\nu_{\text{E3}} &= -1.65(3) \text{ Hz} \longrightarrow \Theta(^2\text{F}_{7/2}) = -0.0297(5) ea_0^2,\end{aligned}$$

with e the elementary charge and a_0 the Bohr radius. The uncertainty is reduced by about one order of magnitude in each case compared to previous

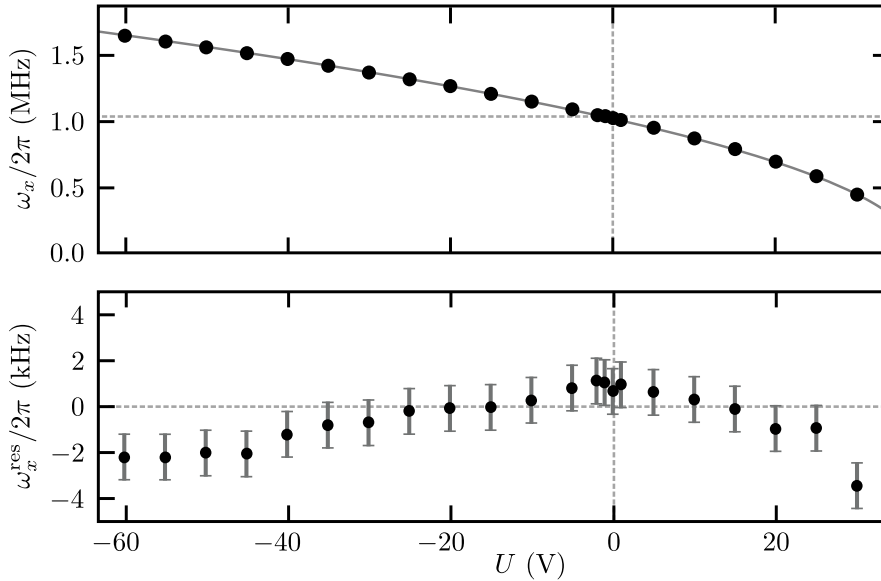


Figure 2.16: **Secular sideband frequency ω_x in dependence of the dc voltage U** applied on both endcap electrodes to de- or increase the trap potential along x . Residuals are given in the lower graph. An increasing deviation from the expected sideband frequency for an increasing absolute value of U is found. This might be related to the fluctuating dc electric fields already discussed, which change for an additionally applied dc voltage U and lead to a displacement of the ion from the potential minimum. The deviations are accounted for in the uncertainty assessment.

measurements. For $\Theta(^2D_{3/2})$, a 1σ agreement is found with the published experimental value [95] and theoretical predictions are within 10 % [82, 96–99]. The $\Theta(^2F_{7/2})$ value yields a 2σ agreement with previous experimental data [75], but theoretical predictions differ by more than a factor of two [97–100] due to the complex electronic structure of the excited clock state that poses a challenge for precise calculations. The ratio of the two quadrupole moments, independent of the specific magnitude and orientation of the electric field gradient, is given by $\Theta(^2D_{3/2})/\Theta(^2F_{7/2}) = -65.8(1.2)$. The corresponding frequency shift ratio $\Delta\nu_{E2}/\Delta\nu_{E3} = -92.1(1.7)$ is employed to assess the EQS on the E3 transition, as will be discussed in the following. During clock operation, the electric quadrupole shift on the E2 transition is suppressed using the method of three orthogonal magnetic field orientations as shown in figure 2.15. There, a total of six independent servos, for each of the three directions and for both the $\Delta m = 0$ (top) and the $\Delta m = 2$ (bottom) transition, are used to assess electric quadrupole and second-order Zeeman shift. For the E3 transition, however,

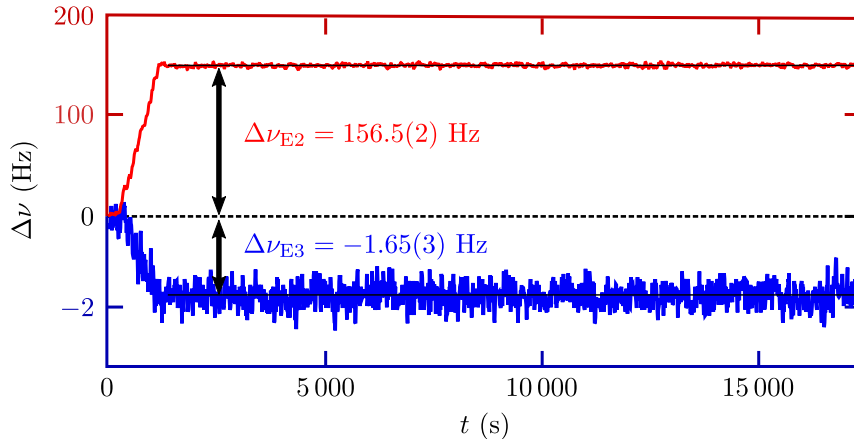


Figure 2.17: **Frequency shift due to an external electric field gradient** measured in interleaved clock operation on both the E2 and E3 transition. The field gradient is generated using an additional dc voltage U applied to the endcap electrodes. At $t = 0$ s, $U = 0$ V and then it is slowly ramped up to $U = -60$ V. The unperturbed transition frequency is determined from independent measurements. The figure is adapted from [65].

the measurement with different magnetic field orientation comes along with large variations of the likewise orientation-dependent light shift, resulting in degradation of clock performance. Instead, the EQS ratio is used to infer the shift on the E3 transition from the E2 transition shift along a single direction. For the estimate of the E2 transition frequency uncertainty, probing along the direction with maximum sensitivity to an error in the angle ($\theta_1 = 45^\circ$) is assumed, with an uncertainty in the angle of 0.1° . For the E3 transition, the uncertainty of the same estimate is added in quadrature to the uncertainty resulting from the quadrupole moment ratio. With patch charges inducing electric field gradients of about 1 V/mm^2 in the trap center, resulting in shifts on the order of 1 Hz on the quadrupole transition, the typical contribution to the systematic uncertainty yields

$$\frac{\Delta\nu_{\text{EQS, E2}}}{\nu_{\text{E2}}} = 0(10) \times 10^{-18},$$

$$\frac{\Delta\nu_{\text{EQS, E3}}}{\nu_{\text{E3}}} = -4.5(1) \times 10^{-18}.$$

In section 4.1, another method for the suppression of the EQS is discussed, relying on the rotation of the magnetic field direction during the dark time of a Ramsey sequence. This is particularly beneficial for clock operation on

the E3 transition as the shift is suppressed within a single interrogation cycle, independently of the magnetic field orientation set during the clock pulses.

2.3.9 Background gas collisions

Collisions with background gas atoms and molecules may cause shifts of the clock transition energy levels. Furthermore these collisions may lead to heating of the ion, resulting in an additional contribution to the second-order Doppler shift. For Langevin collisions, for which a particle is spiraling in towards the ion, additionally a change of the atomic phase can occur which may perturb the superposition of ground and excited clock state. An estimate of the frequency shift has been inferred from [101] for Yb1 [42] using the scattering rate $\gamma = n \langle v \rangle \sigma$ with the number density $n = p/k_B T$, the mean speed of the background gas particles $\langle v \rangle$ and the collision cross section σ . With a pressure of 1×10^{-8} Pa, a collision rate of $3 \times 10^{-3}/s$ and shift of 0.4 mHz is deduced for He as the main background gas constituent. This yields a fractional uncertainty of 6×10^{-19} for both the E2 and E3 transition.

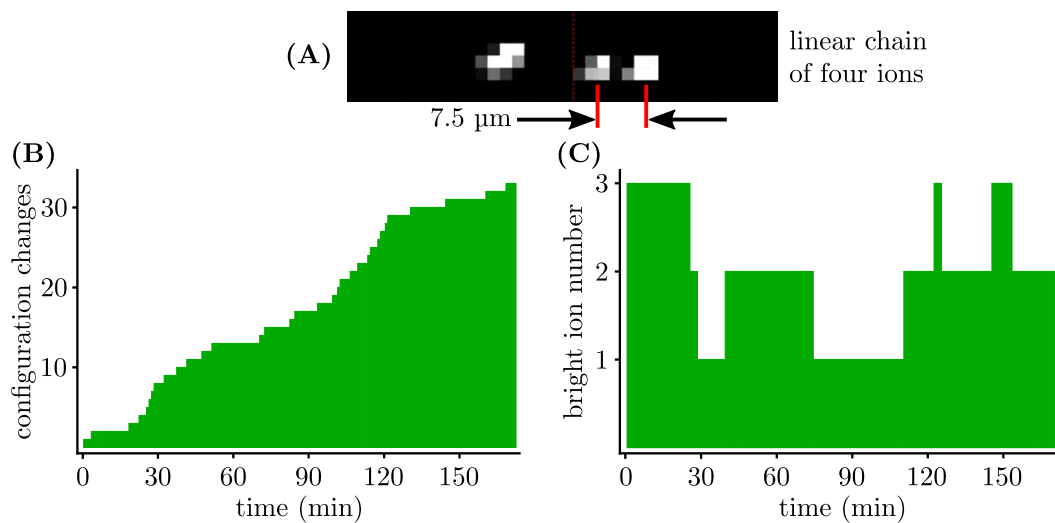


Figure 2.18: **Background gas collisions in an ion crystal.** (A) Linear chain of four ions in the Yb3 trap, with the second ion dark. (B) Changes of the configuration within the linear ion chain. (C) Changes in the number of fluorescing ions within the linear chain.

For Yb3, the pressure is estimated from the ion pump reading to be below 5×10^{-9} Pa, resulting in a fractional uncertainty of the clock transitions below

3×10^{-19} . A lower pressure for Yb3 in comparison to Yb1 is also confirmed by measurements of the reordering rate in an ion crystal: After loading four ions in a linear chain (with one constantly dark), changes of the configurations are observed and accounted to collisions with background gas particles. Recording the changes for about three hours as shown in figure 2.18 (B) yields a rate of $8 \times 10^{-4}/\text{s}$ for position changing collisions for one ion. For a reordering event to occur, the energy for a change of the crystal configuration needs to be lower than the energy transferred to one of the ions due to the collision, $E_{\text{reorder}} < E_{\text{ion}}$. For a two-ion crystal, the energy difference between the ions aligned along the minimum trapping potential (i.e. the axial direction) and along the orthogonal orientation (i.e. the radial direction) serves as an estimate for E_{reorder} [102]: For the employed trapping conditions, $E_{\text{reorder}}/k_{\text{B}} \approx 5$ K for a two-ion Yb^+ crystal, with k_{B} the Boltzmann constant. The collisional energy transfer depends on the scattering angle and the background gas species. Assuming H_2 molecules as the main background gas constituent with a mean speed of about 1.8 km/s at room temperature, a maximum energy transfer to an Yb^+ ion of $E_{\text{ion}}^{\text{max}}/k_{\text{B}} \approx 9$ K is approximated.

Simultaneously to the reordering measurement, the population of the $^2\text{F}_{7/2}$ state has been analyzed as shown in figure 2.18 (C): By turning off the 760 nm repump laser, the population of the F-state can be observed by loss of fluorescence on an individual ion. The transitions into and out of the closed cooling cycles are accounted to collisions with background gas particles. A rate of roughly one quenching collision per hour per ion has been deduced from the measurement, corresponding to a rate of $2 \times 10^{-4}/\text{s}$. Both rates for position changes and F-state quenching have been confirmed in a separate measurement employing a five-ion-crystal.

Using an elaborate model including a Monte-Carlo method to take into account different types of collisions, the background gas collision shift has been calculated for the $^{27}\text{Al}^+$ clock at NIST [102]. There, also a rough estimate for the $^{171}\text{Yb}^+$ E3 transition is given with a shift of $0.0(2.5) \times 10^{-19}$ at a pressure of 6×10^{-9} Pa.

Combining the information obtained from measurements and calculation,

the shift due to background gas collisions is estimated to

$$\frac{\Delta\nu_{\text{BGC, E2}}}{\nu_{\text{E2}}} = \frac{\Delta\nu_{\text{BGC, E3}}}{\nu_{\text{E3}}} = 0(3) \times 10^{-19}.$$

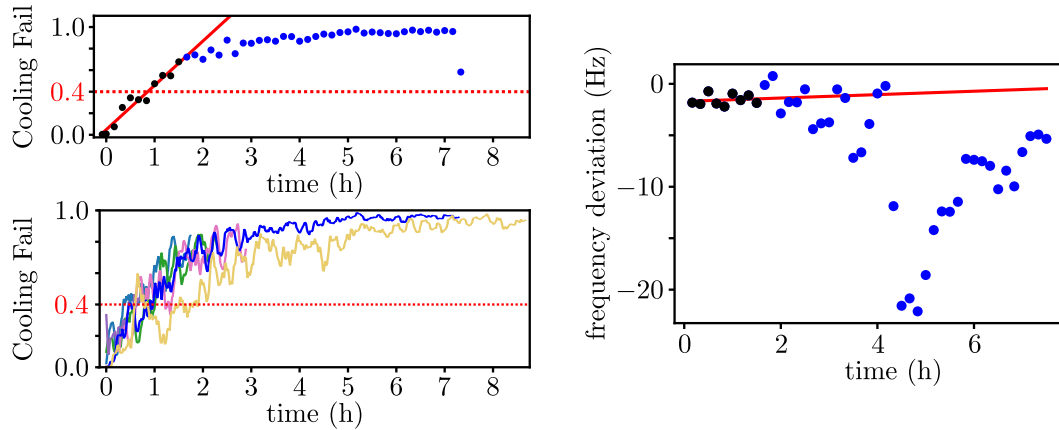


Figure 2.19: **Frequency shift due to background gas collisions** after ion pump shutdown at time $t = 0$ h. From the number of failed cooling cycles (Cooling Fail), the relative increase in the background gas pressure can be inferred that is linear during the initial increase (upper left graph). After about one hour, the number of Cooling Fail events reaches more than 40 % that degrade clock performance significantly. The lower left graph shows that the behavior is similar for several repetitions of the pump shutdown experiment. From approximately the first hour after shutdown, the frequency change on the clock transition can be analyzed, shown here on the right side for one measurement on the E2 transition: The black points are used to extract a slope (red line) of 165 mHz/hour.

A few remarks should be added:

- (1) The theoretical calculations [101] assume Rabi excitations, but similar results are expected for Ramsey and hyper-Ramsey spectroscopy.
- (2) During clock operation, only valid cycles are taken into account. A cycle is not valid, if there is no fluorescence during the cooling period directly after the clock pulse, for example due to a high ion temperature resulting from a collision. The control system continues to iterate cooling cycles until fluorescence is detected again. These cooling attempts are denoted as a Cooling Fail event in the records. Thus, part of the possible shift due to collisions is mitigated by a control mechanism of the clock sequence.
- (3) First tests of a fully experimental assessment of the shift have been performed as shown in figure 2.19. Switching off the ion pump, the increase

in collisions and thereby the pressure can be monitored as the number of Cooling Fail events. The pump restarts automatically if there are enough particles to initiate the pumping. One hour after pump shutdown, about 40 % of the cooling attempts fail and clock performance becomes largely degraded. There the pressure is 100 times larger than during normal clock operation, where about 0.4 % of clock cycles are invalid due to a Cooling Fail event. When operating the clock during the pressure increase, changes in the transition frequency would indicate a shift effect. Six measurements have been performed on the E2 transition. A stability on the order of $10^{-14}/\sqrt{\tau}$ for each measurement is found. From the mean slope of all measurements, a shift of 120(480) mHz at a pressure 100 times larger than the base pressure has been deduced. This leads to a fractional shift of $2(7) \times 10^{-18}$ for the E2 transition, with the accuracy limited by the statistical uncertainty. These experiments need to be further pursued to reduce the shift to the level obtained from theoretical considerations.

2.3.10 Gravitational redshift

For the comparison of two clocks, a frequency correction of the form [103]

$$\frac{\Delta\nu_{\text{GR}}}{\nu_0} = \frac{\phi_1 - \phi_2}{c^2} \quad (2.37)$$

needs to be taken into account for one of the clocks, with $\phi_{1,2}$ the gravitational potential at the position of clock 1 and 2, respectively. This prediction of a time dilation known as gravitational redshift was first stated by Einstein [104]. It is incorporated in Einstein's theory of general relativity and has been verified at the 10^{-5} level by precise measurements of the gravitational redshift, performed both with optical atomic clocks at different heights on Earth [13] and with atomic clocks on Galileo satellites in eccentric orbits [105, 106]. Alternatively, under the assumption that general relativity holds true, the gravitational redshift provides the possibility of using atomic clocks for precise geodetic measurements [107].

On the Earth's surface and for short distances, the correction can be ex-

pressed by

$$\frac{\Delta\nu_{\text{GR}}}{\nu_0} = \frac{g\Delta h}{c^2}, \quad (2.38)$$

with g the acceleration due to gravity and Δh the height difference of the clocks. A value of $g = 9.81251(1) \text{ m/s}^2$ has been obtained for the clock hall from measurements performed at PTB in 2018 with a gravity meter [108]. The uncertainty of g results from its extrapolation from the point of measurement on the PTB campus to the position of the atomic clocks in the clock hall.

Three reference points⁹ for the normal heights within the German national leveling network DHHN92 (Deutsches Haupthöhennetz 1992) in the clock hall of PTB [109, 110] are used to calibrate the height of a line laser for leveling to an uncertainty of about 2 mm. With the line laser, the differential heights of the experimental setups are measured. For example, a height difference of

$$h_{\text{Yb1}} - h_{\text{Yb3}} = -0.065(3) \text{ m}$$

is deduced between the Yb1 and Yb3 clock, which yields a gravitational redshift of Yb3 with respect to Yb1 of

$$\frac{\Delta\nu_{\text{GR}}}{\nu_0} = 7.1(3) \times 10^{-18}.$$

2.3.11 Probe shifts

The atom-light interaction as well as the frequency changing elements, such as acousto-optic modulators (AOMs), can produce frequency shifts. These effects have been studied in detail with the Yb1 setup [36, 42, 111] and the results, summarized in the following, can be transferred to the Yb3 setup.

Light shift. Excitation of a transition is accompanied by electromagnetic radiation leading to an ac Stark shift as described in section 2.3.1, which is called light shift (LS). Especially for the E3 transition with the small oscillator strength, high intensities of MW/m^2 are needed to drive the transition as stated in section 1.4.4. Consequently, the frequency is shifted by $\sim 100 \text{ Hz}$ on a transition that is determined with an accuracy of a few mHz. Using interrogation schemes featuring nested servo loops, such as Rabi-controlled hyper-

⁹The floor marker KB03 and the reference points of CSFI and CSFII, KB05 and KB06, have been used [109, 110].

Ramsey [62, 63] or autobalanced Ramsey spectroscopy [66], the light shift can be measured and corrected in real time during clock operation. For Yb3 that features the Rabi-controlled hyper-Ramsey scheme also used in Yb1 [36], an uncertainty of

$$\frac{u_{\text{LS, E3}}}{\nu_{\text{E3}}} = 8 \times 10^{-19}$$

is deduced. It is based on the estimated uncertainty in the equality of Ramsey and Rabi pulses. As an example, the different pulse lengths could lead to different thermal expansion of the crystal of the AOM driving the pulses. Furthermore, the servo response time of several tens of seconds can lead to light shift errors in case of pointing fluctuations.

The shift contribution can be easily reduced if needed: For long interrogation times (i.e. long Ramsey dark times), the pulses can be extended without a large impact on the overall duty cycle. The intensity scales inverse quadratically with the pulse time and the light shift reduces accordingly. As an example, extending the π -pulse time of currently 60 ms to 120 ms would reduce the shift uncertainty by about a factor of four.

For the quadrupole transition that is driven with about seven orders of magnitude smaller intensity (see section 1.4.4), the light shift for a 30 ms Rabi pulse is [95]

$$\frac{\Delta\nu_{\text{LS, E2}}}{\nu_{\text{E2}}} = -4(4) \times 10^{-19}$$

which is negligible at the current uncertainty level and does not require more involved excitation schemes.

AOM chirp. Typically, acousto-optic modulators are employed in the beam paths to provide frequency offsets and changes of the laser intensity at the ion position. As discussed in detail in [42], switching the power of the AOM leads to a frequency chirp due to temperature changes in the AOM crystal: Switching from maximum to zero rf power results in a relative frequency shift of -8×10^{-16} . The shift is expected to scale linearly with the applied rf power and is typically suppressed by driving the AOM at low power. For the E2 transition, an attenuation of at least 20 dB with respect to the maximum driving power is applied, leading to an uncertainty contribution of

$$\frac{u_{\text{chirp, E2}}}{\nu_{\text{E2}}} = 8 \times 10^{-18}.$$

For the hyper-Ramsey sequence of the E3 transition, a careful analysis of the phase evolution of the probe light has been performed in [111]. It has been found that phase deviations during the pulses lead to an effective frequency detuning of 2 mHz, corrected by the second servo employing the Rabi pulse. Furthermore, periodic variations of the laboratory temperature cause phase drifts due to thermal instabilities of the optical setup, that are expected to average out for sufficiently long measurement times. For an averaging time of one day, a relative frequency shift of 1×10^{-18} is found. This is taken as an estimate for the uncertainty contribution to the E3 transition frequency:

$$\frac{u_{\text{chirp, E3}}}{\nu_{\text{E3}}} = 1 \times 10^{-18}.$$

For longer measurement intervals, the uncertainty becomes smaller. As the rf drive power is proportional to the intensity at the ion position, the shift can be further reduced by extending the pulse time and lowering the AOM input power as explained in the context of the light shift uncertainty above.

As another approach, AOM chirps can be largely suppressed by stabilizing the probe light to the light of a reference fiber after passing through the trap. Thereby, any type of phase excursion, also related for example to air turbulences during free space propagation of the light, can be eliminated. This idea is discussed in greater detail in section 2.4.2.

Servo error. Drifts of the cavity stabilizing the probe laser light can result in servo errors [112], since the transition is not interrogated continuously. Both clock lasers are stabilized to a cryogenically cooled single-crystal silicon cavity [58] with a typical drift rate below 1 mHz/s and a drift rate change of less than 0.1 mHz/s², which is an order of magnitude better compared to the ULE cavities used before [42]. A second-order integrator implemented directly in the clock AOM synthesizer cancels the linear drift and for measurements of several thousands of seconds, the nonlinear frequency drift and the resulting uncertainty become small contributions to the total uncertainty:

$$\begin{aligned} \frac{u_{\text{servo, E2}}}{\nu_{\text{E2}}} &= 3 \times 10^{-19}, \\ \frac{u_{\text{servo, E3}}}{\nu_{\text{E3}}} &= 1 \times 10^{-19}. \end{aligned}$$

Frequency resolution. The AOMs shaping the clock laser light are driven by synthesizers realizing the frequency using direct digital synthesis (DDS). The memory size determines the frequency resolution and thereby the offsets from the target frequency. The synthesizers used have a 48 bit resolution of the frequency tuning word and are referenced to 100 MHz, which corresponds to a frequency resolution of 0.4 μHz , resulting in negligible errors:

$$\frac{\Delta\nu_{\text{freq. res., E2}}}{\nu_{\text{E2}}} < \frac{\Delta\nu_{\text{freq. res., E3}}}{\nu_{\text{E3}}} < 10^{-21}.$$

2.3.12 Uncertainty budget

Summarizing the frequency shifts discussed, the uncertainty budgets for the two clock transitions of Yb3 are derived in table 2.2. Since variations of the dc electric fields as discussed in section 2.3.5 may lead to a first-order Doppler shift at the 10^{-17} fractional frequency level, the uncertainty budget is considered preliminary. These variations are expected to be eliminated by exchanging the physics package.

Second-order Zeeman and quadrupole shift are assessed in real time during clock operation. Given in table 2.2 are typical shift values. A gravitational redshift has to be taken into account in frequency measurements, unless the two clock transitions of Yb3 are compared directly.

Shift effect	$\Delta\nu/\nu_{\text{E2}}$	u/ν_{E2}	$\Delta\nu/\nu_{\text{E3}}$	u/ν_{E3}
Blackbody radiation	-517	18	-73.6	1.5
Ion motion	-1.5	0.4	-1.0	0.2
2nd-order Zeeman (dc)	969	7	-41.5	0.3
2nd-order Zeeman (ac)	0	16	0	1.3
Electric quadrupole	0	10	-4.5	0.1
Background gas collisions	0	1	0	0.3
Light shift	-0.4	0.4	0	0.8
AOM chirp	0	8	0	1.0
Servo error	0	0.3	0	0.1
Total	450	28	-120.6	2.4

Table 2.2: **Yb3 uncertainty budget** for both the E2 and E3 transition in fractional frequency units divided by 10^{-18} .

2.4 Evaluation of the frequency instability

For an atomic clock employing a Ramsey-type experiment with short $\pi/2$ pulses and short dead time in between successive clock interrogations compared to the Ramsey dark time T_{dark} , as well as unity state detection efficiency and negligible spontaneous decay rates, the clock instability can be described by the Allan deviation expressed by [10]

$$\sigma_y(\tau) = \frac{1}{2\pi\nu_0\sqrt{NT_{\text{dark}}\tau}}, \quad (2.39)$$

where N is the number of interrogated atoms. The formula shows that high-frequency transitions, a large number of atoms and long Ramsey dark times improve the stability. For the Yb^+ single-ion clock, $N = 1$ and ν_0 is given. Therefore, the main focus is put on extending T_{dark} in order to improve the stability. From a simple model relating the expectation value of the Ramsey experiment with the local oscillator phase noise [55], a formula for the Ramsey fringe contrast, the excitation probability P in dependence of T_{dark} , can be extracted:

$$P = \frac{1}{2}A \left(1 + e^{-(\sigma_{\text{FF}}\omega_L T_{\text{dark}})^2/2} \cos[(\omega_L - \omega_0)T_{\text{dark}} + \phi] \right), \quad (2.40)$$

with A the maximum contrast amplitude, $\omega_L/(2\pi)$ the laser and $\omega_0/(2\pi)$ the atom transition frequencies, and ϕ the phase difference between the two Ramsey pulses. The flicker frequency noise σ_{FF} represents the instability of the local oscillator at the ion position. From a deliberate detuning $\delta = \omega_L - \omega_0$ and a variation of T_{dark} , the noise σ_{FF} is deduced. Furthermore, an optimum probe time can be estimated:

$$T_{\text{dark}}^{\text{opt}} = \frac{1}{\sqrt{2}\sigma_{\text{FF}}\omega_0}. \quad (2.41)$$

2.4.1 Comparison of Yb1 and Yb3

With the E3 transition clock laser only stabilized to its ULE cavity that has a short term stability of about 5×10^{-16} , Ramsey dark times for Yb1 with contrast of more than 80 % are limited to about 150 ms. In an extended setup explained in section 3.1, the signal of a laser stabilized to a single-

crystal silicon cavity with an instability of 5×10^{-17} from 1 s to more than 10 s [58] is transferred via a frequency comb to the E3 clock laser. Assuming full transfer of this tenfold better frequency instability to the local oscillator at the ion position, it is expected to obtain coherent interrogation of at least 1 s according to equation (2.40). However, the extended setup only enables T_{dark} of up to 300 ms, corresponding to an improvement of the coherence time of about a factor of two and implying a limitation in the stability transfer. For Yb3, similar coherence times are observed, thus the properties of the physics package such as ion heating rate or vacuum quality seem not to be the limiting factor. To investigate the instability of the clocks in more detail, three different experiments are conducted and explained in the following.

1. Detuning scans with 1 s and 2 s Rabi pulses are performed for Yb3 while the clock laser is stabilized by Yb1. As can be seen in figure 2.20, the linewidths of both resonance lines do not reach the Fourier limit of 0.8 Hz and 0.4 Hz, respectively, indicating noise sources resulting in decoherence. One such source is the quantum projection noise of Yb1 which serves as the frequency reference. Using a reference with better short-term stability, such as the Sr lattice clock at PTB, this contribution would become negligible.

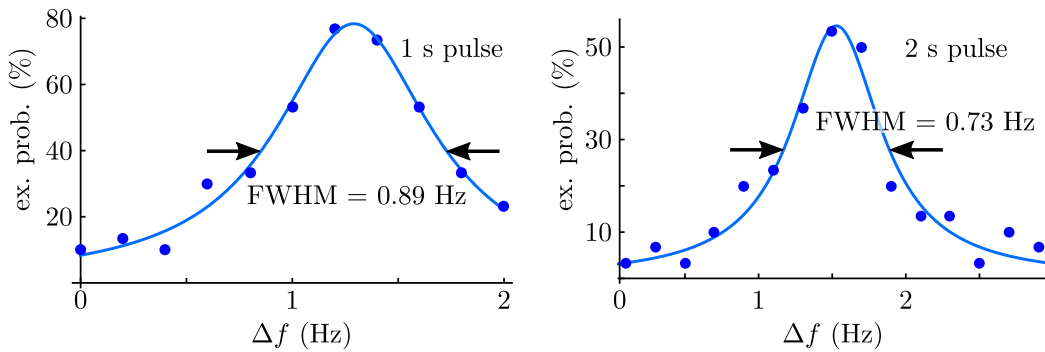


Figure 2.20: **E3 transition profiles of a detuning scan** using Rabi pulses of 1 s and 2 s length. The full width at half maximum (FWHM) is in both cases larger than the Fourier limits of 0.8 Hz and 0.4 Hz.

2. Clock operation on the E3 transition in Yb3 is performed with two identical, interleaved servos that are operated digitally: The first servo is stabilizing the clock laser to the atomic transition, the second servo is controlling an offset to the first. If the transition frequencies obtained with both servos are identical, this offset averages to zero. The frequency data of the second

servo is used to investigate the stability as shown in figure 2.21. For two independent measurement runs with 500 ms (blue) and 1000 ms (green) Rabi pulses, similar instabilities are found, marked by the black dashed line:

$$\sigma_y^{\text{two-servo}}(\tau) \approx 1.4 \times 10^{-15} / \sqrt{\tau/\text{s}}.$$

The instability has been divided by $\sqrt{2}$ to indicate the level that would be obtained without the duty cycle reduction from interleaved clock operation. Since the instability does not improve for longer Rabi pulse times, a limitation of the local oscillator coherence is suspected. In a long-term comparison of Yb1 and Yb2 discussed in detail in section 3.2, with Ramsey dark times of 350 ms and 360 ms, respectively, a similar instability (red) is found. For all three measurements, two servo signals are compared with each other. Assuming equal noise contributions for both servos, $\sigma_y^{\text{two-servo}}(\tau)$ can be divided by $\sqrt{2}$ to obtain the single-servo instability:

$$\sigma_y^{\text{single-servo}}(\tau) \approx 1.0 \times 10^{-15} / \sqrt{\tau/\text{s}}.$$

Comparing Yb1 to the Sr lattice clock at PTB, which exhibits a superior frequency instability of about $1.5 \times 10^{-16} / \sqrt{\tau/\text{s}}$, confirms the single-servo instability [38].

3. The Ramsey fringe contrast for different Ramsey dark times and with a small detuning δ of the laser frequency from the atomic resonance frequency is shown in figure 2.22. Evaluation of the signal using equation (2.40) confirms the observation of similar instabilities for the local oscillators at the ion positions of Yb1 and Yb3, which are not at the level expected from the Si-cavity:

$$\begin{aligned} \sigma_{\text{FF}}(\text{Yb1}) &= 5.7(3) \times 10^{-16}, \\ \sigma_{\text{FF}}(\text{Yb3}) &= 5.9(6) \times 10^{-16}. \end{aligned}$$

The optimum probe time $T_{\text{dark}}^{\text{opt}}(\text{Yb1}) = 307(16)$ ms calculated with equation (2.41) is consistent with experimental observations.

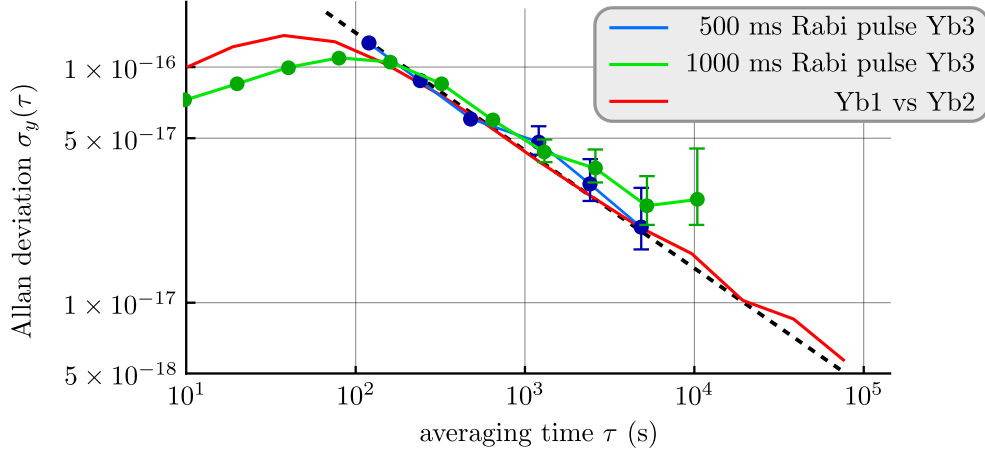


Figure 2.21: **Allan deviation of interleaved clock operation** with two servos employing Rabi pulses of equal length on the E3 transition. The first servo stabilizes the laser to the transition frequency, the second servo controls an offset with respect to the first and is analyzed in terms of the frequency instability. To incorporate the duty cycle reduction by a factor of two, the values of the data points are divided by $\sqrt{2}$. The blue graph shows the measurement for 0.5 s, the green curve for 1 s Rabi pulses. For comparison, the clock stability of Yb1 vs Yb2 discussed in section 3.2 is shown in red. The dashed line corresponds to an instability of $1.4 \times 10^{-15}/\sqrt{\tau/s}$.

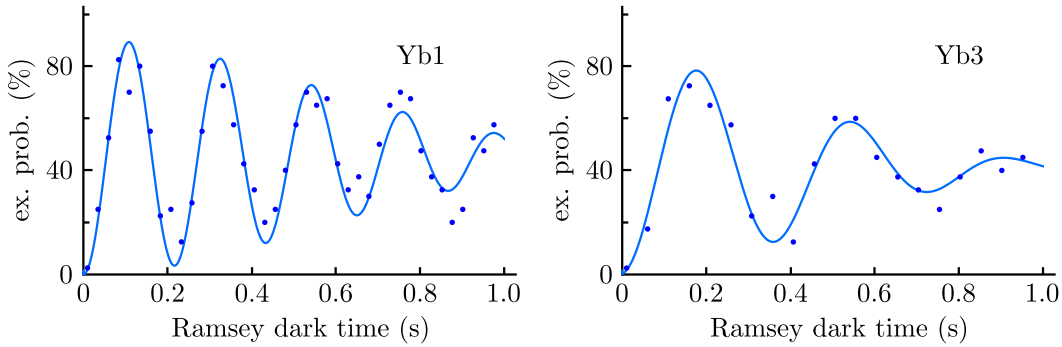


Figure 2.22: **Ramsey fringe contrast for different dark times** and with small detunings $\delta \approx 2\pi \times 5$ Hz and $\delta \approx 2\pi \times 2.5$ Hz for Yb1 and Yb3, respectively, in order to extract the local oscillator instability at the ion position.

2.4.2 Probe light stabilization with a reference fiber

One possible noise source that could limit the transfer of the Si cavity stability and lead to a disturbances of the local oscillator phase at the ion position is related to unstabilized beam paths. While the light guided through optical fibers is actively phase stabilized, most of the free space path is not: For Yb1, the unstabilized beam is propagating over a distance of about 3 m between fiber output and trap in free space. In order to suppress possible frequency and phase excursions due to air turbulence or moving optics, this part of the setup is revised. A phase stabilization is implemented directly after the ion trap to the light of a reference fiber with much shorter free space travel, as shown in figure 2.23. Thereby, the unstabilized beam path reduces from about 3 m to about 20 cm.

The stabilization depends on the probe light propagating through the trap, which also causes an interaction of the ion with the probe light. To avoid coupling to the atomic transition while the phase locked loop of the stabilization has not settled, a frequency detuning is applied in the interrogation sequence during the initialization of the phase lock as shown in figure 2.24: When introducing the probe light by opening the shutter and switching on the AOM in front of the trap, the frequency of both probe and reference beam is detuned by 1 kHz in order to be off-resonant with respect to the atomic transition. After 4 ms of settling time for the control loop, during which a phase of 8π is accumulated that does not influence the relative phase between local oscillator and atomic transition, the frequencies of probe and reference light are switched simultaneously to the light-shifted resonance frequency for the duration of the pulse.

A direct comparison of unstabilized and stabilized free-space path yields the Ramsey fringe contrasts shown in figure 2.25 (A), with flicker frequency noises

$$\begin{aligned}\sigma_{\text{FF}}(\text{Yb1, unstabilized}) &= 5.3(6) \times 10^{-16}, \\ \sigma_{\text{FF}}(\text{Yb1, stabilized}) &= 3.4(3) \times 10^{-16},\end{aligned}$$

and an optimal probe time $T_{\text{dark}}^{\text{opt}}(\text{Yb1, stabilized}) = 515(27)$ ms.

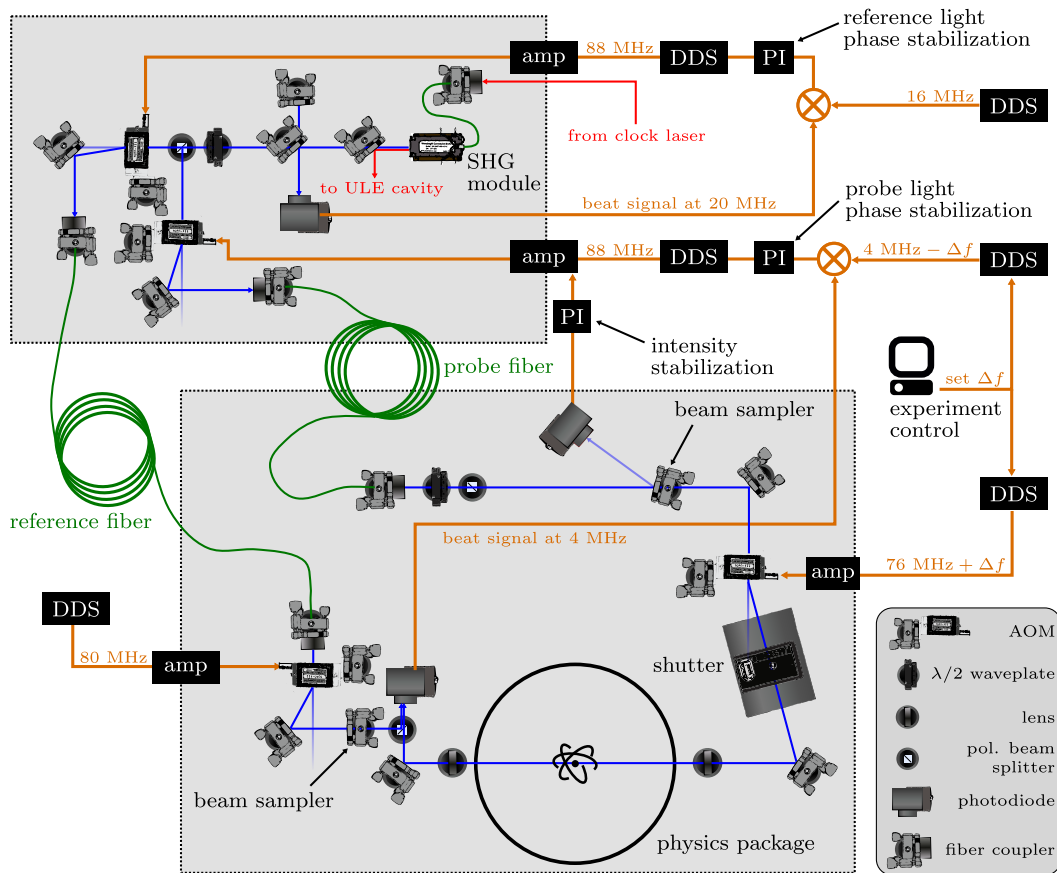


Figure 2.23: **Schematic setup of the reference fiber stabilization.** Beam paths are marked by red and blue, electronic signals by orange lines. Light from the clock laser is coupled into a second harmonic generation (SHG) module and the frequency doubled light is sent via two optical fibers (green lines) to the table with the physics package. The light leaving the probe fiber is intensity stabilized by varying the amplification (amp) of the rf signal of the AOM in front of the fiber. To interrogate the ion, the probe beam can be pulsed with an AOM and a shutter controlled by the experiment control. The light propagating through the reference fiber is phase stabilized by sending a small fraction of the light back to create a beat signal, picked up by a photodiode in front of the fiber. The beat signal between reference and probe light is measured by a photodiode and used to stabilize the complete probe beam path. The experiment control introduces frequency offsets Δf , for example to correct for the light shift, simultaneously to the DDS steering the AOM in front of the trap and the DDS controlling the beat frequency. Thereby, the integrating digital servo system (PI) of the probe light phase stabilization remains settled when offsets are applied.

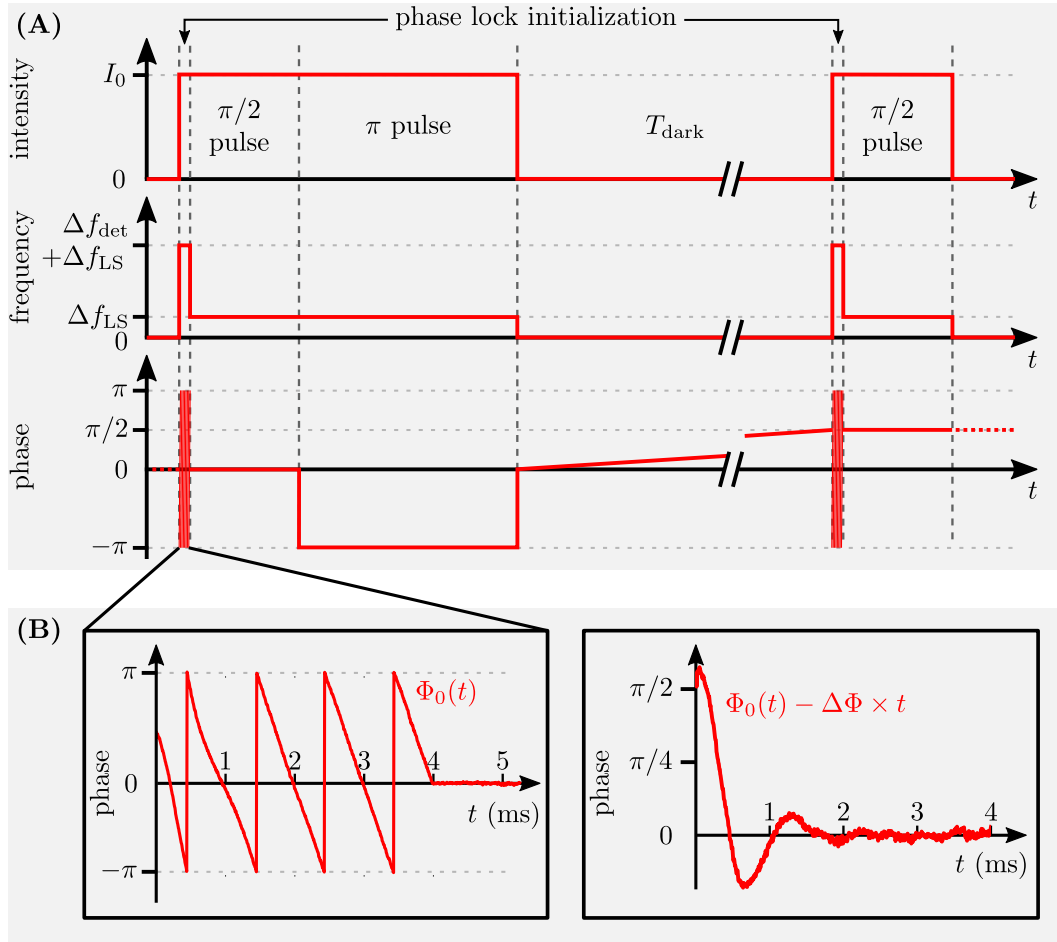


Figure 2.24: **Pulse sequence of hyper-Ramsey spectroscopy employing the reference fiber stabilization.** (A) Intensity, frequency and phase of the hyper-Ramsey spectroscopy, but with the phase lock initialization as additional elements of the sequence. There, the light is already interacting with the ion, but a frequency detuning Δf_{det} keeps the laser radiation off-resonant to the atomic transition. Detuning and initialization time span are chosen such that the phase of the local oscillator evolves by a multiple of 2π with respect to the atomic transition phase during that interval. Thereby, the detuning does not introduce an additional phase offset between the Ramsey pulses which would result in a frequency error. Shifting the frequency of the probe laser field by Δf_{LS} , the light shift is compensated. (B) Experimental data of the probe light phase with respect to the atomic transition phase. On the right hand side, the constant phase drift due to the detuning Δf_{det} has been removed to visualize the settling behavior of the control loop. It is emphasized that the probe light phase evolves by a multiple of 2π in addition to the phase correction applied by the servo system.

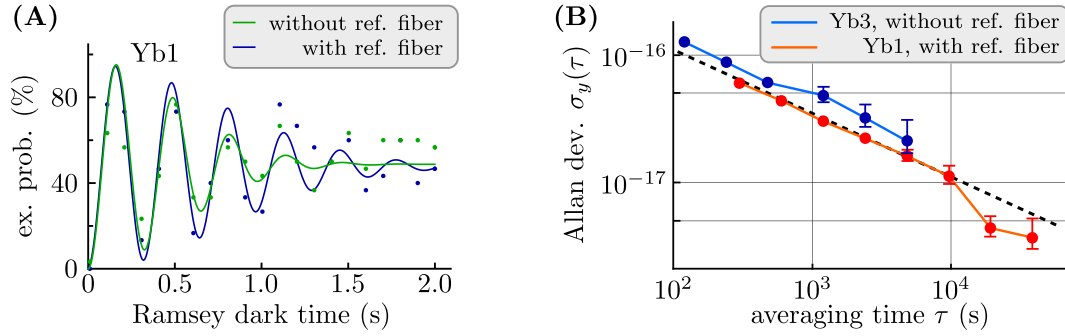


Figure 2.25: **Instabilities with and without the reference fiber.** (A) Ramsey fringe contrast for Yb1, without (green) and with (blue) stabilization of the free space beam path by the reference fiber. (B) Allan deviation of interleaved clock operation. Two servos employ 500 ms long Rabi pulses on the E3 transition. The first servo stabilizes the laser to the transition frequency, the second servo controls an offset with respect to the first and is analyzed in terms of the frequency instability. To incorporate the duty cycle reduction by a factor of two, the instabilities are divided by $\sqrt{2}$. The blue graph shows the measurement for Yb3 already presented in figure 2.21 that does not involve a reference fiber for stabilization. The red graph shows data for Yb1 employing the reference fiber stabilization scheme. The black dashed line corresponds to an instability of $1.1 \times 10^{-15} / \sqrt{\tau/s}$.

The improvement of the instability is confirmed by interleaved clock operation of Yb1 with Rabi pulses of 500 ms, identical to the measurements shown in figure 2.21 for Yb3 but with the reference fiber stabilization scheme employed. The Yb1 clock instability depicted in figure 2.25 (B) in red yields

$$\sigma_y^{\text{two-servo}}(\tau) \approx 1.1 \times 10^{-15} / \sqrt{\tau/s}$$

as indicated by the black dashed line. Assuming equal noise contributions from the two interleaved servos, $\sigma_y^{\text{two-servo}}(\tau)$ can be divided by $\sqrt{2}$ to extract the single-servo instability:

$$\sigma_y^{\text{single-servo}}(\tau) \approx 7.8 \times 10^{-16} / \sqrt{\tau/s}.$$

To conclude, the measurements presented demonstrate that beam propagation through free space needs to be handled rigorously. Employing a reference fiber for the stabilization of the probe light will be further investigated to achieve better laser-ion coherence times, to improve the clock instabilities, and to suppress frequency shifts related to phase deviations such as AOM chirps.

Chapter 3

Clock comparisons and searches for new physics

The four single-ion $^{171}\text{Yb}^+$ frequency standards at PTB (Yb1, Yb2, Yb3, optical clock) are employed for a variety of frequency comparisons. Furthermore, frequency ratio measurements are performed with a Sr lattice clock operated at PTB [38]. Two caesium fountains [113] serving as primary frequency standards and realizing the SI second enable measurements of the absolute frequencies of the Yb^+ reference transitions [39]. This chapter gives an overview of these atomic clock comparisons.

Part of the data is further analyzed with respect to the search for new physics, often referred to as physics beyond the standard model. The standard model of particle physics (SM) has in general proven to yield good agreement with experimental results [114, 115]. However, there are many indications that it is incomplete: “*Indeed, it is inconsistent with the very existence of our Universe*” [115]. For instance, it does not explain the observed imbalance between matter and antimatter. Furthermore, the theory of gravitation described by general relativity (GR) remains to be unified with the SM. To better understand these inconsistencies, the theoretical models are tested by experiments in the search for limitations of the established theories.

For instance, GR relies on the Einstein equivalence principle (EEP) that itself consists of three main statements [116, 117]:

Universality of free fall (UFF). The trajectory of a freely falling test body is independent of its internal structure and composition.

Local Lorentz invariance (LLI). Any non-gravitational experiment is independent of the velocity and orientation of the reference frame.

Local position invariance (LPI). Any non-gravitational experiment is independent of the location in time and space.

Rigorous tests of the LLI and LPI statements are performed in this chapter:

LLI. An effective field theory commonly known as the standard model extension (SME) [118, 119] can be used to search for violations of LLI in a wide variety of experiments [120]. The SME is a phenomenological framework which contains the SM as a limiting case. Many theories predicting Lorentz violation can be described in the low-energy limit by the SME. While Lorentz violations are possible within the SME for each type of particle separately [115], the discussion here is restricted to a test of LLI for the electron and photon sector: In section 3.2 the E3 transition frequencies in Yb1 and Yb2 are compared for a stringent test of LLI [36] that improves previous limits obtained from atomic spectroscopy experiments [121–123] by one to two orders of magnitude.

LPI. A spatial or time-dependent variation of fundamental constants would result in a violation of LPI, which is searched for in a large variety of experiments [124]. For the fine structure constant α , astronomical observations suggest a spatial variation at the 3.9σ level [125]. In atomic clock experiments, a variation of α would manifest itself in a variation of the atomic transition frequency. Thus, the comparison of transitions with different sensitivities to the value of α can be exploited for a test of LPI. In section 3.3, frequency ratio measurements of the E2 and E3 transition are evaluated for time-dependent variations of α in the solar system in the present epoch, improving existing limits by about a factor of 20 [39]. The data is further analyzed in terms of a coupling of α to gravity. Similar tests are performed for the ratio of the $^{171}\text{Yb}^+$ E3 and the ^{133}Cs ground state hyperfine transition frequency with respect to the proton-to-electron mass ratio μ , as described in section 3.4.

As a side note, the Yb^+ single-ion and Sr lattice clocks at PTB are regularly participating in international clock comparison campaigns together with clocks located for example in institutes in the United Kingdom and France. The resulting data is also used to the search for new physics, tightening constraints on the existence of transient variation of constants and topological defect dark matter [126].

3.1 Experimental infrastructure

The infrastructure used for the comparisons at PTB is discussed and schematically depicted in figure 3.1. The figure is intended to provide a simplified picture of the infrastructure, it is not exhaustive and only parts critical for the forthcoming sections are described. The setup can be separated into three main sections, highlighted by the gray shaded areas: (A) The Yb^+ clock systems and (B) the frequency comb FC1, caesium fountains and hydrogen masers are all located in the clock hall of PTB. (C) In another building, the experiments comprising the Sr clock, frequency comb FC2 and the cryogenic silicon cavity Si-2 [58] are located.

The E3 and E2 clock lasers are locked to optical cavities with a bandwidth of about 500 kHz. The laser light is frequency doubled from 934 nm to 467 nm and 871 nm to 436 nm, respectively, and split to supply the light to the different trap systems. Light is guided from the laser to the individual experiments using path-length stabilized optical fibers. A small fraction of the E3 laser light at the fiber output is directed to a photodiode. The signal is used to stabilize the laser intensity by varying the amplification of the rf signal of an acousto-optic modulator (AOM) in front of the fiber. Thereby, intensity fluctuations at the ion position resulting in variations of the light shift are reduced. In front of each trap, AOMs are used to apply frequency offsets Δf during the clock cycle, to change the laser intensity and to generate the pulses of the clock sequence. The clock cycle is computer-controlled using Artiq hard- and software, which provides monitoring and control of analog and digital signals and the generation of rf signals using direct digital synthesis (DDS). In figure 3.1, only two traps are depicted, but the extension to further trap systems is straightforward by copying the setup of trap 2.

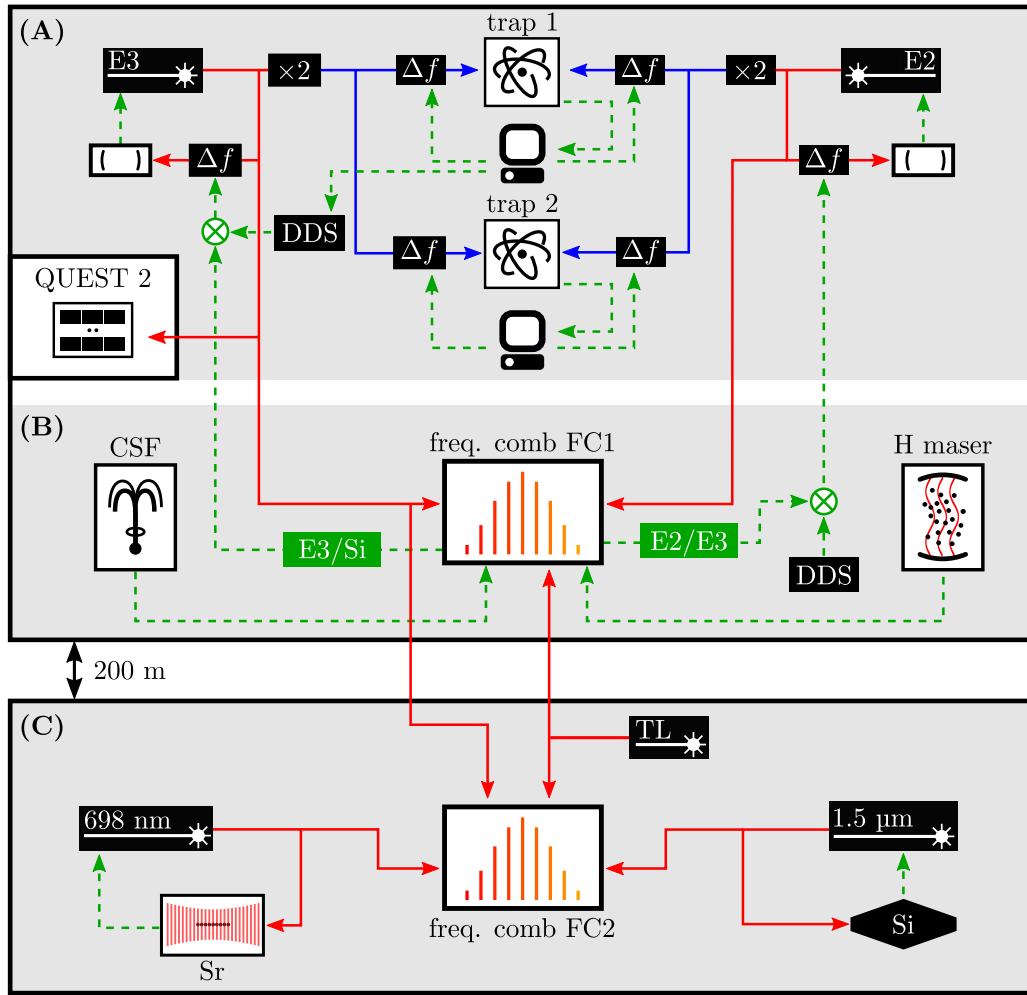


Figure 3.1: **Schematic of the laboratory infrastructure.** Laser paths are depicted by red and blue solid lines, electronic signals by green dashed lines. **(A)** Clock lasers for the E3 and E2 transition are stabilized to optical cavities. The laser light is frequency doubled and sent to the traps. Trap 1 operates as the master clock and the ion signal is used to steer the E3 clock laser frequency via direct digital synthesis (DDS). Frequency offsets Δf are applied locally in front of the trap using acousto-optical modulators. **(B)** The frequency comb FC1 located in the same laboratory is used to interconnect signals of different sources: The stability of a Si cavity is transferred to the E3 laser frequency with the E3/Si signal and the E2/E3 laser beat signal is used to stabilize the E2 laser frequency. Furthermore, the comb allows for the determination of the absolute clock transition frequencies with the caesium fountains (CSF) and for frequency ratio measurements with the Sr clock. **(C)** The frequency comb FC2 is located in a building separated by roughly 200 m from the clock hall. FC2 is connected to FC1 with a transfer laser (TL) and receives light from the E3 clock laser. Lasers locked to the single crystal Si cavity and to the Sr lattice clock are connected to FC2. In yet another building, the research group QUEST 2 is using the E3 clock laser light for experiments on $^{172}\text{Yb}^+$ in a linear ion trap.

Light of both clock lasers is provided to the frequency comb FC1, together with signals from the caesium fountains CSF1 and CSF2 and from a hydrogen maser. Furthermore, light from the E3 laser is sent to FC2 and in combination with a transfer laser TL at a wavelength of $1.5\ \mu\text{m}$ that is shared between both combs, comparisons and evaluation of the two combs are possible. Both the Sr clock and the Si cavity are connected to FC2 via lasers.

The frequency ratio E3/Si is generated at FC1 as a virtual beat at an intermediate frequency of about 80 MHz that is used to stabilize the E3 laser to the Si cavity, enhancing the laser’s short-term stability. Trap system 1 is operated as the master clock, steering the E3 laser frequency via a signal produced by DDS towards the atomic transition frequency. The other transition frequencies are realized locally by applying corrections Δf to the respective AOM in the laser path in front of the ion. The E2 laser frequency is locked with a fixed frequency ratio E2/E3 to the E3 laser frequency. Part of the light of the E3 laser is provided to the research group QUEST 2 “Quantum Clocks and Complex Systems (QuaCCS)”. In this experiment, which is located in another building and employs a linear ion trap, coherent excitation of the E3 transition of the $^{172}\text{Yb}^+$ ion has been performed and its frequency has been measured relative to that realized with $^{171}\text{Yb}^+$ in the Yb1 setup [127].

The availability of the Yb^+ optical clocks has improved continuously over the past few years. This is a result of more robust laser systems, the new setups Yb3 and optclock complementing the existing Yb1 and Yb2 ion trap systems, and new interrogation schemes such as interleaved operation of the E2 and E3 transition. At the same time, parts of the data evaluation process have been automated to analyze the clock data more efficiently. The real-time measurement and correction of second-order Zeeman (section 2.3.6) or electric quadrupole shifts (section 2.3.8) are examples for the improvement of the control software. Moreover, the validation of clock data is extended, e.g. by monitoring the micromotion amplitude during clock operation as discussed in section 2.3.5. The surveillance is further extended to the surrounding infrastructure: Lab temperature is recorded at different positions in the clock hall, laser power and stabilization to optical cavities is monitored, and frequency counters recording fiber stabilization signals have watchdog timers implemented to report failures.

3.2 Direct comparison of the E3 transition and test of local Lorentz invariance

In 2017, a six-months-long comparison of the electric octupole transitions realized by the two clocks Yb1 and Yb2 has been performed as shown in figure 3.2 (A), with a total amount of data corresponding to 3.9×10^6 s of measurement time. This comparison and its results have been published in [36]. As explained in figure 3.1, one clock (Yb1) is steering the clock laser while the second clock (Yb2) realizes a local frequency offset. The uncertainty budgets compiled for both systems are given in table 3.1. With a frequency instability of $\sigma_y(\tau) = 1.4 \times 10^{-15} / \sqrt{\tau}$, a statistical uncertainty of 2.1×10^{-18} is determined from the last point of the Allan deviation shown in figure 3.2 (B). Together with a fractional systematic uncertainty of 3.6×10^{-18} , a fractional offset of

$$\Delta\nu_{1-2}/\nu_0 = 2.8(4.2) \times 10^{-18}$$

has been found after correcting for frequency shifts of the two clocks. It is worth noting that even though the same clock transition has been interrogated, the two setups show substantial differences as depicted in table 3.2.

Having observed good agreement between the two systems and the expected white frequency noise behavior, the data is well suited to be further analyzed for searches for new physics. The non-spherical ${}^2F_{7/2}$ clock state of Yb^+ is a suitable candidate to perform a test of LLI in the framework of the SME [128], searching for an anisotropy of spacetime. Stringent tests of LLI have been performed with other atomic systems as well, including neutral Dy atoms [121] and Ca^+ ions [122, 123]. In the SME, a symmetry-breaking tensor $c_{\mu\nu}$ is added to the kinetic term in the SM Lagrangian, yielding an energy shift of the form [122]

$$\delta H = -C_0^{(2)} \frac{\mathbf{p}^2 - 3p_z^2}{6m} \quad (3.1)$$

between two bound electronic states with the electron mass m and with \mathbf{p} and p_z the momentum of a bound electron¹ and its projection along the quantiza-

¹Even though the derivation is based on Lorentz violation in the electron sector, the results can not be separated from Lorentz violation of the photon sector. With a suitable choice of the coordinate system, the results discussed here describe limits to the differential electron-photon anisotropies that can be interpreted both in terms of the electronic dispersion as well

Shift effect	$\Delta\nu_1/\nu_{E3}$	$\Delta\nu_2/\nu_{E3}$	$\Delta\nu_{1-2}/\nu_{E3}$
Second-order Doppler	-2.3 (1.5)	-4.0 (2.2)	1.7 (2.7)
Blackbody radiation	-70.5 (1.8)	-69.9 (1.7)	-0.6 (1.7)
Probe light	0 (0.8)	0 (0.5)	0 (0.9)
Second-order Zeeman	-10.4 (0.2)	-11.3 (0.4)	0.9 (0.4)
Quadratic dc Stark	-0.8 (0.6)	-1.3 (0.8)	0.5 (1.0)
Quadrupole	-5.7 (0.5)	-3.9 (0.5)	-1.8 (0.7)
Background gas	0 (0.5)	0 (0.5)	0 (0.7)
Servo	0 (0.2)	0 (0.1)	0 (0.1)
Gravitation	-0.5 (0.1)	0 (0.1)	-0.5 (0.1)
Total	-90.2 (2.7)	-90.4 (3.0)	0.2 (3.6)

Table 3.1: **Uncertainty budgets for Yb1 and Yb2** in fractional frequency units divided by 10^{-18} . For the fractional frequency difference $\Delta\nu_{1-2}/\nu_{E3}$, common-mode uncertainties, for example related to the atomic polarizability, are suppressed.

Yb1	
trap geometry	quadrupole Paul trap with conical electrode shapes
control software	Labview
interrogation seq.	Rabi-controlled hyper-Ramsey, Rabi and accordingly tuned Ramsey pulses alternated
fiber stabilization	one stabilized clock laser fiber, AOM after fiber
<hr/>	
Yb2	
trap geometry	endcap-trap design
control software	Matlab
interrogation seq.	Rabi-controlled Ramsey, frequency-shift keying between drive-pulse and dark-time intervals
fiber stabilization	AOM before clock fiber, stab. with reference fiber

Table 3.2: **Differences of the Yb1 and Yb2 setups** in the configurations used for the measurement interval in 2017.

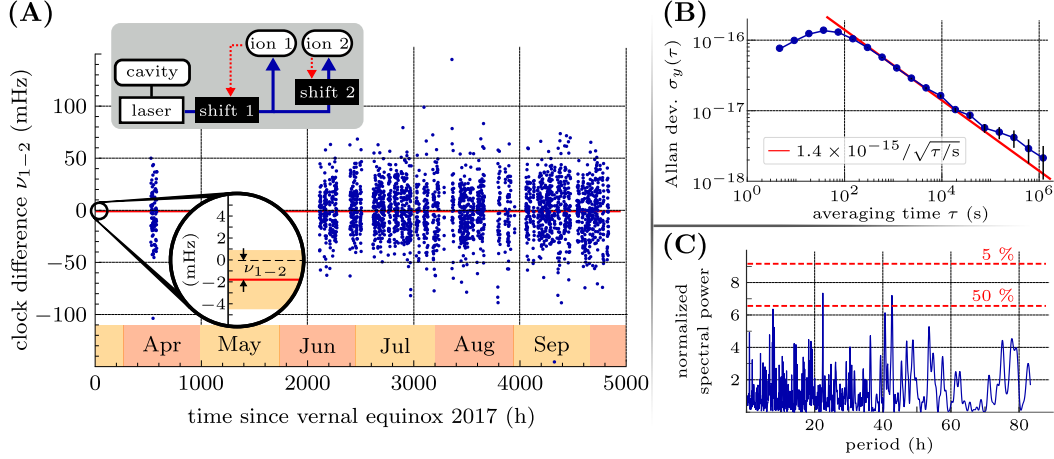


Figure 3.2: **E3 clock comparison of Yb1 and Yb2.** (A) For a period of six months in 2017, the two transition frequencies have been compared and a frequency difference of 1.8(2.7) mHz has been obtained. (B) Allan deviation of the clock comparison with an instability of $1.4 \times 10^{-15} / \sqrt{\tau/s}$. (C) Normalized Lomb periodogram with the dashed line indicating the significance levels: The probabilities of finding at least one peak in an uncorrelated data set above the lower line is 50 %, above the upper line 5 %. Hence there is no periodic signal of high significance found. The figure is adapted from [36].

tion axis z . The factor $C_0^{(2)} = c_{xx} + c_{yy} - 2c_{zz}$ contains spatial elements of the $c_{\mu\nu}$ tensor that is defined as

$$c_{\mu\nu} = \begin{pmatrix} c_{tt} & c_{tx} & c_{ty} & c_{tz} \\ c_{tx} & c_{xx} & c_{xy} & c_{xz} \\ c_{ty} & c_{xy} & c_{yy} & c_{yz} \\ c_{tz} & c_{xz} & c_{yz} & c_{zz} \end{pmatrix}. \quad (3.2)$$

The bound electron momentum can be expressed by the quadrupole moment operator $T_0^{(2)} = \mathbf{p}^2 - 3p_z^2$. Its expectation value depends on the specific electronic state and becomes exceptionally large [128] for the $^2F_{7/2} |F = 3, m_F = 0\rangle$ clock state with

$$\langle T_0^{(2)} \rangle / 6m = hq = h \times 2.6 \times 10^{16} \text{ Hz}$$

and h the Planck constant. The isotropic ground state $^2S_{1/2}$ is Lorentz violation insensitive. The $c_{\mu\nu}$ tensor is frame-dependent, for comparison of different

as the photon-mediated Coulomb field [122, 129]. Although the ^{171}Yb nucleus possesses an unpaired neutron, the nucleon sector does not contribute because with nuclear spin $I = 1/2$, the term in equation (3.1) for the neutron kinetic energy vanishes [130].

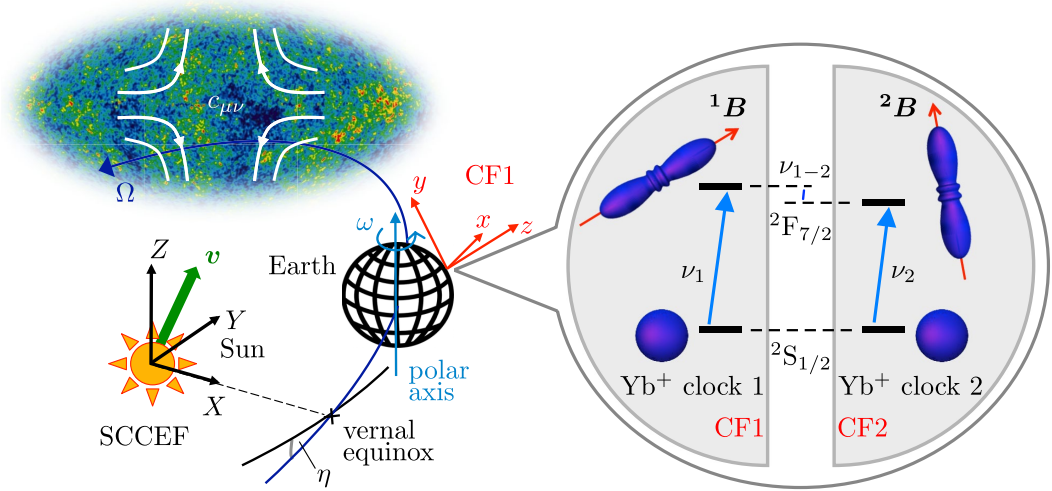


Figure 3.3: **Test of LLI using two Yb^+ clocks** with the two clock frames CF1 and CF2 oriented along different directions and the ion quantization axes, determined by the magnetic fields ${}^1\mathbf{B}$ and ${}^2\mathbf{B}$, aligned with the z axis of the respective frame. The Sun-centered celestial equatorial frame (SCCEF) moves with constant velocity v with respect to the cosmic-microwave-background rest frame. The Earth rotates around its axis with frequency ω and orbits the Sun with frequency Ω . In both clocks, the E3 transition is employed and a modulation of the frequency difference ν_{1-2} at combinations of ω and Ω is searched for. The figure is adapted from [36].

experiments typically the uniquely defined Sun-centered celestial equatorial frame (SCCEF) is chosen. A change of the quantization axis orientation of the individual ions using externally applied magnetic fields ${}^1\mathbf{B}$ and ${}^2\mathbf{B}$ gives rise to a change in the values ${}^{1,2}C_0^{(2)}$. In this notation, left-side indices 1 and 2 indicate clock 1 and 2, respectively. For the full measurement time, a fixed orientation for ${}^1\mathbf{B}$ and ${}^2\mathbf{B}$ has been used. Consequently, the ${}^{1,2}C_0^{(2)}$ values only change due to motion of the Earth, and the $c_{\mu\nu}$ tensor components c_{mn} in the clock reference frames CF1 and CF2 can be mapped to the components c_{MN} in the SCCEF frame using Lorentz transformations:

$${}^{1,2}c_{mn} = {}^{1,2}\Lambda_m^M {}^{1,2}\Lambda_n^N c_{MN}, \quad (3.3)$$

$$\Lambda = \begin{pmatrix} 1 & -\beta_1 & -\beta_2 & -\beta_3 \\ (-R\beta)_1 & & & \\ (-R\beta)_2 & R & & \\ (-R\beta)_3 & & & \end{pmatrix}, \quad (3.4)$$

with R a rotation matrix and β a boost vector defined in the specific laboratory frame, which can be found in [36] for the experiment described here. In this notation, lower case indices stand for the clock frames and upper case indices for the SCCEF frame. The different frames are visualized in figure 3.3.

The rotation matrix and boost term incorporate rotations at the angular frequencies of the sidereal day $\omega = 2\pi/(23.934 \text{ h})$ and the sidereal year $\Omega = 2\pi/(365.256 \times 24 \text{ h})$, respectively. The time-dependent ${}^{1,2}C_0^{(2)}(t)$ terms for both clocks are linear combinations of trigonometric functions at these angular frequencies and their mixtures. A suitable, constant choice for the ions' quantization axes orientations in the ion reference frames during the full measurement time permits to search for time-dependent frequency changes by fitting the acquired data to the function

$$\nu_{1-2}(t) = -q[{}^1C_0^{(2)}(t) - {}^2C_0^{(2)}(t)]. \quad (3.5)$$

In particular, this includes the search for oscillations at the angular frequencies ω and Ω as well as 2ω , $\Omega \pm \omega$ and $\Omega \pm 2\omega$. The data timestamps are referenced to the vernal equinox of 2017. Equation (3.5) can be decomposed into contributions from the individual c_{MN} components oscillating at the different frequencies described by the prefactors $f_{1-7}(t)$:

$$\begin{aligned} \nu_{1-2}(t) = & c_{TX}f_1(t) + c_{TY}f_2(t) + c_{TZ}f_3(t) + c_{XZ}f_4(t) \\ & + c_{YZ}f_5(t) + (c_{XX} - c_{YY})f_6(t) + c_{XY}f_7(t). \end{aligned} \quad (3.6)$$

The c_{MN} components can be compared to limits obtained from measurements with other atomic systems and from astrophysical observations as shown in table 3.3. The reduced chi-squared for the fit of the data to equation (3.6) yields $\chi_{\text{red}}^2 = 1.05$. It should be noted that the c_{MN} components are correlated since the covariance matrix of the fit contains non-zero off-diagonal elements. However, uncorrelated linear combinations can be constructed and are given in [36]. In conclusion, the new limits given in table 3.3 are consistent with zero and thereby do not indicate a Lorentz violation. Apart from c_{TZ} , the uncertainties of all components are improved by one to two orders of magnitude.

	New limits [36]	Ca ⁺ limits [123]	Dy limits [121]	Astrophysical limits [131]
c_{X-Y}	$-0.5 \pm 1.7 \times 10^{-20}$	$6.2 \pm 9.2 \times 10^{-19}$	$2.9 \pm 5.7 \times 10^{-17}$	$3.3 \pm 6.2 \times 10^{-15}$
c_{XY}	$-7.0 \pm 8.1 \times 10^{-21}$	$2.4 \pm 4.8 \times 10^{-19}$	$0.7 \pm 3.6 \times 10^{-17}$	$0.0 \pm 3.0 \times 10^{-15}$
c_{XZ}	$0.8 \pm 1.3 \times 10^{-20}$	$0.8 \pm 2.1 \times 10^{-19}$	$0.9 \pm 1.1 \times 10^{-16}$	$0.0 \pm 3.0 \times 10^{-15}$
c_{YZ}	$1.0 \pm 1.3 \times 10^{-20}$	$-3.1 \pm 2.2 \times 10^{-19}$	$3.1 \pm 6.6 \times 10^{-17}$	$-0.4 \pm 2.2 \times 10^{-15}$
c_{TX}	$-0.4 \pm 8.5 \times 10^{-17}$		$5.7 \pm 8.3 \times 10^{-15}$	$-1.5 \pm 5.5 \times 10^{-15}$
c_{TY}	$4.4 \pm 8.7 \times 10^{-17}$		$-8.3 \pm 7.5 \times 10^{-13}$	$0.5 \pm 1.0 \times 10^{-15}$
c_{TZ}	$-1.2 \pm 1.6 \times 10^{-16}$		$1.9 \pm 1.7 \times 10^{-12}$	$-1.0 \pm 3.0 \times 10^{-17}$

Table 3.3: **New limits on the differential Lorentz violating parameters.** The individual component values c_{MN} are given here for a direct comparison to results obtained with other atomic systems and from astrophysical observations.

3.3 Measurement of the E3/E2 transition ratio and test of α variation

From May 2016 onwards, the ratio of the two clock transitions has been measured regularly, with Yb1 realizing the E2 and Yb2 the E3 transition frequency for most of the time. Since the beginning of 2020, it is possible to measure both transitions interleaved in a single system, enabling a direct measurement with the Yb1 ion only. This change of the system realizing the E3 transition frequency is expected to have no relevant effect on the measured ratio, since an agreement of the E3 transition frequencies for Yb1 and Yb2 at the low 10^{-18} level has been found as discussed in section 3.2. The results of the E3/E2 transition ratio measurements have been published in [39].

The E2 probe laser frequency is stabilized at the frequency comb FC1 with fixed ratio $1/R_0$ to the E3 probe laser frequency as visualized in figure 3.1. The E3 transition frequency is realized by steering the probe laser directly, while the atomic E2 transition frequency is tracked by an AOM that induces the frequency detuning Δf_{E2} . The frequency shifts $\Delta\nu_{E2}$ and $\Delta\nu_{E3}$ are assessed from the uncertainty budgets. The frequency ratio is obtained using

$$R_{E3,E2} = \nu_{E3}/\nu_{E2} = R_0 \left(1 + \frac{\Delta f_{E2}}{\nu_{E2}} + \frac{\Delta\nu_{E2}}{\nu_{E2}} - \frac{\Delta\nu_{E3}}{\nu_{E3}} \right). \quad (3.7)$$

The E3 uncertainty budgets have been introduced in section 3.2 and play

Effect	$\Delta\nu_{\text{E2}}/\nu_{\text{E2}}$	$u_{\text{E2}}/\nu_{\text{E2}}$	$r_{\text{E2}}/\nu_{\text{E2}}$
Blackbody radiation	-495	27	3
Quadrupole	0	14	14
Second-order Zeeman (rf)	0	10	1
Second-order Zeeman (dc)	463	6	6
Second-order Stark	-2.0	2	2
Second-order Doppler	-1.0	1	1
Servo	0	1	1
Total	-35	33	16

Table 3.4: **Uncertainty budget of the Yb1 E2 transition.** Frequency shifts $\Delta\nu_{\text{E2}}$, uncertainties u_{E2} and reproducibilities r_{E2} are all given in fractional frequency units divided by 10^{-18} .

a negligible role for the total uncertainty. The E2 uncertainty for Yb1 is summarized in table 3.4. For tests of fundamental physics, the reproducibility r_{E2} , accounting for potentially varying systematic frequency shifts, needs to be considered. In particular, uncertainties of atomic parameters, such as the differential polarizability, are not directly contributing to the reproducibility.

The results of 11 measurements over a period of more than four years is shown in figure 3.4. Taking only the statistical uncertainty into account, a reduced chi-squared value $\chi_{\text{red}}^2 = 1.3$ is obtained. Adding the fractional reproducibility of 1.6×10^{-17} in quadrature results in $\chi_{\text{red}}^2 = 0.8$. The weighted average of all measurements yields the ratio

$$R_{\text{E3,E2}} = 0.932\,829\,404\,530\,965\,376(32)$$

with a total fractional uncertainty of 34×10^{-18} dominated by the systematic uncertainty of the E2 transition. The statistical uncertainty of 6×10^{-18} and the systematic uncertainty of 3×10^{-18} for the E3 transition are small contributions to the total uncertainty. Compared to a previous direct measurement of the ratio [91], the value found here is about 2.3 combined standard uncertainties larger and the uncertainty is reduced by one order of magnitude. Another ratio reported in [42] is derived from absolute frequency measurements of ν_{E3} and ν_{E2} , has a fractional uncertainty of 5.4×10^{-16} , and in comparison, the value given here is about 1.6 combined standard uncertainties smaller.

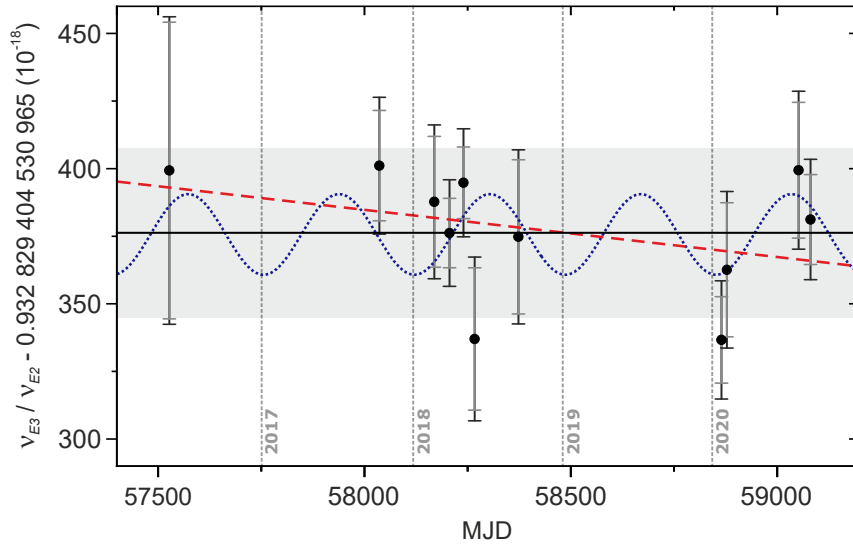


Figure 3.4: **Measurement of the E3/E2 transition frequency ratio $R_{E3,E2}$** for a period of more than four years, with Yb1 realizing the E2 transition frequency. The gray error bars yield statistical uncertainties, the black error bars the square root of the quadratic sum of statistical uncertainty and reproducibility. The solid line shows the weighted average and the gray background the total uncertainty of the frequency ratio. The red dashed line and the blue dotted sinusoid are fits to searches of violations of local position invariance. The figure is adapted from [39].

In the following, the data is further evaluated in terms of variations of fundamental constants. The transition frequencies ν_{el} and ν_{hfs} between electronic and hyperfine structure energy levels, respectively, can be expressed by [115]

$$\nu_{el} \propto cR_{\infty}CF(\alpha), \quad (3.8)$$

$$\nu_{hfs} \propto \alpha^2 cR_{\infty}C_{hfs}F_{hfs}(\alpha)G(1/\mu, g_i), \quad (3.9)$$

with $R_{\infty} = \alpha^2 m_e c^2 / (2hc)$ the Rydberg constant that contains the rest mass energy of the electron $m_e c^2$ and the fine structure constant α . The nonrelativistic atomic structure is described by the numerical factors C and C_{hfs} . Relativistic corrections specific to each transition are described by $F(\alpha)$ and $F_{hfs}(\alpha)$. The function $G(1/\mu, g_i)$ depends on the proton-to-electron mass ratio $\mu = m_p/m_e$, and the g factor associated with the nuclear magnetic moment μ_i . The g factor contains a dependence on the strong-interaction parameter $X_q = m_q/\Lambda_{QCD}$, which is the ratio of the average quark mass m_q and the quantum chromodynamic scale Λ_{QCD} .

The frequency ratio $R = \nu_{el,1}/\nu_{el,2}$ of two optical transitions can be analyzed in terms of variations of α using the relation $d \ln(R)/dt = (1/R)(dR/dt)$, which results in

$$\frac{1}{R} \frac{dR}{dt} = \kappa_\alpha \frac{1}{\alpha} \frac{d\alpha}{dt}, \quad (3.10)$$

with

$$\kappa_\alpha = \frac{\alpha}{F_1(\alpha)} \frac{dF_1(\alpha)}{d\alpha} - \frac{\alpha}{F_2(\alpha)} \frac{dF_2(\alpha)}{d\alpha}. \quad (3.11)$$

In the case of the E3/E2 transition ratio in $^{171}\text{Yb}^+$, $\kappa_\alpha(R_{\text{E3,E2}}) = -6.95$ [77]. A linear fit to the data, shown in figure 3.4 by the dashed red line, yields

$$\frac{1}{R_{\text{E3,E2}}} \frac{dR_{\text{E3,E2}}}{dt} = -6.8(7.5) \times 10^{-18}/\text{yr}$$

and consequently

$$\frac{1}{\alpha} \frac{d\alpha}{dt} = 1.0(1.1) \times 10^{-18}/\text{yr}.$$

It is the first significant improvement of this value since 2008, when a stringent limit on $d\alpha/dt$ was obtained from measurements of the Hg^+/Al^+ frequency ratio [101]. The result presented here tightens that constraint by more than a factor of 20. In 2014, two measurements improved the limit obtained in 2008 by about 10 % [91, 132], based on combined analysis of several experiments contributing to $d\alpha/dt$ and $d\mu/dt$.

Furthermore, the data can be evaluated in terms of a coupling of α to gravity by searching for an oscillation of the frequency ratio due to the variation of the Sun's gravitational potential $\Phi(t)$ on Earth at a cycle time T_a of the anomalistic year:

$$\Phi(t) = \Delta\Phi_0 \cos(2\pi(t - t_p)/T_a) \quad (3.12)$$

with $\Delta\Phi_0 \approx 1.65 \times 10^{-10}c^2$. Performing a non-linear least square fit of the frequency ratio data,

$$R_{\text{E3,E2}}(t) = A \cos(2\pi(t - t_p)/T_a) + B, \quad (3.13)$$

with t_p the perihelion of 2018 and A, B the fitting parameters, the relative oscillation amplitude

$$\frac{A}{R_{\text{E3,E2}}} = -16(13) \times 10^{-18}$$

is obtained. This corresponds to a change of the relative frequency ratio in dependence of the gravitational potential

$$\frac{1}{R_{E3,E2}} \frac{dR_{E3,E2}}{d\Phi} = -9.7(7.7) \times 10^{-8}/c^2$$

and results in a limit for the coupling of α to gravity of

$$\frac{1}{\alpha} \frac{d\alpha}{d\Phi} = 14(11) \times 10^{-9}/c^2,$$

improving the existing limit by one order of magnitude [133].

3.4 Absolute frequency measurement of the E3 transition and test of μ variation

Over a time span of nine years, from 2010 to 2019, comparisons of the E3 transition frequency realized by Yb1 with the ^{133}Cs hyperfine transition frequency provided by the two caesium fountains CSF1 and CSF2 [113] in the clock hall have been conducted. The results have been published in [39]. From the measurements, the absolute frequency ν_{E3} of the E3 transition is extracted, as presented in figure 3.5. The data points are shown with respect to

$$\nu_{E3,\text{SRS}} = 642\,121\,496\,772\,645 \text{ Hz},$$

which is the recommended value of the E3 transition frequency for the Secondary Representation of the SI Second (SRS), provided by the International Committee for Weights and Measures [134]. It is based on measurements performed at the National Physical Laboratory in the United Kingdom and at PTB before 2015. The data points in figure 3.5 before 2017 are not taken into account for the absolute frequency value, but for the investigation of frequency variations. The value of 2010 has been reported in [75], the value of 2012 in [132]. The value in 2015 has been acquired during a European clock comparison campaign [135].

From 2017 to 2019, 2478 and 4394 hours of measurement of Yb1 with CSF1 and CSF2 have been acquired, respectively. The data is analyzed indepen-

dently for the two caesium clocks. Interruptions of the operation of Yb1 shorter than one day are bridged by a hydrogen maser acting as a flywheel oscillator. Such an approach is chosen since for short uptime intervals of the optical clock, the instability of the fountain clocks at the level of low $10^{-13}/\sqrt{\tau/s}$ dominates the statistical uncertainty of the measurement. Comparing the hydrogen maser with the optical clock during its operation, and on much longer timescales with the caesium fountains that have a significantly higher availability, the actual measurement time can be extended at the cost of an additional uncertainty due to the extrapolation, which can be calculated with knowledge of the maser properties [136, 137]. An average absolute frequency value of

$$\nu_{E3} = 642\,121\,496\,772\,645.10(8) \text{ Hz}$$

has been found from the individually measured frequencies

$$\nu_{E3,CSF1} = \nu_{E3} - 0.09(13) \text{ Hz},$$

$$\nu_{E3,CSF2} = \nu_{E3} + 0.08(11) \text{ Hz}.$$

Dominated by the systematic uncertainties at the low 10^{-16} level of the caesium fountains, the total fractional uncertainty yields 1.3×10^{-16} , which is a reduction of more than a factor three compared to previous measurements [22, 132] and represents currently the most accurate absolute value for an optical transition frequency. In combination with the frequency ratio derived in section 3.3, an absolute frequency value for the E2 transition can be given:

$$\nu_{E2} = 688\,358\,979\,309\,308.22(9) \text{ Hz}.$$

In direct analogy to the investigation for variations of the fine structure constant α discussed in the last section, the data shown in figure 3.5 can be used for an evaluation of variations of the proton-to-electron mass ratio μ : From equations (3.8) and (3.9), the temporal dependence of the frequency ratio of an electronic and a hyperfine transition on the three quantities α , μ , and X_q can be described by [42, 115, 138]

$$\frac{1}{R} \frac{dR}{dt} = \kappa_\alpha \frac{1}{\alpha} \frac{d\alpha}{dt} + \kappa_q \frac{1}{X_q} \frac{dX_q}{dt} + \kappa_\mu \frac{1}{\mu} \frac{d\mu}{dt}, \quad (3.14)$$

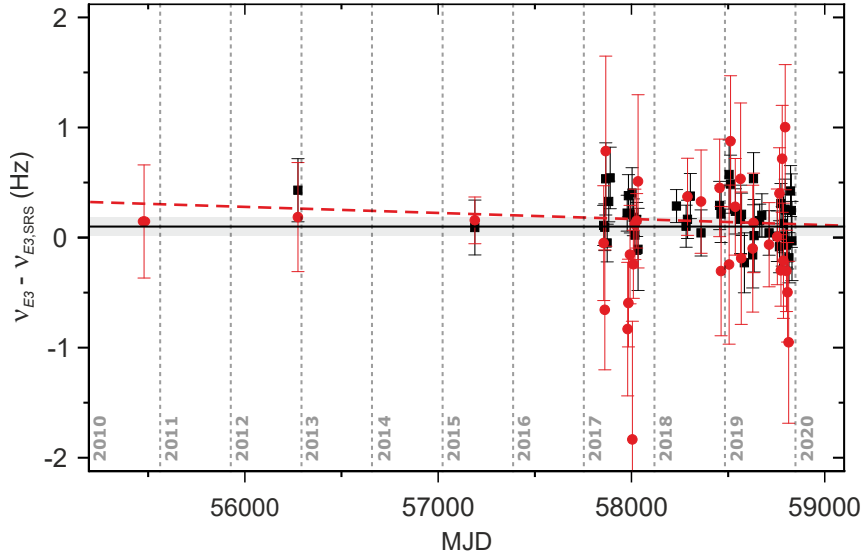


Figure 3.5: **Absolute transition frequency ν_{E3}** in a comparisons of Yb1 to the caesium fountains CSF1 (red dots) and CSF2 (black squares) at PTB for a period of more than nine years. The data points are shown with respect to the recommended value for the transition frequency, $\nu_{E3,SRS}$. Data since 2017 is used to calculate the weighted mean (black line) and its uncertainty (gray background). All data points are evaluated to search for a temporal drift, depicted by the red dashed line. The figure is adapted from [39].

similar to the expression in equation (3.10) The relative sensitivities κ_α , κ_q and κ_μ are derived from many-body calculations [77]. For the frequency ratio $R_{E3,Cs}$, the absolute frequency values are divided by the conventional value of the ^{133}Cs ground state hyperfine transition frequency of 9 192 631 770 Hz. The sensitivity factors of the frequency ratio are given by $\kappa_\alpha(R_{E3,Cs}) = -8.78$ [77], $\kappa_q(R_{E3,Cs}) = -0.002$ [138] and $\kappa_\mu(R_{E3,Cs}) = 1$ [139]. The linear drift of the ratio, marked by the dashed red line in figure 3.5, is determined as

$$\frac{1}{R_{E3,Cs}} \frac{dR_{E3,Cs}}{dt} = -3.1(3.4) \times 10^{-17}/\text{yr}.$$

Using equation (3.14), the limit on variations of α derived in the last section, and $\kappa_q(R_{E3,Cs})(1/X_q)(dX_q/dt) = -0.14(9) \times 10^{-16}/\text{yr}$ [140], the limit for the variation of μ is calculated to be

$$\frac{1}{\mu} \frac{d\mu}{dt} = -8(36) \times 10^{-18}/\text{yr},$$

improving the existing limits by about a factor of 2 [14, 141]. Additionally, the coupling of μ to gravity can be investigated in the same way as performed for α . A relative oscillation amplitude of

$$\frac{A}{R_{\text{E3,Cs}}} = -7(72) \times 10^{-18}$$

is obtained for the data in figure 3.5. This can be expressed in terms of the frequency ratio by

$$\frac{1}{R_{\text{E3,Cs}}} \frac{dR_{\text{E3,Cs}}}{d\Phi} = -4(44) \times 10^{-8}/c^2.$$

With the limit on gravitational coupling on α from the last section and with an oscillation amplitude obtained from comparisons between caesium clocks and hydrogen masers [142], $\kappa_q(R_{\text{E3,Cs}})(1/X_q)(dX_q/d\Phi) = 43(45) \times 10^{-10}/c^2$ can be derived. This is used to constrain the gravitational coupling of μ to

$$\frac{1}{\mu} \frac{d\mu}{d\Phi} = 7(45) \times 10^{-8}/c^2,$$

which is a slight improvement upon the limit $35(59) \times 10^{-8}/c^2$ obtained in [14].

3.5 Frequency ratio of $^{171}\text{Yb}^+$ and ^{87}Sr

There are several other optical atomic clocks being developed at PTB apart from the $^{171}\text{Yb}^+$ single-ion frequency standards, among them optical lattice clocks based on ^{87}Sr . Frequency comparisons between these systems are performed on a regular basis. In particular, between December 2012 and October 2019, a series of 109 measurements has been conducted between Yb1 and a stationary ^{87}Sr lattice clock (Sr) that is shown in figure 3.6. The results are published in [38].

Over the last years, both systems have been continuously updated, for example to improve the short-term stability of the clock lasers by stabilizing to the signal of the Si-cavity. For the most recent comparisons, the infrastructure discussed in section 3.1 has been used. While Yb1 employs the E3 transition for these comparisons, the Sr clock is operated on the $(5s^2)^1\text{S}_0 \rightarrow (5s5p)^3\text{P}_0$ transition at a frequency of $\nu_{\text{Sr}} \approx 429$ THz.

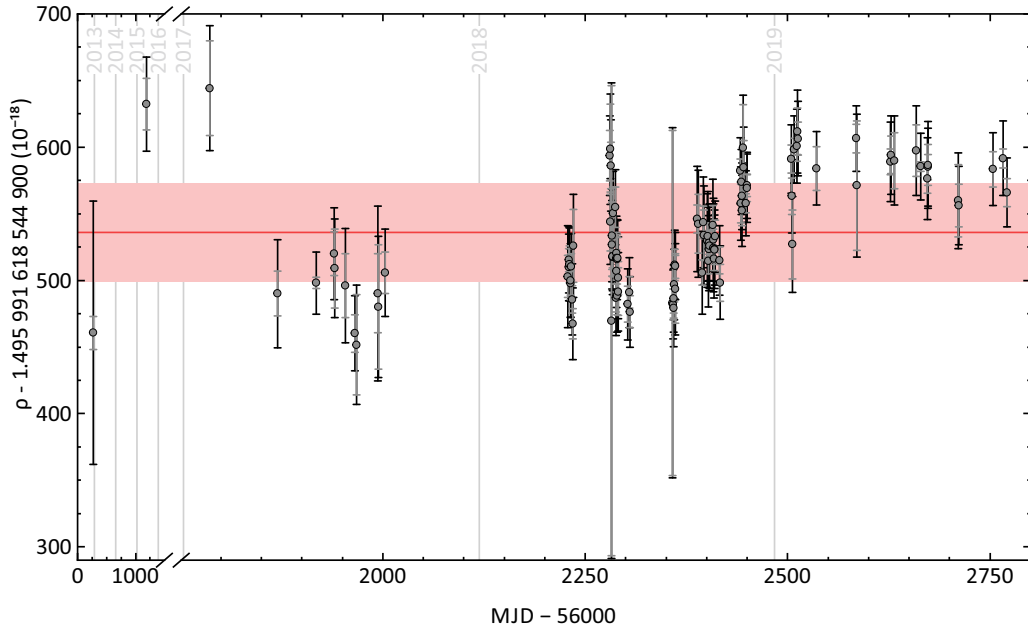


Figure 3.6: **Ratio of the $^{171}\text{Yb}^+$ E3 and the $^{87}\text{Sr} (5s^2)^1\text{S}_0 \rightarrow (5s5p)^3\text{P}_0$ transition** measured between 2012 and 2019 with Yb1 and the stationary Sr lattice clock at PTB. The gray error bars show the statistical, the black error bars the total uncertainty. The red line is the weighted average and the red background the respective uncertainty of the frequency ratio. The figure is taken from [38].

The relative systematic uncertainty of the comparison is dominated by the contribution from the Sr lattice clock of 1.5×10^{-17} . The fractional instability of the comparison yields approximately $1.0 \times 10^{-15}/\sqrt{\tau/\text{s}}$, limited by Yb1 and corresponding to a relative statistical uncertainty of low 10^{-17} after a few hours of measurement time. Therefore, the total fractional uncertainty of an individual measurement point is typically on the order of 2.5×10^{-17} . The full data set in figure 3.6 shows $\chi_{\text{red}}^2 = 1.9$. Since no deviation from white frequency noise in the instability is found for measurement intervals up to a few days, the excess scatter indicated by the reduced chi-square value appears on a long-term scale related to slow frequency drifts. Despite an extensive investigation that includes changes in the experimental setups and deliberate increase of individual frequency shift contributions, the cause of the excess scatter has not been identified. To account for the unknown variation, the uncertainty of each measurement is increased by an additional uncertainty contribution $u_{\text{add}}/R_{\text{Yb1,Sr}} = 1.8 \times 10^{-17}$ to fulfill the requirement $\chi_{\text{red}}^2 = 1$. This yields the

frequency ratio

$$R_{\text{Yb1,Sr}} = \frac{\nu_{\text{Yb1}}}{\nu_{\text{Sr}}} = 1.495\,991\,618\,544\,900\,537(38)$$

visualized by the red line in figure 3.6, with a fractional frequency uncertainty of 2.5×10^{-17} . This is first reported value for the direct measurement between these two atomic species and the uncertainty of the frequency ratio is improved by one order of magnitude with respect to values obtained from absolute frequency measurements [14, 132, 143]. Despite the additional uncertainty, this is one of the best frequency ratio measurements to date. There is one measurement campaign that has reported lower uncertainties of frequency ratios [12], which are listed in table 1.1 of section 1.3.

3.6 Spectroscopy of the ${}^2\text{F}_{7/2}$ $F = 3$ to $F = 4$ hyperfine transition

The electronic transitions in Yb^+ , with transition energies in the optical regime, are not the only transitions that can be exploited for high-precision frequency measurements and for tests of fundamental physics: It has also been proposed to employ a transition between the hyperfine sublevels of the ${}^2\text{F}_{7/2}$ manifold for a test of local Lorentz invariance [128, 144]. In the following it will be shown that our Yb^+ systems are readily set up for precision spectroscopy and clock operation on various magnetic sublevels of the ${}^2\text{F}_{7/2}$ $|F = 3\rangle \rightarrow |F = 4\rangle$ hyperfine transition.

In order to drive the hyperfine transition, first the atom needs to be prepared in the ${}^2\text{F}_{7/2}$ $|F = 3\rangle$ state, which is performed in full analogy to the procedure used to interrogate the E3 transition frequency: After successful excitation of the transition (confirmed by the electron shelving technique), the ion remains for minutes to hours in the excited clock state that is eventually depopulated by collisions and off-resonant coupling to dipole allowed transitions due to blackbody radiation. Therefore, the microwave spectroscopy is in practice not limited by the excited state lifetime. To drive the hyperfine transition, microwave radiation pulses are employed. In figure 3.7 (A) the result of a Rabi-flopping experiment for the $|F = 3, m_F = 0\rangle \rightarrow |F = 4, m_F = 0\rangle$

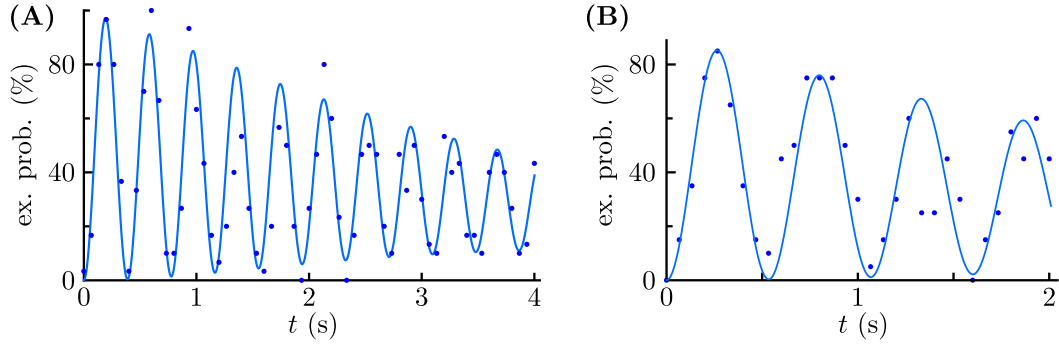


Figure 3.7: **Rabi-flopping experiments on the hyperfine transitions of the ${}^2F_{7/2}$ state.** (A) Probing the $|F = 3, m_F = 0\rangle \rightarrow |F = 4, m_F = 0\rangle$ transition that shows a coherence with at least 80 % contrast for more than one second. (B) Probing the first-order magnetic field sensitive $|F = 3, m_F = 0\rangle \rightarrow |F = 4, m_F = 1\rangle$ transition with a similar coherence time.

transition is presented, showing coherence with at least 80 % contrast for more than one second. For the first-order magnetic field sensitive transition $|F = 3, m_F = 0\rangle \rightarrow |F = 4, m_F = 1\rangle$, a similar result is found, as pictured in figure 3.7 (B). This demonstrates immunity to external magnetic field fluctuations, provided by the μ -metal shielding surrounding the ion trap. For both Rabi-flopping experiments, an exponential decay term has been added to the Rabi-flopping formula in equation (1.43) for a fit of the data points, with time constants $\tau_{|3,0\rangle \rightarrow |4,0\rangle} = 6(1)$ s and $\tau_{|3,0\rangle \rightarrow |4,1\rangle} = 6(3)$ s, which resembles a relaxation of the excited state that is still under investigation.

Clock operation has been performed on various magnetic sublevels of the hyperfine transition. As an example that is sensitive to a linear Zeeman shift, interleaved clock operation on the

$$\begin{aligned} |+\rangle &= |F = 3, m_F = 0\rangle \rightarrow |F = 4, m_F = +1\rangle, \\ |-\rangle &= |F = 3, m_F = 0\rangle \rightarrow |F = 4, m_F = -1\rangle \end{aligned}$$

transitions is discussed here. The clock has been operated continuously for 96 hours with a Ramsey dark time $T_R = 800$ ms. Two additional servos are used for stabilization of the E3 transition frequency in a Rabi-controlled Ramsey scheme. An instability of $0.62 \text{ Hz}/\sqrt{\tau/\text{s}}$ depicted in figure 3.8 yields a statistical uncertainty of 1 mHz. The mean frequency of the two transitions,

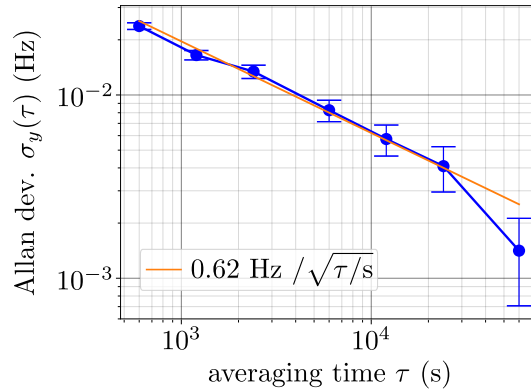


Figure 3.8: **Instability of interleaved microwave clock operation** performed continuously for 96 hours on the $|F = 3, m_F = 0\rangle \rightarrow |F = 4, m_F = \pm 1\rangle$ transitions of the $^2F_{7/2}$ state at a transition frequency of 3.62 GHz and with a Ramsey dark time of 800 ms. Additionally, Rabi-controlled Ramsey spectroscopy of the E3 transition ensures the correct laser frequency for efficient population of the excited clock state.

which is independent of the magnetic field in first order, is measured as

$$\frac{\nu_{|+\rangle} + \nu_{|-\rangle}}{2} = 3\,620\,527\,303.869(1) \text{ Hz.}$$

Systematic corrections and the systematic uncertainty are still under investigation and the obtained hyperfine splitting frequency can be confirmed with measurements involving other magnetic sublevels. It should be noted that external perturbations affect the microwave transition differently compared to the electric octupole transition. For instance, the electric quadrupole shift as defined in equation (2.35) is proportional to a prefactor α that contains the coupling terms of the Hamiltonian for the respective transition. For the E3 transition, $\alpha_{E3} = 5/7$. Different shift strengths are calculated for transitions within the hyperfine sublevels, such as:

$$\begin{aligned} \alpha(|F = 3, m_F = 0\rangle \rightarrow |F = 4, m_F = 0\rangle) &= 0, \\ \alpha(|F = 3, m_F = 0\rangle \rightarrow |F = 4, m_F = \pm 1\rangle) &= -3/28, \\ \alpha(|F = 3, m_F = \pm 3\rangle \rightarrow |F = 4, m_F = \pm 2\rangle) &= 33/28. \end{aligned}$$

The experiments performed demonstrate that different hyperfine sublevels of the $^2F_{7/2}$ manifold can be readily employed for precision spectroscopy using microwave radiation.

3.7 Yb3 measurements

Starting from the end of 2019, Yb3 has been regularly compared both with the E2 and E3 transition to Yb1 and opticlock. Due to the difficulties with Yb3 related to varying dc electric fields discussed in section 2.3.5, the following comparisons are considered preliminary and will be pursued more rigorously once the physics package has been replaced. The results presented here will be comprised of the following comparisons:

$$\begin{aligned} &\nu_{E3}(\text{Yb1}) - \nu_{E3}(\text{Yb3}), \\ &\nu_{E2}(\text{Yb1}) - \nu_{E2}(\text{Yb3}), \\ &\nu_{E2}(\text{Yb3}) - \nu_{E2}(\text{opticlock}), \\ &\nu_{E3}(\text{Yb3})/\nu_{E2}(\text{Yb3}). \end{aligned}$$

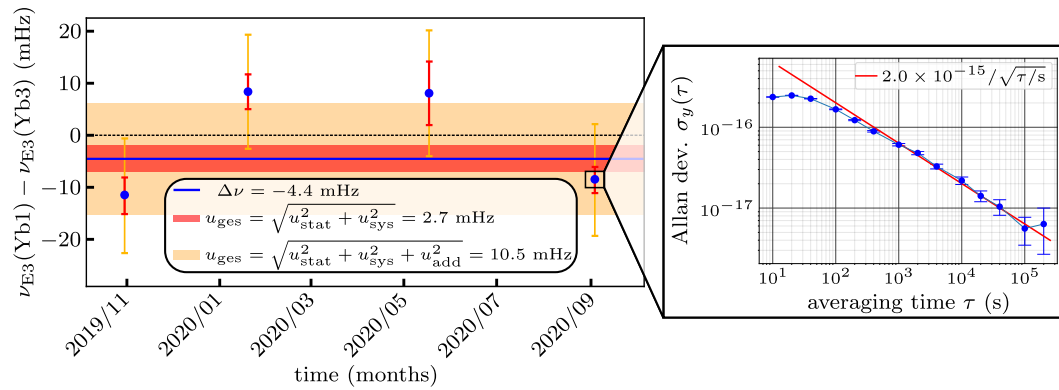


Figure 3.9: **Difference of the Yb1 and Yb3 E3 transition frequencies.** Measurements not further than 10 days apart are comprised into one data point, with red error bars showing the combined uncertainty. The blue line and the red shade area represent the mean value and its uncertainty. Due to the large scatter, an additional uncertainty contribution (orange) of 1.6×10^{-17} is added to yield $\chi_{\text{red}}^2 = 1$. The inset shows the relative frequency stability of the data in the last point.

Electric octupole frequency difference. A total of 480 hours of measurement have been acquired for the comparison of the E3 transition frequencies of Yb1 and Yb3. Continued measurements with gaps smaller than 10 days are compressed into a single data point, resulting in four points for figure 3.9. The combined systematic uncertainty of $u_{\text{sys}}/\nu_{E3} = 3.0 \times 10^{-18}$ arises from the quadrature of the individual systematic uncertainties provided in table 3.1 for

Yb1 and table 2.2 for Yb3, with the contribution of the atomic polarizability in the context of the blackbody radiation shift common-mode suppressed. In combination with the fractional statistical uncertainty $u_{\text{stat}}/\nu_{\text{E3}} = 3.0 \times 10^{-18}$, a frequency offset

$$\frac{\nu_{\text{E3}}(\text{Yb1}) - \nu_{\text{E3}}(\text{Yb3})}{\nu_{\text{E3}}} = -6.9(4.3) \times 10^{-18}$$

is found with a reduced chi-square value of $\chi_{\text{red}}^2 = 8.1$. All χ_{red}^2 values given in this section take into account both statistical and systematic uncertainty of the individual data points. Within a single measurement window, much less scatter is observed, as for example shown for the last point in figure 3.9, for which the individual data points yield $\chi_{\text{red}}^2 = 1.7$: The Allan deviation follows the expected $1/\sqrt{\tau}$ -property of white frequency noise to well below 10^{-17} . The 1 s frequency instability of 2.0×10^{-15} is slightly higher than for the Yb1(E3)-Yb2(E3) campaign discussed in section 3.2, where only the E3 transition was operated. Here, for both Yb1 and Yb3, the E2 and E3 transition are interrogated in interleaved clock operation. To account for the large scatter in figure 3.9, an additional uncertainty contribution $u_{\text{add}}/\nu_{\text{E3}} = 1.6 \times 10^{-17}$ has been added in quadrature that yields $\chi_{\text{red}}^2 = 1.0$ and leads to $u_{\text{ges}}/\nu_{\text{E3}} = 1.6 \times 10^{-17}$.

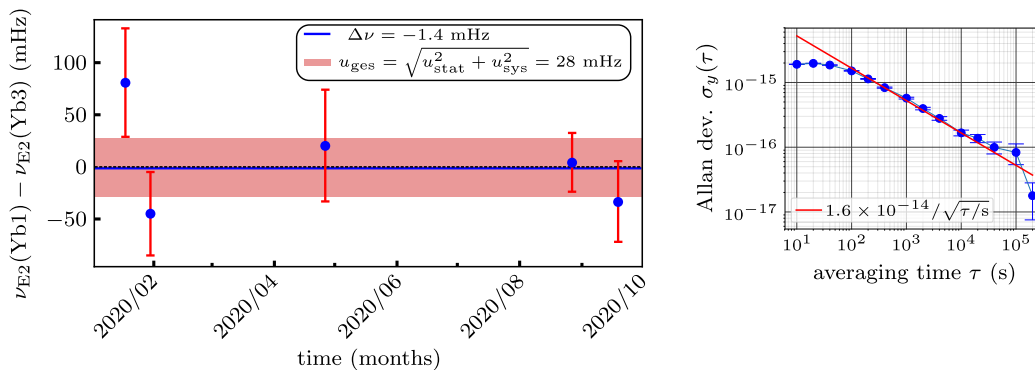


Figure 3.10: **Difference of the Yb1 and Yb3 E2 transition frequencies.** Measurements not further than 10 days apart are comprised into one data point, with red error bars showing the combined uncertainty. The blue line and the red shade area represent the mean value and its uncertainty. The stability of the full data set is shown on the right hand side.

Electric quadrupole frequency difference. In the same way as for the E3 transition frequency comparison, data has been acquired for a comparison of the E2 transition frequencies of Yb1 and Yb3: For the data shown in figure 3.10, individual measurements not further than 10 days apart have been compressed into a single data point. The mean value yields a relative frequency difference of

$$\frac{\nu_{\text{E2}}(\text{Yb1}) - \nu_{\text{E2}}(\text{Yb3})}{\nu_{\text{E2}}} = 0.2(4.1) \times 10^{-17}.$$

The fractional uncertainty is derived from the individual systematic uncertainties in table 3.4 for Yb1 and table 2.2 for Yb3, and a fractional statistical uncertainty of 2.5×10^{-17} . A reduced chi-squared $\chi_{\text{red}}^2 = 1.1$ is found. More than 270 hours of data have been acquired in total, for which the Allan deviation is shown on the right side of figure 3.10. Again, the instability of 1.6×10^{-14} at one second is limited due to the fact that interleaved clock operation is performed on the E3 and E2 transition, with most of the duty cycle reserved for probing of the E3 transition. For clock operation only on the E2 transition of Yb3 and with Yb1 referenced to the E3 transition frequency, typical instabilities observed are about 6×10^{-15} at one second, as shown in figure 3.11.

A comparison of the electric quadrupole transition has also been performed at the beginning of 2020 between Yb3 and opticlock. The data shown in figure 3.12 comprises more than 335 hours of measurement that yield $\chi_{\text{red}}^2 = 0.6$ and an instability of 1.0×10^{-14} at one second. With a combined fractional systematic uncertainty of 3.2×10^{-17} and a fractional statistical uncertainty of 0.9×10^{-17} , a relative frequency difference of

$$\frac{\nu_{\text{E2}}(\text{Yb3}) - \nu_{\text{E2}}(\text{opticlock})}{\nu_{\text{E2}}} = -3.5(3.3) \times 10^{-17}$$

is derived.

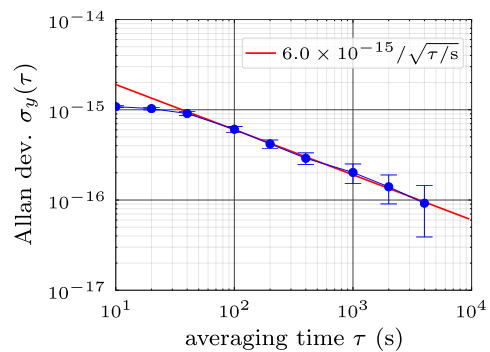


Figure 3.11: **Relative stability of the Yb3 E2 against the Yb1 E3 transition frequency.**

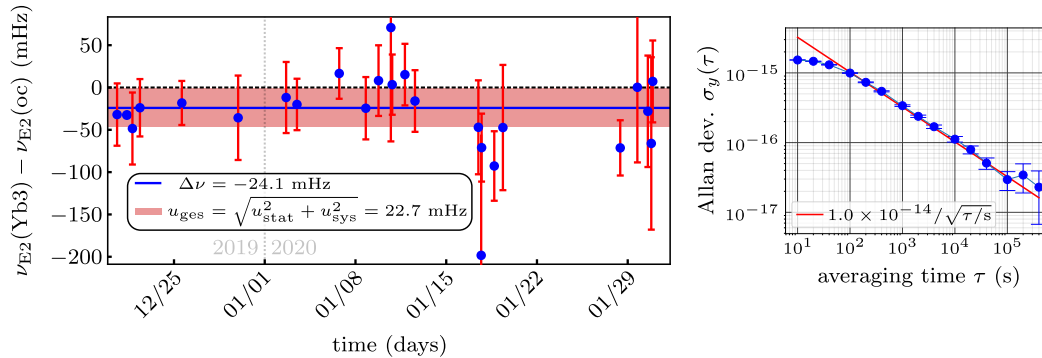


Figure 3.12: **Difference of the Yb3 and optclock (oc) E2 transition frequencies.** Red error bars show the combined uncertainty. The blue line and the red shade area represent the mean value and its uncertainty. The relative stability of the full data set is shown on the right hand side.

Transition frequency ratio. From interleaved measurements of the E3 and E2 transition frequencies, their ratio can be evaluated directly with the Yb3 system. A total of more than 600 hours of data with an instability of 1.2×10^{-14} at one second yields a ratio of

$$R_{E3,E2}(\text{Yb3}) = \frac{\nu_{E3}(\text{Yb3})}{\nu_{E2}(\text{Yb3})} = 0.932\,829\,404\,530\,965\,399(27).$$

The fractional uncertainty of 2.8×10^{-17} is dominated by the systematic uncertainty of the E2 transition. The relative statistical uncertainty yields $u_{\text{stat}}/R_{E3,E2}(\text{Yb3}) = 1.0 \times 10^{-17}$. The value agrees well with the frequency ratio found employing the E2 transition in Yb1 as discussed in section 3.3. As before, the data points shown in figure 3.13 are combined results of measurements with gaps smaller than 10 days, and one finds $\chi_{\text{red}}^2 = 0.4$. Taking all individual measurements instead yields $\chi_{\text{red}}^2 = 0.9$.

To conclude, first results of clock operation with the new single-ion frequency standard Yb3 have been presented. A comparison of the E3 transition of Yb1 and Yb3 shows that below a fractional uncertainty of 10^{-17} , scattering of the data becomes visible that is expected to be resolved once the variations in the dc electric fields have been suppressed. Then, more rigorous tests to lower the contributions to the systematic uncertainty, for example with respect to the rf second-order Zeeman shift, can be performed. For the comparison of the E2 transitions, the preliminary data shows agreements of Yb3 with both

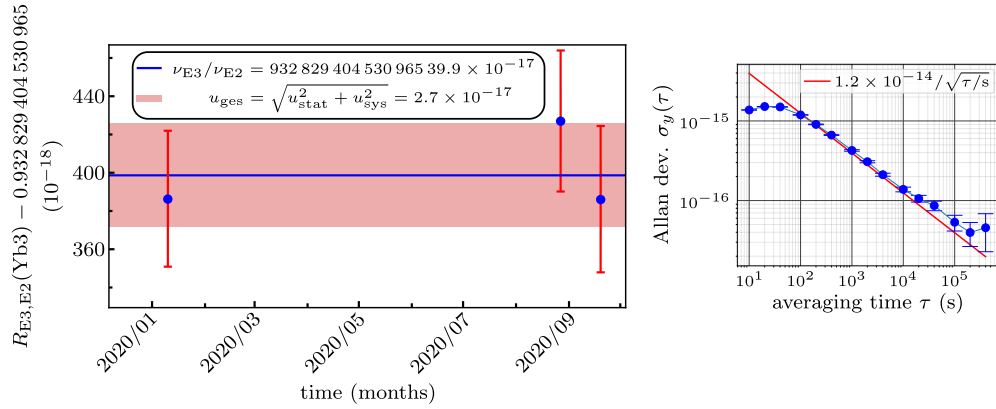


Figure 3.13: **Ratio of the Yb3 E3 and E2 transition frequencies.** Measurements not further than 10 days apart are comprised into one data point, with red error bars showing the combined uncertainty. The blue line and the red shade area represent the mean value and its uncertainty. The relative stability of the full data set is shown on the right hand side.

Yb1 and opticlock, and the frequency ratio of the E3 and E2 transition frequencies measured in an interleaved operation of the two clock transitions in Yb3 is compatible with the value found in section 3.3.

Chapter 4

Advanced interrogation methods

To reduce the systematic uncertainty of atomic clocks, methods for the control, suppression and evaluation of frequency shifts are devised. To improve the clock stability, interrogation schemes are geared towards long interaction times between atom and local oscillator. Such long interaction times dominate the overall clock cycle while the temporal overhead for state preparation and read-out is kept small. In this chapter, two methods designed for the reduction of specific uncertainty contributions are discussed: a coherent suppression technique for tensorial frequency shifts, and a Ramsey-type interrogation scheme immune to aberrations of the Ramsey pulses and the associated frequency shifts. Furthermore, a zero-crossing point of the scalar differential polarizability of the E3 transition, also known as the magic wavelength, is measured. This constitutes the first step towards interrogation methods employing sympathetic cooling for extended Ramsey dark times in a dual-species clock.

Due to its small oscillator strength, excitation of the E3 transition is accompanied by a significant light shift that needs to be well controlled. To further investigate the atomic properties of the E3 transition, a relation between light shift and transition rate is obtained. This is used in combination with the differential polarizabilities at the E3 transition wavelength to calculate the lifetime of the $^2F_{7/2}$ state with high accuracy. The light shift can be largely suppressed employing twisted light, i.e. placing the ion in the dark center of a Laguerre-Gaussian beam that features orbital angular momentum. Excitation of an E3 transition with such a beam is demonstrated for the first time at the end of this chapter.

4.1 Magnetic field rotation for coherent suppression of tensor frequency shifts

Shift effects that have a tensorial character, with symmetry properties of the second-degree spherical harmonics $Y_2^0(\theta) \propto (3 \cos^2 \theta - 1)$, can be typically suppressed by averaging the frequencies measured for three orthogonal orientations of the ion quantization axis, defined by an externally applied magnetic field [82]. An example has been given by the electric quadrupole shift (EQS) in section 2.3.8: An electric field gradient A coupling to the quadrupole moment Θ of an atomic state results in an energy shift of that state. Since the ground state of the clock transitions in Yb^+ does not possess a quadrupole moment, the frequency shift depends on the quadrupole moment of the excited state as well as the angle θ between magnetic field vector \mathbf{B} and z axis of the trap:

$$\Delta\nu_{\text{EQS}} = \nu_{\text{quad}}(3 \cos^2 \theta - 1) \propto A\Theta(3 \cos^2 \theta - 1). \quad (4.1)$$

The orientation-independent shift is given by ν_{quad} . The formula presented here is a simplification of equation (2.35) given in section 2.3.8, with the assumptions of a field gradient between the dc endcap electrodes and a trap with cylindrical symmetry around the z axis. It should be noted that the method described is valid for the general expression of the EQS, but for the discussion here, the shift is well approximated by the simplified expression.

Averaging the frequencies measured for three mutually orthogonal orientations of the magnetic field vector is performed during clock operation on the E2 transition. Since the tensorial part of the quadratic Stark shift features the same symmetry properties (section 2.3.1), implementation of this method for the E3 clock would lead to large variations of the light shift for the different orientations, degrading clock performance. Therefore, clock operation on the E3 transition is performed with a fixed orientation. The EQS of the E3 transition frequency is corrected based on the EQS of the E2 transition and the ratio of the quadrupole moments $\Theta(^2\text{D}_{3/2})/\Theta(^2\text{F}_{7/2})$, as derived in section 2.3.8. This approach requires interleaved clock operation of the E2 and E3 transition, thereby reducing the duty cycle of the E3 clock. In order to enhance the E3 clock stability and to achieve independence from the E2 transi-

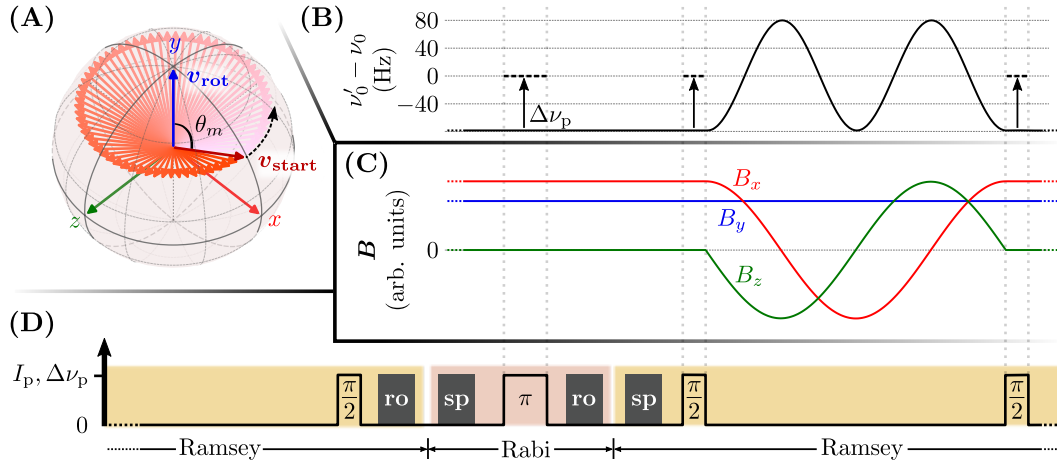


Figure 4.1: **Visualization of the coherent suppression scheme.** (A) Rotation of the magnetic field around \mathbf{v}_{rot} , here along the y axis, at the magic angle θ_m . (B) Deviation of the instantaneous atomic resonance frequency ν'_0 from the unperturbed transition frequency ν_0 due to an electric field gradient. For the full rotation that is performed during the dark time of a Ramsey sequence, the shift averages to zero. The shift present during the Ramsey pulses is measured from interleaved Rabi excitations and corrected by applying an auxiliary frequency offset $\Delta\nu_p$. (C) Variation of the magnetic field components along the principal axes during the sequence. (D) Rabi-controlled Ramsey cycle, with clock laser intensity I_p and offset $\Delta\nu_p$ from ν_0 during the pulses, as well as readout (ro) and state preparation (sp) conducted in between interrogations. The figure is adapted from [65].

tion, a different approach is presented here, relying on the coherent suppression of the EQS during the dark time of the Ramsey interval. This method and its demonstration are shown in the following and have been published in [65].

Inspired by a technique called magic angle spinning, commonly employed in nuclear magnetic resonance spectroscopy [145], a 2π rotation of the magnetic field vector is performed during the Ramsey dark time of the clock cycle. The field is rotated at constant speed around a vector \mathbf{v}_{rot} at the magic angle θ_m with $\cos^2 \theta_m = 1/3$, as shown in figure 4.1 (A). This scheme can be seen as a coherent version of the method of averaging over three orthogonal orientations of the magnetic field vector [82]: For each position of the vector moving with constant speed on the trajectory, two mutually orthogonal vectors at different positions on the same trajectory can be found. While for the incoherent averaging scheme three independent clock cycles are needed for the suppression, the coherent scheme facilitates a suppression during the free atomic evolution time of a single cycle.

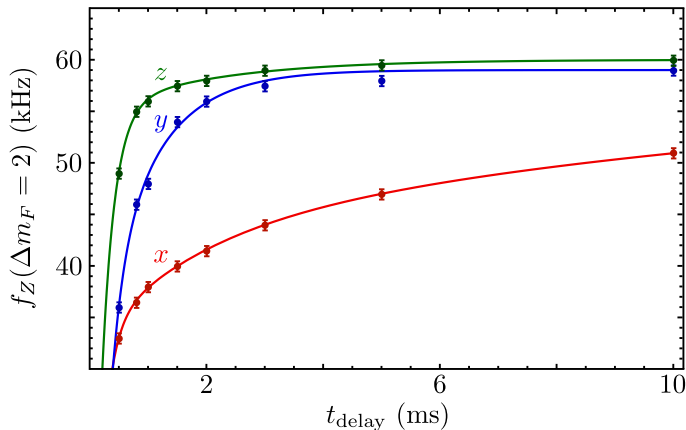


Figure 4.2: **Delay of the magnetic field along the principal axes, measured on the $|m_F = 0\rangle \rightarrow |m_F = 2\rangle$ Zeeman sublevels of the E2 transition.** The magnetic field is oriented along each of the three main axes independently (x - red, y - blue, z - green), with a strength that yields a Zeeman splitting frequency $f_Z(\Delta m_F = 2) = 60$ kHz. At $t_{\text{delay}} = 0$ ms the currents are reversed to provide the same magnetic field along the opposite direction, and the field response at the position of the ion is measured from the Zeeman splitting. A linear combination of exponential functions is fitted to the data.

The vector \mathbf{v}_{rot} and thus the starting magnetic field vector $\mathbf{v}_{\text{start}}$ employed during the Ramsey pulses can be chosen freely, i.e. with maximum excitation probability for the E3 transition. In figure 4.1, $\mathbf{v}_{\text{rot}} \parallel \mathbf{e}_y$ has been chosen as an example. Using a Rabi-controlled Ramsey scheme, the EQS during the Ramsey pulses is monitored with an additional Rabi sequence and corrected by a second servo loop, fully analogous to the light shift suppression with Rabi-controlled Ramsey spectroscopy explained in section 1.4.6.

For the experimental realization of the coherent suppression scheme, deviations of the magnetic field vector from the ideal trajectory due to delayed magnetization and eddy-current effects need to be taken into account. The magnetic field response can be assessed by applying a step function to the current driver control input, for each of the three coil sets along one of the principle axes x , y , z . The magnetic field at the ion position is inferred from the Zeeman splitting frequency f_Z after a variable delay t . The field delay is modeled by a linear combination of exponential functions,

$$f_Z(t) = (f_{\text{start}} - f_{\text{end}})(A_1 e^{-(t-\tilde{t})/\tau_1} + A_2 e^{-(t-\tilde{t})/\tau_2}) + f_{\text{end}}, \quad (4.2)$$

with $A_1 + A_2 = 1$ and the equilibrium Zeeman splitting frequencies f_{start} and f_{end} before and after the step. From the measured field delay shown in figure 4.2, time constants τ_1 and τ_2 of about 0.2 ms and 1.0 ms can be found. For the x axis, a third term with $\tau_3 = 16$ ms has been fitted to the data. The response time \tilde{t} is on the order of 0.1 ms, it describes the delay between setting the step function in the experimental routine and actual change of the coil currents.

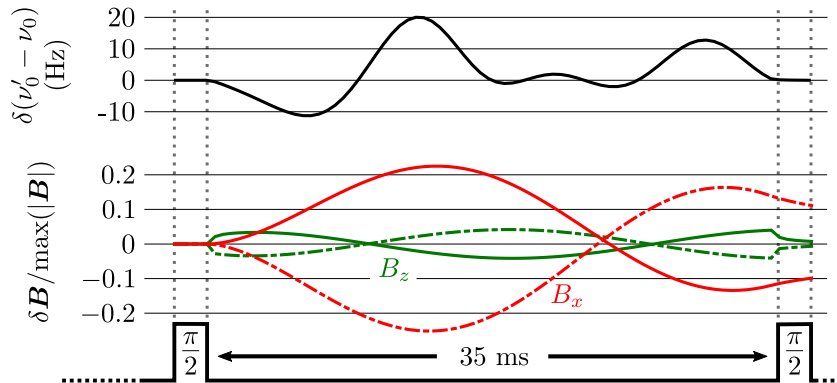


Figure 4.3: **Distortions due to the magnetic field delay** for the instantaneous atomic transition frequency (black line) and two of the magnetic field components (solid red and green line). This simulation is performed for the example shown in figure 4.1 and using the measured magnetic field delay presented in figure 4.2. The dashed red and green line show the magnetic field compensations that need to be applied to retrieve the unperturbed trajectories. The figure is adapted from [65].

The field delay model in equation (4.2) is employed to simulate the expected deviations from the ideal magnetic field trajectories and to compute compensating trajectories, both depicted in figure 4.3 for rotation around the y axis. The corresponding frequency deviation is calculated and plotted as well.

The E3 transition is an ideal candidate for the application of the coherent suppression scheme, as it facilitates long Ramsey dark times and suffers from large light shifts not permitting the incoherent averaging method. However, for demonstration of the technique, the E2 transition is better suited since the EQS is almost two orders of magnitude larger and uncompensated frequency deviations are easier resolved. A Ramsey dark time of 35 ms and a π pulse time of 5 ms are chosen. A voltage $U = -60.0(3)$ V applied to the endcap electrodes of the trap induces a large electric field gradient and leads to the orientation-independent shift $\nu_{\text{quad}} = 78.7(2)$ Hz, the same operating conditions as in

section 2.3.8. Three different rotation vectors \mathbf{v}_{rot} are chosen, one along each of the principal axes. The E3 transition of Yb1 provides a stable frequency reference. First, the rotation scheme is employed without compensating for the magnetic field delay, yielding $\Delta\nu^{\text{exp}}$ in table 4.1. The expected frequency shifts $\Delta\nu^{\text{sim}}$ due to the field delay can be simulated with knowledge of orientation and strength of the EQS, and the difference $\Delta\nu^{\text{exp}} - \Delta\nu^{\text{sim}}$ is a measure for the validity of the field delay model. Finally, compensating trajectories are computed and employed during the coherent rotation, yielding the frequency shifts $\Delta\nu_{\text{comp}}^{\text{exp}}$ in the last column of table 4.1. For all three rotation axes, the tensorial shift is largely suppressed. From the largest deviation -0.3 Hz and the mean EQS $\nu_{\text{quad}} = 78.7(2)$ Hz, a minimum suppression factor of 260 is derived.

\mathbf{v}_{rot}	$\Delta\nu^{\text{exp}}$	$\Delta\nu^{\text{sim}}$	$\Delta\nu^{\text{exp}} - \Delta\nu^{\text{sim}}$	$\Delta\nu_{\text{comp}}^{\text{exp}}$
\mathbf{e}_x	$-0.51(4)$	$-0.46(10)$	$-0.05(11)$	$-0.30(8)$
\mathbf{e}_y	$2.50(4)$	$2.67(25)$	$-0.17(25)$	$-0.05(9)$
\mathbf{e}_z	$8.07(3)$	$7.74(30)$	$0.33(30)$	$0.00(7)$

Table 4.1: **Frequency deviation from the unperturbed transition frequency employing the coherent suppression scheme** for rotation around the three main axes and with an externally applied electric field gradient. Experimentally, $\Delta\nu^{\text{exp}}$ are found if the magnetic field delay is not compensated, with statistical uncertainties given. The expected offsets $\Delta\nu^{\text{sim}}$ due to the field delay, extracted from simulations and with uncertainties obtained from a Monte Carlo method, are compared with the experimental values. Employing the compensated magnetic field trajectories, the frequency deviations $\Delta\nu_{\text{comp}}^{\text{exp}}$ are found (with statistical uncertainties). All values are given in Hz.

Using the EQS ratio $\Delta\nu_{\text{E2}}/\Delta\nu_{\text{E3}} = -92.1(1.7)$ from section 2.3.8, and a typical electric field gradient of less than 1 V/mm² resulting in $\nu_{\text{quad}} = 1$ Hz on the E2 transition, a residual shift of less than 0.04 mHz on the E3 transition is expected when employing the coherent rotation scheme. The corresponding relative uncertainty of the E3 clock is about 6×10^{-20} . It should be noted that the Ramsey dark time for the E3 clock of more than 300 ms is an order of magnitude larger than in this experimental demonstration on the E2 transition, which yields a slower rotation and thereby less field-delay-induced distortion of the trajectory. This is expected to reduce the uncertainty even further.

4.2 Autobalanced Ramsey spectroscopy

Ramsey's method of separated oscillatory fields [60, 61] enables the comparison of a local oscillator phase ϕ_L to the unperturbed atomic transition phase ϕ_0 during the free evolution period in between Ramsey pulses. The outcome of this measurement is used to steer the local oscillator frequency ω_L towards the unperturbed atomic transition frequency ω_0 in a servo loop. If a significant perturbation is present during the Ramsey pulses such as the light shift in the case of the E3 transition, a shifted local oscillator frequency $\omega_{L,\text{drive}}$ is required to resonantly drive the transition. However, deviations of $\omega_{L,\text{drive}}$ from the light shifted transition frequency may occur due to phase or frequency chirps and other perturbations, resulting in a clock error, i.e. an offset of ω_L from ω_0 . These effects can be suppressed, as shown in the following.

Two Ramsey sequences are employed that suffer from the same perturbations during the pulses but have different Ramsey dark times T_{short} and T_{long} , i.e. the two sequences are isomorphic. Their differential signal can be used to obtain immunity to the pulse defects, as shifts are common-mode suppressed: During clock operation, the differential error signal¹ will be zero if $\omega_L = \omega_0$,

$$\Delta p_{\text{diff}} = \Delta p_{\text{short}} - \Delta p_{\text{long}} = 0. \quad (4.3)$$

However, an error in the stabilization of the laser to the atomic reference may still occur, since Δp_{diff} may not be symmetric around $\omega_L = \omega_0$ while $\Delta p_{\text{short}} = \Delta p_{\text{long}} = 0$ is not enforced. The individual error signals Δp_{short} and Δp_{long} can be nonzero at $\omega_L = \omega_0$ due to defects of the Ramsey pulses. To avoid a clock error due to an asymmetric differential error signal, $\Delta p_{\text{short}} = 0$ needs to be ensured. This is achieved by correcting for deviations of $\omega_{L,\text{drive}}$ from the resonant drive frequency in an independent servo loop.

Relying on these insights, autobalanced Ramsey spectroscopy (ABRS) is based on interleaved operation of the two employed Ramsey sequences [66]. The principle of this method is shown in figure 4.4, with a frequency offset from the light-shifted atomic transition frequency ω'_0 as an example for the

¹The error signal Δp has been introduced in section 1.4.6. It is obtained from the difference in the excitation probabilities when probing the atomic transition slightly red and blue detuned from the local oscillator frequency.

probe pulse defect. This leads to a constantly increasing deviation of ϕ_L from ϕ_0 during the pulse. The short sequence with T_{short} is used to obtain a phase step ϕ^c , correcting for this defect in a servo loop and ensuring $\Delta p_{\text{short}} = 0$. The phase step is applied in all Ramsey cycles (short and long) together with a phase increment or decrement $\phi^\pm = \pm\pi/2$ used to generate the error signal. It should be noted that instead of the phase step ϕ^c , a detuning of the drive frequency $\omega_{L,\text{drive}}$ can be implemented as well. In the long sequence, the interrogation is more sensitive to a frequency offset during the free evolution time. The spectroscopic signal Δp_{long} is evaluated to feed a second servo that steers the local oscillator frequency ω_L towards the atomic transition frequency ω_0 .

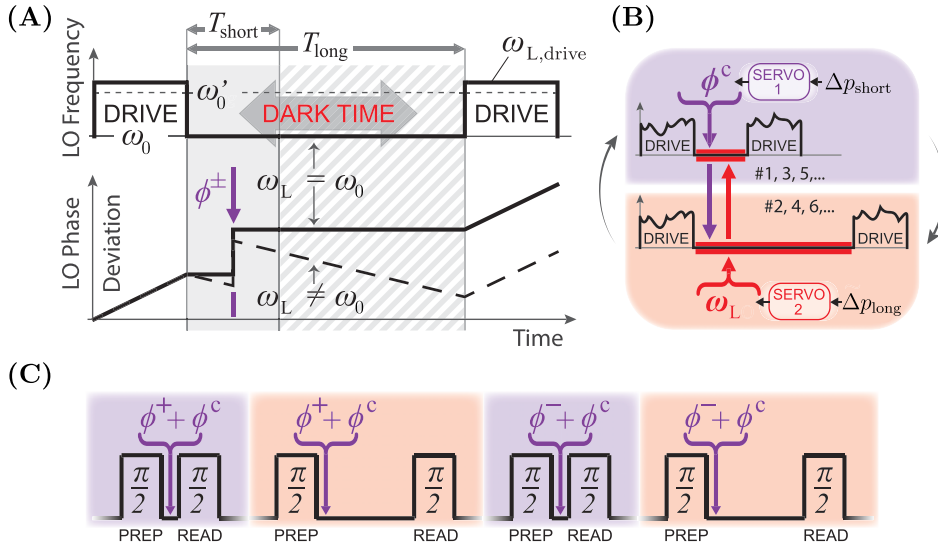


Figure 4.4: **Sequence of the autobalanced Ramsey scheme.** (A) Two Ramsey interrogations with dark times T_{short} and T_{long} are performed. The local oscillator frequency $\omega_{L,\text{drive}}$ during the pulses slightly deviates from the light-shifted atomic resonance frequency ω_0' , leading to a phase offset between the two frequencies. If local oscillator and unperturbed transition frequency are equal during the dark time, $\omega_L = \omega_0$ (solid line), the outcome of short and long Ramsey experiment are equal. A frequency offset leads to a phase deviation (dashed line). A phase modulation $\phi^\pm = \pm\pi/2$ is used to generate the discriminator signal. (B) The spectroscopic signal obtained from the short sequence Δp_{short} is used to steer a phase offset ϕ^c applied during both long and short Ramsey dark time. The signal Δp_{long} obtained during the long sequence is used to steer ω_L during the dark time. The two sequences may be distorted (as indicated by the ragged pulses) but need to be identical apart from the different dark times. (C) Short and long sequence are applied alternately, as well as the phase steps ϕ^+ and ϕ^- . The figure is adapted from [66].

To demonstrate the universal immunity to defective pulse sequences, experiments are performed with an intensity defect, a phase excursion and a phase lag. For standard Ramsey spectroscopy, shifts of the clock frequency are found that are corrected employing ABRS. The results are presented in figure 4.5 and have been published in [66].

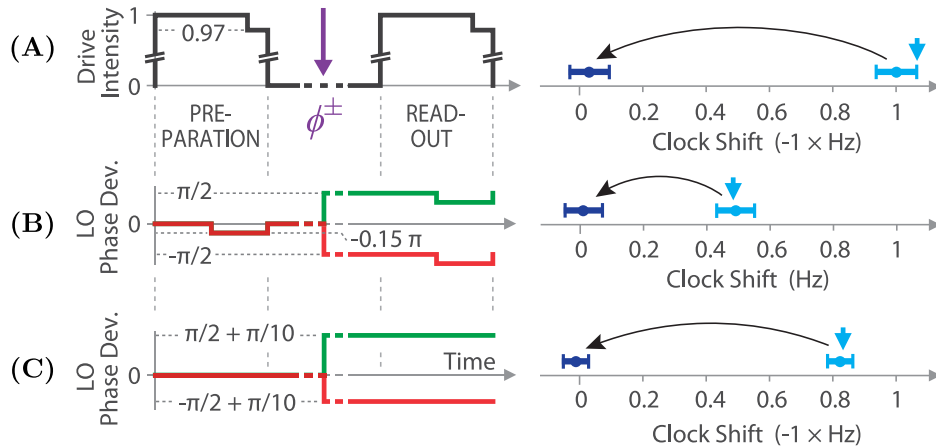


Figure 4.5: **Experimental demonstration of the autobalanced Ramsey scheme** for different perturbations: (A) intensity defect, (B) phase excursion, and (C) phase lag. The standard Ramsey scheme leads to deviations depicted by the light blue data points, with theoretically predicted shifts indicated by the arrows. Employing autobalanced Ramsey spectroscopy (dark blue data points), the shifts are eliminated. For the phase deviation experiments, the traces for both phase steps ϕ^+ (green) and ϕ^- (red) are shown. The figure is adapted from [66].

The requirement of isomorphic short and long Ramsey sequence is not entirely met for the Yb2 setup in which the experiments are carried out. The trap exhibits a large heating rate of about 300 quanta of motion per second, reducing the effective Rabi frequency for the Ramsey pulse after T_{long} . For compensation, an EOM has been installed that produces off-resonant sidebands at $\omega_{\text{EOM}} = 2\pi \times 2$ GHz and reduces the carrier frequency strength for the second pulse of T_{short} accordingly.

ABRS can be regarded as an incoherent method related to hyper-Ramsey spectroscopy (HRS): With an additional π -pulse added to the standard Ramsey sequence, light shifts are suppressed in HRS within a single, phase-coherent interrogation cycle, while ABRS uses the combined output of two independent cycles. With respect to the clock stability, ABRS seems to be the inferior method as quantum projection noise is observed in both interrogation cycles.

Due to phase noise on ϕ^c carried over in the long interrogation cycle, fluctuations of ω_L are expected to be a factor of $\sqrt{2}$ larger than without the feedback from the ϕ^c -servo. However, the stability reduction is traded against an increase in the Ramsey dark time, as the additional π -pulse of HRS is removed. The Rabi pulse needed to control the light shift in HRS (Rabi-controlled hyper-Ramsey spectroscopy) is of similar time span as the short Ramsey sequence in ABRS. Depending on the specific experimental parameters, ABRS can be comparable to HRS or even advantageous in terms of clock stability.

4.3 Towards light shift-suppressed sympathetic cooling: Magic wavelength measurement

Parallel to the work on the single-ion clock experiments, a dual-species clock experiment is set up for simultaneous investigation of $^{171}\text{Yb}^+$ and $^{88}\text{Sr}^+$ in a linear ion trap. It will be used for the investigation of the static scalar differential polarizability, as described in section 2.3.2. Here, another potential advantage of a co-trapped $^{88}\text{Sr}^+$ ion is sketched.

Measurements of the scalar differential polarizability $\Delta\alpha_S$ of the E3 transition of Yb^+ at different wavelength indicate a zero-crossing point and thereby a magic wavelength around 680 nm [33]. This is of particular interest for sympathetic cooling of Yb^+ with Sr^+ , as the $^2\text{S}_{1/2} \rightarrow ^2\text{D}_{5/2}$ electric quadrupole transition in $^{88}\text{Sr}^+$ at 674 nm [146] could in principle allow for sideband cooling of the Sr^+ ion without introducing a light shift of the E3 transition frequency during clock operation on the Yb^+ ion. In this case, the coherent interrogation would not be limited by the motional heating of the ion, facilitating very long dark times and an improved clock stability. As a first step towards this approach, the magic wavelength of the E3 transition has to be determined. The corresponding experiment will be explained in the following.

The interaction of an atom with an electric field \mathbf{E} has been described in section 2.3.1. From equation (2.2), one finds the expression of the quadratic Stark shift for the E3 transition, also known as light shift:

$$\Delta\nu_{\text{LS}} = -\frac{1}{h}|\mathbf{E}|^2 \left[\frac{\Delta\alpha_S(\lambda)}{2} + \frac{4}{5} \frac{\Delta\alpha_T(\lambda)}{4} (3 \cos^2 \beta - 1) \right]. \quad (4.4)$$

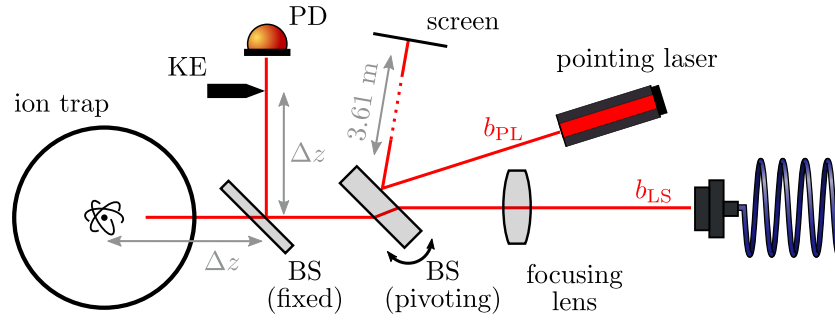


Figure 4.6: **Measurement of the differential polarizability** by exposing the ion to light from laser beams b_{LS} of different wavelengths. In order to measure the beam profile at the ion position, the beam is shifted by varying the angle of a glass plate called a beam sampler (BS). The angle can be measured accurately on a distant screen using a pointing laser beam b_{PL} . To calibrate the relation between pointing laser spot on the screen and beam displacement at the ion position, a knife-edge (KE) measurement is performed using a photodiode (PD). The beam b_{LS} propagates an equal distance Δz to ion trap center and knife-edge.

The wavelength-dependent scalar and tensorial differential polarizabilities are given by $\Delta\alpha_S(\lambda)$ and $\Delta\alpha_T(\lambda)$, respectively, and β is the angle between the ion quantization axis defined by an external magnetic field and the electric field vector. To determine both components of the polarizability, the ion is exposed to laser light of different wavelengths and at different magnetic field orientations. The quadratic Stark shift depends on the intensity of the light,

$$I = \frac{1}{2}c\epsilon_0|\mathbf{E}|^2, \quad (4.5)$$

with c the speed of light and ϵ_0 the vacuum permittivity. The intensity can be deduced from the beam profile and the laser power at the ion position.

The beam profile is measured with the experimental setup shown in figure 4.6. Light inducing the quadratic Stark shift is coupled out of a fiber and focused to the position of the ion. This is referred to as beam b_{LS} in the following. A beam sampler, a glass plate of 5 mm thickness, displaces the beam after the focusing lens depending on the angle between beam and plate. A pointing laser beam b_{PL} reflected from the beam sampler surface is focused on a screen in a distance of 3.61(1) m to measure a change of the beam sampler angle using a long lever arm.

In order to calibrate the dependence of the b_{LS} displacement at the ion position on the b_{PL} displacement at the screen, a second beam sampler directs a small fraction of b_{LS} onto a photodiode. A sharp blade is installed at the focus in front as shown in figure 4.6, at the same distance from the beam sampler as the ion in the trap. The beam position is deduced from a knife-edge measurement: The blade is moved either horizontally or vertically through the beam and the transmitted power is detected by a photodiode, as presented in figure 4.7 (A). The data is fitted using an error function erf,

$$P(x) = P_0 + \frac{P_{\text{max}}}{2} \left[1 - \operatorname{erf} \left(\frac{\sqrt{2}(x - x_0)}{w_0} \right) \right], \quad (4.6)$$

with P_0 the background and P_{max} the maximum power, x_0 the beam center and w_0 the Gaussian beam waist. Performing this measurement for several displacements, the following dependence on the beam sampler angle is found: A displacement of b_{PL} on the screen Δx_{screen} translates to a displacement of b_{LS} at the ion position Δx_{ion} with

$$\begin{aligned} \Delta x_{\text{ion}} / \Delta x_{\text{screen}} &= 0.955(8) \text{ } \mu\text{m/mm}, \\ \Delta y_{\text{ion}} / \Delta y_{\text{screen}} &= 0.550(4) \text{ } \mu\text{m/mm} \end{aligned}$$

for x the horizontal and y the vertical direction. These values are confirmed in theoretical calculations for angles between b_{LS} and glass plate of $\theta_x \approx 50^\circ$ and $\theta_y \approx 25^\circ$.

In the next step, the intensity profile at the ion position is mapped by observing the light shift for several beam displacements as depicted in figure 4.7 (B). From a fit to a Gaussian beam profile taking into account astigmatism, i.e. different beam waists for x and y , and with knowledge of the total laser power, the intensity I at the beam center is deduced, to which the ion is exposed. From measurements of the power before and after the vacuum chamber, a loss of 0.7(1) % due to the windows at Brewster's angle is inferred.

For four different wavelengths of the laser, the light shift of the E3 transition frequency has been measured, each with different magnetic field orientations. All light shift measurements are performed with interleaved clock operation,

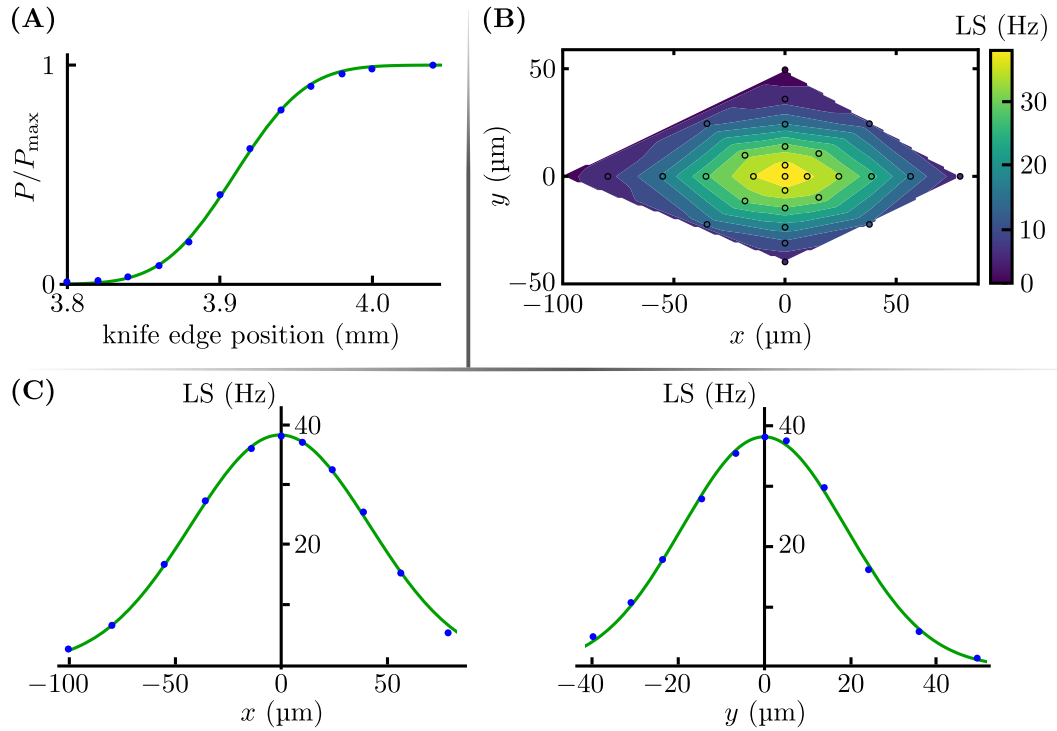


Figure 4.7: **Measurement of the beam profile.** (A) Detection of the power of the beam on a photodiode after a moving sharp blade (knife-edge measurement). (B) Beam profile at the position of the ion, measured by the light shift (LS) induced on the E3 transition frequency. (C) Horizontal and vertical cut through the beam profile shown in (B).

for which one servo steers the frequency without and one with the additional light shift introduced. The frequency difference is attributed to the light shift. The measurements are summarized in table 4.2. Figure 4.8 (A) shows one example of the dependence of the light shift on the magnetic field orientation, with a fit according to equation (4.4).

A linear fit of the scalar differential polarizabilities in figure 4.8 (B) yields a magic wavelength of $681.2(5)$ nm and a slope of $2.3(1) \times 10^{-43}$ $\text{Jm}^2\text{V}^{-2}/\text{nm}$. This converts to a sensitivity of about -0.2 $\mu\text{Hz}/\text{MHz}/(\text{Wmm}^{-2})$, i.e. an error of 1 MHz in the magic wavelength at an intensity of 1 Wmm^{-2} will result in a clock frequency shift of -0.2 μHz . To put this number into context, it is compared to the corresponding value for a lattice clock: For ^{87}Sr , the lattice light is provided by a laser at 813 nm wavelength with a sensitivity of about -34 $\mu\text{Hz}/\text{MHz}/(\text{Wmm}^{-2})$ [147].

When performing sideband cooling of Sr^+ during clock operation of Yb^+ ,

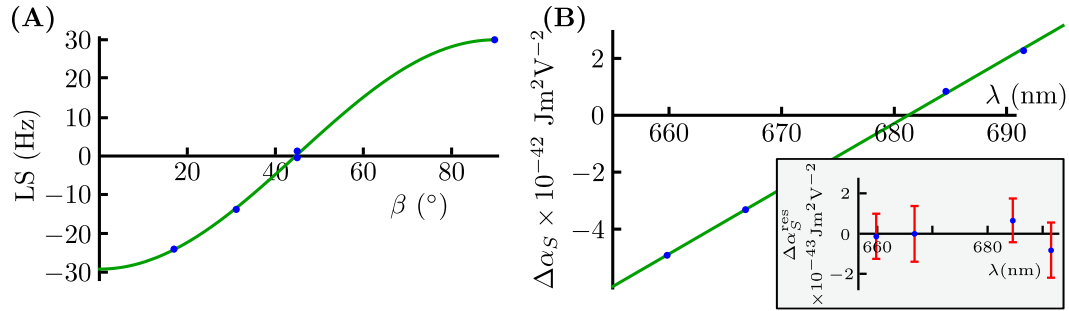


Figure 4.8: **Differential polarizability on the E3 transition at different wavelengths.** (A) The tensorial differential polarizability depends on the angle β between ion quantization axis and laser beam polarization, leading to a variation of the measured light shift (LS) on the E3 transition frequency, here shown for a wavelength of 666.8 nm. There is a contribution of about 10 Hz to the light shift due to the scalar differential polarizability. (B) Scalar differential polarizability in dependence of the wavelength of the light shifting laser, with a zero crossing at 681.2(5) nm. The inset shows the residuals and uncertainties of the data points.

meas.	wavelength (nm)	I (W/mm ²)	$\Delta\alpha_S$ (10 ⁻⁴² Jm ² V ⁻²)	$\Delta\alpha_T$ (10 ⁻⁴¹ Jm ² V ⁻²)
1	659.8(1)	6.1(1)	-4.9(1)	1.51(3)
2	666.8(1)	5.45(3)	-3.3(2)	1.59(3)
3	684.6(1)	2.58(4)	0.8(1)	1.51(4)
4	691.5(1)	2.38(6)	2.3(2)	1.52(5)

Table 4.2: **Scalar and tensorial differential polarizabilities** $\Delta\alpha_S$ and $\Delta\alpha_T$ at different light shift laser wavelengths, in combination with the laser intensity at the ion position I .

the laser light at about 674 nm is not at the magic wavelength. However, the light shift can be tuned by simultaneously introducing light at 1033 nm, which pumps the atom back into the ground state after successful excitation of the clock state [148]. Laser light at 1092 nm, typically employed to repump the $D_{3/2}$ state during Doppler cooling, can be used for further tuning: With a suitable choice of the intensities, the light shift due to the near-infrared beams cancels the light shift from the 674 nm laser. The tensorial contribution of the polarizability is suppressed by averaging the polarization using an electro-optic modulator. Residual light shifts can be eliminated efficiently by employing autobalanced Ramsey spectroscopy described in section 4.2 for clock operation of the Yb^+ ion, as shifts present during both short and long Ramsey pulse are common-mode suppressed.

4.4 E3 transition light shift and ${}^2F_{7/2}$ state lifetime

In order to drive the E3 transition, interrogation methods have to control or suppress the large light shift resulting from the high intensity of the probe laser. The high intensity is necessary due to the small oscillator strength of the transition, corresponding to an exceptionally small linewidth and a very long natural lifetime of the excited ${}^2F_{7/2}$ state. So far, theoretical estimates of the $\text{Yb}^+ {}^2F_{7/2}$ state natural lifetime range from about 2 [149] to more than 8 [150] years, and experimental investigations have uncertainties spanning more than ten years [74, 151]. Within this section, a precise measurement of the ${}^{171}\text{Yb}^+ {}^2F_{7/2}$ state natural lifetime is discussed, as can be found in [152].

Typically, the lifetime of a metastable excited atomic state is inferred experimentally from the spontaneous decay time of that state to the ground state. The fluorescence signal of an associated fast-cycling dipole-allowed transition may be used to determine if the ground-state decay has occurred. In single-ion experiments, lifetimes of up to a few tens of seconds have been measured using this method [70, 153–155]. It provides high accuracy, as demonstrated for the ${}^2D_{5/2}$ state lifetime in ${}^{40}\text{Ca}^+$ with $\tau = 1.1649(44)$ s [156]. For clouds of more than 10^6 neutral atoms trapped in a magnetic quadrupole field, the much larger signal-to-noise ratio allows for the assessment of longer lifetimes [157, 158]. For instance, the 2S_1 state lifetime in He has been measured as $\tau = 7870(510)$ s [159].

For the highly-forbidden Yb^+ E3 transition, the measurement of the spontaneous decay rate is not a suitable method. Alternatively, the natural lifetime can be deduced from excitation of the transition. In previous assessments [74, 151], the lifetime has been estimated from the excitation rate and the laser intensity at the ion position. Here, a relation between the excitation rate and the light shift of the transition is obtained to calculate the natural lifetime, as discussed in the following.

According to equation (4.4) given in the last section, the light shift of the E3 transition can be expressed by

$$\Delta\nu_{\text{LS}} = -\frac{E_0^2}{h} \left[\frac{\Delta\alpha_S}{2} + \frac{\Delta\alpha_T}{5}(3\cos^2\beta - 1) \right], \quad (4.7)$$

with E_0 the electric field amplitude and β the angle between electric field vector and the ion quantization axis defined by an externally applied magnetic field. The scalar and tensorial differential polarizabilities $\Delta\alpha_S$ and $\Delta\alpha_T$ for the E3 transition [160] have been obtained in an analogous manner to the assessment of the polarizabilities for the magic wavelength discussed in the last section:

$$\begin{aligned}\Delta\alpha_S(467 \text{ nm}) &= -2.67(11) \times 10^{-40} \text{ Jm}^2/\text{V}^2, \\ \Delta\alpha_T(467 \text{ nm}) &= 4.1(2) \times 10^{-41} \text{ Jm}^2/\text{V}^2.\end{aligned}$$

For a specific probe laser intensity, the light shift $\Delta\nu_{\text{LS}}$ can be measured with a frequency scan using Rabi excitation. Performing a Rabi-flopping experiment at the obtained resonant frequency, the Rabi frequency Ω can be deduced from equation (1.43), which yields

$$p_{\bar{n}}(t) = \frac{1}{2} \left(1 - \frac{\cos(\Omega t) + \Omega t \eta^2 \bar{n} \sin(\Omega t)}{1 + (\Omega t \eta^2 \bar{n})^2} \right). \quad (4.8)$$

These experiments are carried out at an angle $\beta = \beta_0 = 59^\circ$ between electric field vector and ion quantization axis, at which the maximum excitation probability of the E3 transition is obtained. Measuring light shift $\Delta\nu_{\text{LS}}$ and Rabi frequency Ω for different laser intensities as shown in figure 4.9 reveals a quadratic dependence, which can be expressed by

$$\Delta\nu_{\text{LS}} = \xi_{\text{LS}} \Omega^2, \quad (4.9)$$

with $\xi_{\text{LS}} = 0.033(1)/\text{Hz}$.

Furthermore, the Rabi frequency is given by equation (1.23):

$$\Omega = \frac{|M|E_0}{\hbar}, \quad (4.10)$$

with M the matrix element. Using equations (4.7) and (4.9), the absolute value of the matrix element can be expressed by

$$|M| = \frac{1}{2\pi} \sqrt{-\frac{h}{\xi_{\text{LS}}} \left[\frac{\Delta\alpha_S}{2} + \frac{\Delta\alpha_T}{5} (3 \cos^2 \beta_0 - 1) \right]}. \quad (4.11)$$

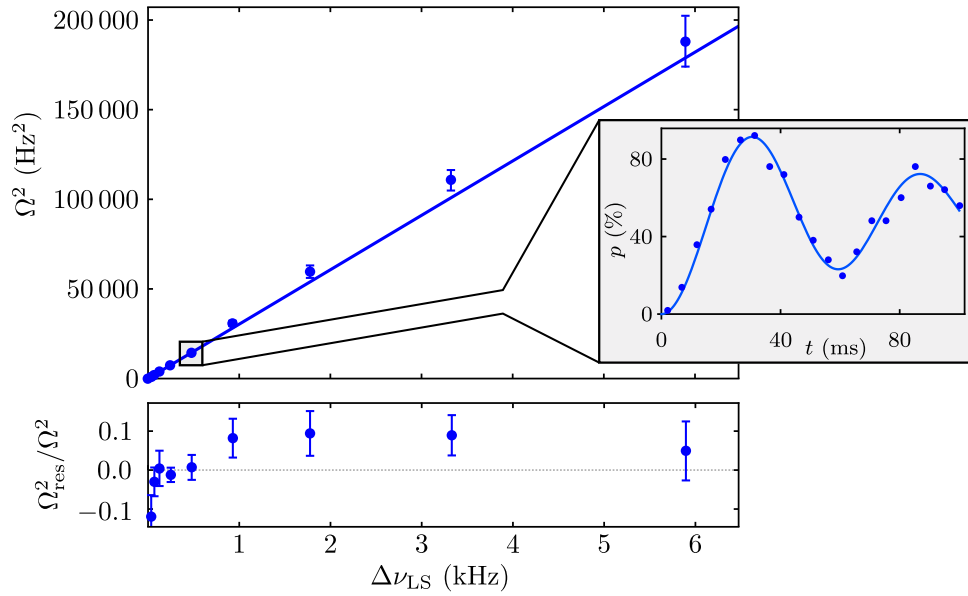


Figure 4.9: **Squared Rabi frequency Ω^2 versus light shift $\Delta\nu_{LS}$** of the E3 transition for different laser intensities at the ion position. The lower graph shows the relative uncertainties and residuals. The inset shows an example of the Rabi-flopping experiment at a light shift of 477(1) Hz, from which Ω is deduced.

With the previously obtained experimental values, the matrix element for the E3 transition of Yb^+ is determined as

$$|M| = 2.62(7) \times 10^{-37} \text{ Jm/V}.$$

From the matrix element, the rate of spontaneous decay from the excited to the ground state and thereby the lifetime of the excited state can be calculated [53, 83, 161]. In collaboration with colleagues of the institute “Fundamental physics for metrology” at PTB, a relation between the experimental value of the matrix element and the decay rate for the E3 transition in Yb^+ has been obtained, from which the radiative lifetime of the $\text{Yb}^+ \ ^2\text{F}_{7/2}$ state is determined as

$$\tau_{\text{Yb}^+(^2\text{F}_{7/2})} = 49.8(2.5) \times 10^6 \text{ s},$$

corresponding to 1.58(8) years [152]. This yields a natural linewidth of the E3 transition of

$$\gamma_{\text{Yb}^+(\text{E3})} = \frac{1}{\tau_{\text{Yb}^+(^2\text{F}_{7/2})}} = 2\pi \times 3.20(16) \text{ nHz}. \quad (4.12)$$

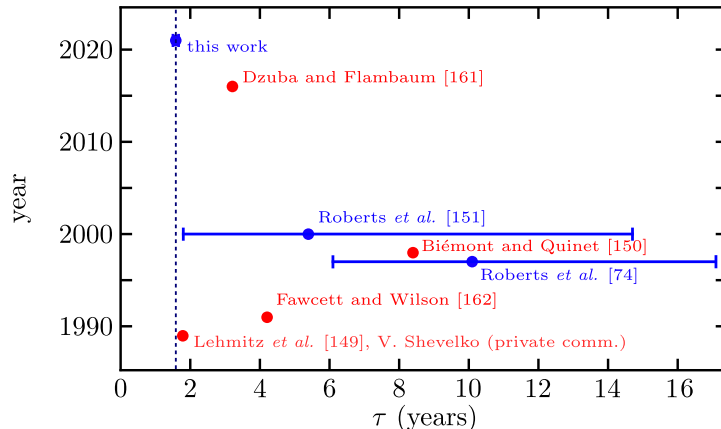


Figure 4.10: **Overview of the reported values for the natural lifetime of the $\text{Yb}^+ \ ^2\text{F}_{7/2}$ state.** Blue points mark experimental results [74, 151], red points theoretical predictions [149, 150, 161, 162].

The measured value is compared with previous experimental results and theoretical predictions in figure 4.10. It should be noted that the $^2\text{F}_{7/2}$ state is quenched in the experimental setups by the excitation of repumping transitions through thermal radiation and by background gas collisions, yielding an effective lifetime of about one hour as discussed in detail in section 2.3.9.

4.5 Excitation of the E3 transition using twisted light

For all measurements presented so far, laser beams with Gaussian beam profiles and the fundamental transverse mode TEM_{00} are employed to excite the ion. In this case, the wavefront approximates a plane wave for the well-localized atom. Within this section, beams with higher-order transverse modes are discussed for the excitation of the E3 transition. In particular, Laguerre-Gaussian modes LG_{lp} with cylindrical symmetry around the beam propagation axis z are investigated, with azimuthal index l and radial index p . While the LG_{00} mode is identical to the fundamental Gaussian mode, Laguerre-Gaussian beams with $l > 0$ feature photons that carry orbital angular momentum (OAM) in addition to the spin angular momentum (SAM). The projection of OAM on the propagation direction of the photons is specified by m_l . In the transverse plane, a light field carrying OAM exhibits a helical phase front and the far-field inten-

sity features an annular pattern with vanishing on-axis field amplitude, giving it the name twisted, vortex or doughnut beam.

Twisted light is used for a variety of applications in atomic physics [163, 164], including the transfer of OAM to Bose-Einstein condensates [165, 166], trapping of particles [167], and storing of quantum information [168]. Vortex beams can also be employed to modify the selection rules for the excitation of an atomic transition as demonstrated for the ${}^2S_{1/2} \rightarrow {}^2D_{5/2}$ electric quadrupole transition in a ${}^{40}\text{Ca}^+$ ion [169]. In such a single-ion experiment, the particle can be precisely positioned within the beam profile. Placing the ion in the dark center of the beam permits the suppression of parasitic light shifts. Good agreement between the experimental results and theoretical calculations for the modified selection rules has been obtained [170–172].

The theory has been extended to excitation of higher-order multipole transitions with twisted light [173], which can be compared to experimental results on the excitation of the E3 transition in Yb^+ with different types of vortex beams. Such a comparison tests the fundamental atomic properties of the electric octupole transition and adds to the comprehension of twisted photons interacting with atoms. Additionally, the E3 transition is a promising candidate for future applications of vortex beams, as twisted light offers the potential of significantly reducing ac Stark shifts.

4.5.1 Generation of vortex beams

Vortex beams are typically produced from a fundamental Gaussian mode profile with an optical element such as a spiral phase plate [174], a vortex retarder [175], a holographic phase plate [176], or a digital micromirror device [177]. For the following experiments, the first two elements are used:

Spiral phase plate. A glass substrate with the thickness incremented helically around the center is called a spiral phase plate (SPP). It induces a spiraling change in the plane wavefront to create a vortex beam. The size of the increment determines the OAM of the beam. The polarization of the light is preserved. One SPP² is used to create $\text{LG}_{10}(m_l = 1)$,

²The spiral phase plate V-467-20-1 from vortex photonics has been chosen: <https://www.vortex-photonics.de/vortex-lenses-spiral-phase-plates.html> (accessed September 7, 2021).

two consecutive SPPs are used to produce $\text{LG}_{20}(m_l = 2)$ beams. Their far-field intensity profiles are visualized in figure 4.11.

Vortex retarder. A half-wave retarder with uniform thickness across the clear aperture and a rotating fast axis is called a vortex retarder (VR). Incoming linearly polarized plane wave light is converted into twisted light with a distinct polarization pattern. In the following, vortex beams with radial ($\text{LG}_{10}(\text{rad})$) and azimuthal ($\text{LG}_{10}(\text{az})$) polarization are investigated³ as depicted in figure 4.11. They do not have a well-defined OAM projection m_l but can be regarded as a linear combination of two twisted beams with $m_l = \mp 1$ and SAM projection $\lambda = \pm 1$ [173].

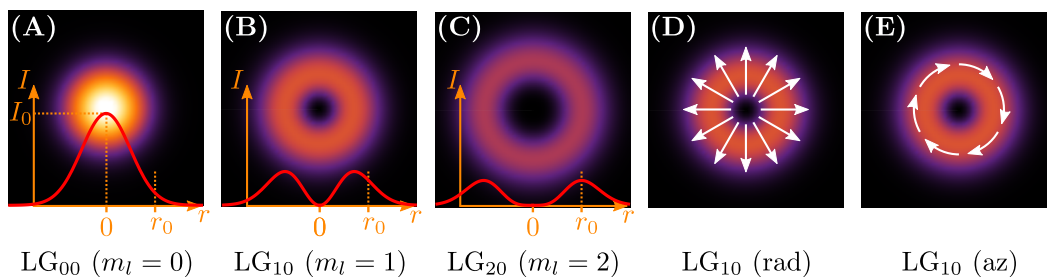


Figure 4.11: **Calculated far-field intensity patterns of Laguerre-Gaussian modes.** (A)–(C) From the fundamental Gaussian mode shown in (A), beams with well-defined OAM projection $m_l > 0$ can be produced by a spiraling phase plate. The red graphs show the 1D intensity profile through the beam center, with I_0 the maximum intensity and r_0 the beam radius of the LG_{00} mode. The polarization remains unchanged by the transformation. (D)–(E) From a LG_{00} mode with linear polarization, a vortex retarder produces beams with radial (rad) and azimuthal (az) polarization as illustrated by the white arrows.

For the excitation of the E3 transition with twisted light, the beam needs to be tightly focused to achieve an excitation rate comparable to the plane wave case at similar beam power. This puts high demands on the setup for good pointing stability and little optical aberrations of the beam. A compact setup has been devised to guide the light from the optical fiber output to the ion, as shown in figure 4.12: The LG_{00} beam at the fiber output is collimated with a lens to a Gaussian beam diameter of about 15 mm. Its linear polarization can be rotated with a $\lambda/2$ wave plate. OAM is induced to the wavefront by

³The customized vortex retarder WPV10L-467-SP from Thorlabs Inc. has been chosen: https://www.thorlabs.com/newgrouppage9.cfm?objectgroup_id=9098 (accessed September 7, 2021).

employing different types of vortex plates. The beam is guided through a one inch tube and focused by an objective⁴ that features a numerical aperture of 0.28 and is placed directly in front of the vacuum viewport. At the opposite side of the vacuum chamber, a beat signal with respect to a reference beam is used for active phase stabilization of the probe light, in analogy to the setup discussed in section 2.4.2. The optical setup is mounted on a motorized linear xyz stage that is positioned with sub-micrometer accuracy using additional sensors⁵.

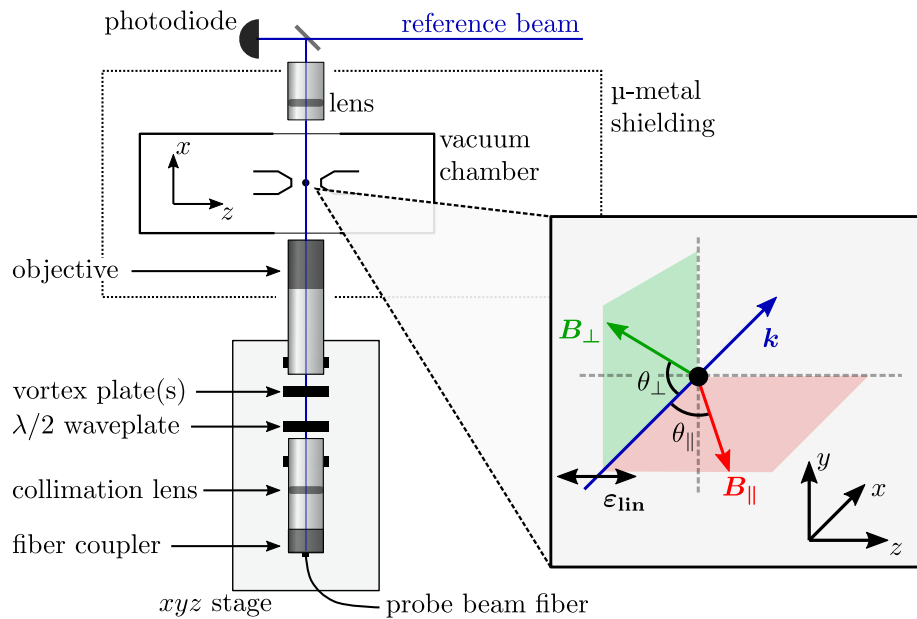


Figure 4.12: **Setup for the Yb^+ excitation with twisted light.** The probe light is fiber-guided to the optical table. After inducing orbital angular momentum with the vortex plate(s), an objective placed close to the vacuum chamber is employed to focus the beam onto the ion. The optical elements are mounted on a motorized xyz stage to displace the beam with respect to the atom. A beat signal generated between probe and reference beam is used to actively phase stabilize the probe light. The magnetic field vector B_{\parallel} (B_{\perp}) shown in the inset in red (green) is only moved in the xz -plane (xy -plane) and the angle with respect to the beam propagation vector k is given by θ_{\parallel} (θ_{\perp}). If twisted light with linear polarization is employed, the polarization vector ϵ_{lin} is oriented along the z axis.

⁴A Mitutoyo plan apochromat objective with $10\times$ magnification, a numerical aperture of 0.28, a working distance of 34 mm and a wavelength range of 436 nm to 656 nm is used.

⁵Axial probes GT21 from TESA Technology have been chosen: https://tesatechnology.com/en-gb/products/palpeurs-de-mesure/palpeurs-axiaux-standards/standard-probes-gt21-%C2%B1-1-mm,-4,-3-mm-bolt-travel_p47267.htm (accessed September 7, 2021).

Two-dimensional profiles of the vortex intensity at the ion position are assessed from measurements of the light shift on the E2 transition caused by the vortex beam, with the beam displaced along y and z using the motorized actuators of the linear stage. To position the ion in the focus, the linear stage is moved along the x axis. Profiles are shown for an $\text{LG}_{20}(m_l = 2)$ and an $\text{LG}_{10}(\text{rad})$ beam in figure 4.13. They feature a radius of the ring of maximum intensity of $r_{\text{tw}} = 1.5(1) \mu\text{m}$ and $r_{\text{tw}} = 1.6(1) \mu\text{m}$, respectively. Both beams exhibit optical aberrations such as a tilt, but in the vicinity of the beam center the expected intensity profiles of the Laguerre-Gaussian modes are found. For the $\text{LG}_{10}(\text{rad})$ beam, the on-axis field amplitude is not vanishing, which can be explained by an admixture of the LG_{00} mode of about 4 %, i.e. the fundamental Gaussian mode is not completely converted into the twisted light mode by the vortex retarder.

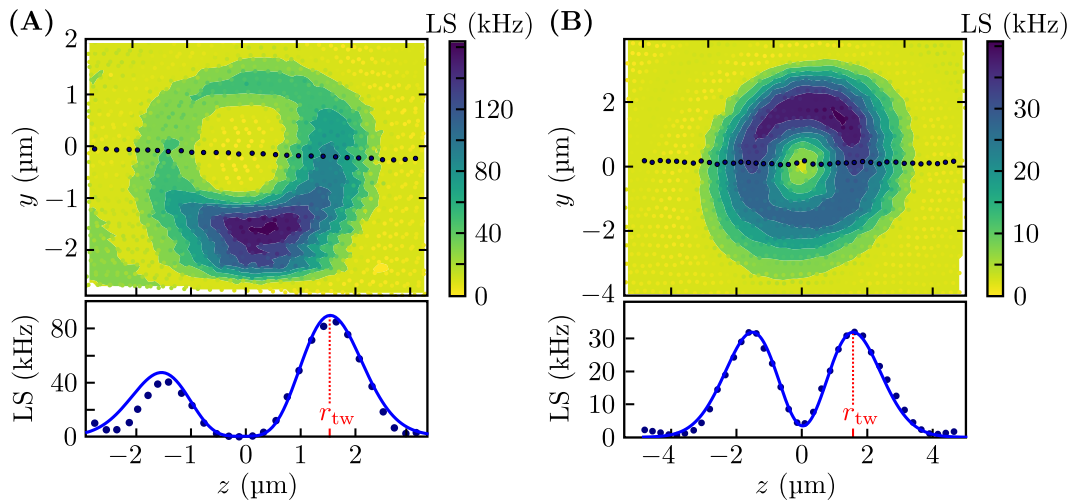


Figure 4.13: **Profiles of the light shift on the E2 transition induced by the vortex beam**, i.e. the vortex beam intensity pattern at the ion position. As the most dominant optical aberration, both profiles exhibit a tilt. The intensity along the lines marked by the blue dots are shown below. The blue lines are obtained from calculations [178]. The radius of the ring of maximum intensity is given by r_{tw} . (A) Intensity profile of an $\text{LG}_{20}(m_l = 2)$ beam with $r_{\text{tw}} = 1.5(1) \mu\text{m}$. (B) Intensity profile of an $\text{LG}_{10}(\text{rad})$ beam with $r_{\text{tw}} = 1.6(1) \mu\text{m}$. For the calculated blue curve, an admixture of 4 % of the LG_{00} mode is taken into account that leads to a non-vanishing field amplitude at the beam center.

4.5.2 Light shift suppression

With the vortex beam characterized at the ion position, excitation of the E3 transition can be investigated. Since the ion is placed in the dark center of the beam, a suppression of the light shift $\Delta\nu_{\text{LS}}$ is expected. For plane wave excitation, the dependence between light shift $\Delta\nu_{\text{LS}}^{\text{pl}}$ and Rabi frequency Ω has been determined in section 4.4:

$$\Delta\nu_{\text{LS}}^{\text{pl}} = \xi_{\text{LS}}\Omega^2, \quad (4.13)$$

with $\xi_{\text{LS}} = 0.033(1)/\text{Hz}$. A light shift suppression factor for the twisted beam can be defined by

$$S_{\text{LS}} = \frac{\Delta\nu_{\text{LS}}^{\text{pl}}}{\Delta\nu_{\text{LS}}^{\text{tw}}} = \frac{\xi_{\text{LS}}\Omega^2}{\Delta\nu_{\text{LS}}^{\text{tw}}}. \quad (4.14)$$

Detuning scans and Rabi-flopping experiments are performed for different types of twisted light. The largest suppression is found for an $\text{LG}_{20}(m_l = 2)$ beam with light shift $\Delta\nu_{\text{LS}}^{\text{tw}} = 36(1)$ Hz for a Rabi frequency $\Omega = 2\pi \times 11.5(2)$ Hz as shown in figure 4.14. This corresponds to a light shift suppression factor of

$$S_{\text{LS}} = 4.8(2),$$

i.e. about a fivefold reduction of the light shift compared to plane wave excitation. The suppression is limited by residual electromagnetic fields at the beam center, for example due to optical aberrations and pointing instabilities, both related to the optical setup. Furthermore, the ion samples a region of nonzero electromagnetic field since it is not a point-like object but exhibits a finite spatial spread, as discussed for the ground state wave packet in section 1.4.1. From a mean quantum number $\bar{n} \approx 8$ as derived in section 2.3.4, a spatial spread $\sigma_{\text{spread}} \approx 105$ nm is estimated. A spread of $\sigma_{\text{spread}} = 100$ nm, used in the calculations of the next subsection, yields good agreement between theory and experimental results. It should be noted that the loss of coherence observed for the Rabi oscillations in figure 4.14 (B) could be attributed to a mean quantum number $\bar{n} \approx 25$ for the employed trap depth with $\omega_x \approx 2\pi \times 780$ kHz. However, calculations with the corresponding spatial spread of $\sigma_{\text{spread}} \approx 314$ nm are not consistent with experiments, and a degradation of Doppler cooling with respect to the experiments performed in section 2.3.4 is not expected. Therefore, the

loss of coherence in the Rabi oscillations is attributed to limitations in the coherence of the laser beam.

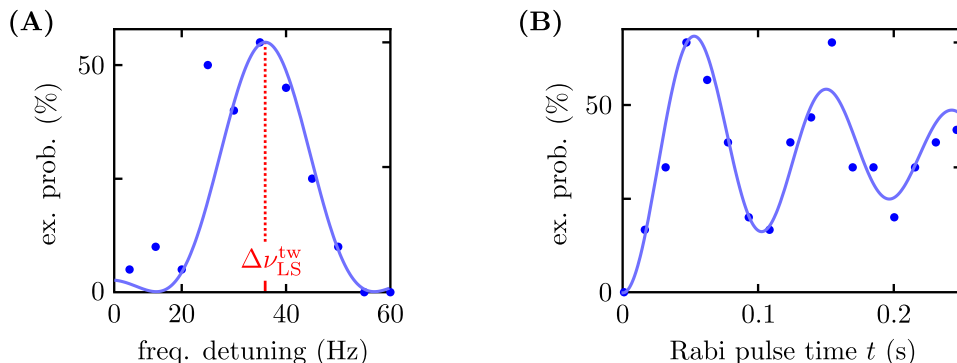


Figure 4.14: **Light shift suppression with an $\text{LG}_{20}(m_l = 2)$ beam.** (A) Detuning scan to assess the light shift $\Delta\nu_{\text{LS}}^{\text{tw}} = 36(1)$ Hz. (B) Rabi-flopping experiment to assess the Rabi frequency $\Omega = 2\pi \times 11.5(2)$ Hz. The light shift is reduced by about a factor of five compared to plane wave excitation.

4.5.3 Angular dependence of the excitation probability

In order to better understand the interaction of the E3 transition with twisted light, the excitation probability in dependence of the magnetic field angle and the polarization is investigated. The results are compared to theory [173] for different types of Laguerre-Gaussian beams that are listed in table 4.3. A digital servo stabilizes the clock laser frequency to the E3 transition and the excitation probability on resonance is measured. For one measurement, multiple such servos are employed for different magnetic field orientations with respect to the beam propagation vector \mathbf{k} , as defined in figure 4.12: A measurement is either conducted with the magnetic field placed in the xz -plane (shown in the figure in red) at different angles θ_{\parallel} . Alternatively, the measurement is performed with the magnetic field vector in the xy -plane (shown in the figure in green) at different angles θ_{\perp} . An additional servo probing the E2 transition keeps track of the light shift to ensure that the ion remains in the beam center. Thereby, the pointing stability of the vortex beam is monitored. Drifts of the beam position of about 100 nm/hour are observed that are attributed to temperature fluctuations in the laboratory. For vortex beams with linear polarization ϵ_{lin} , the polarization is aligned with the xz -plane.

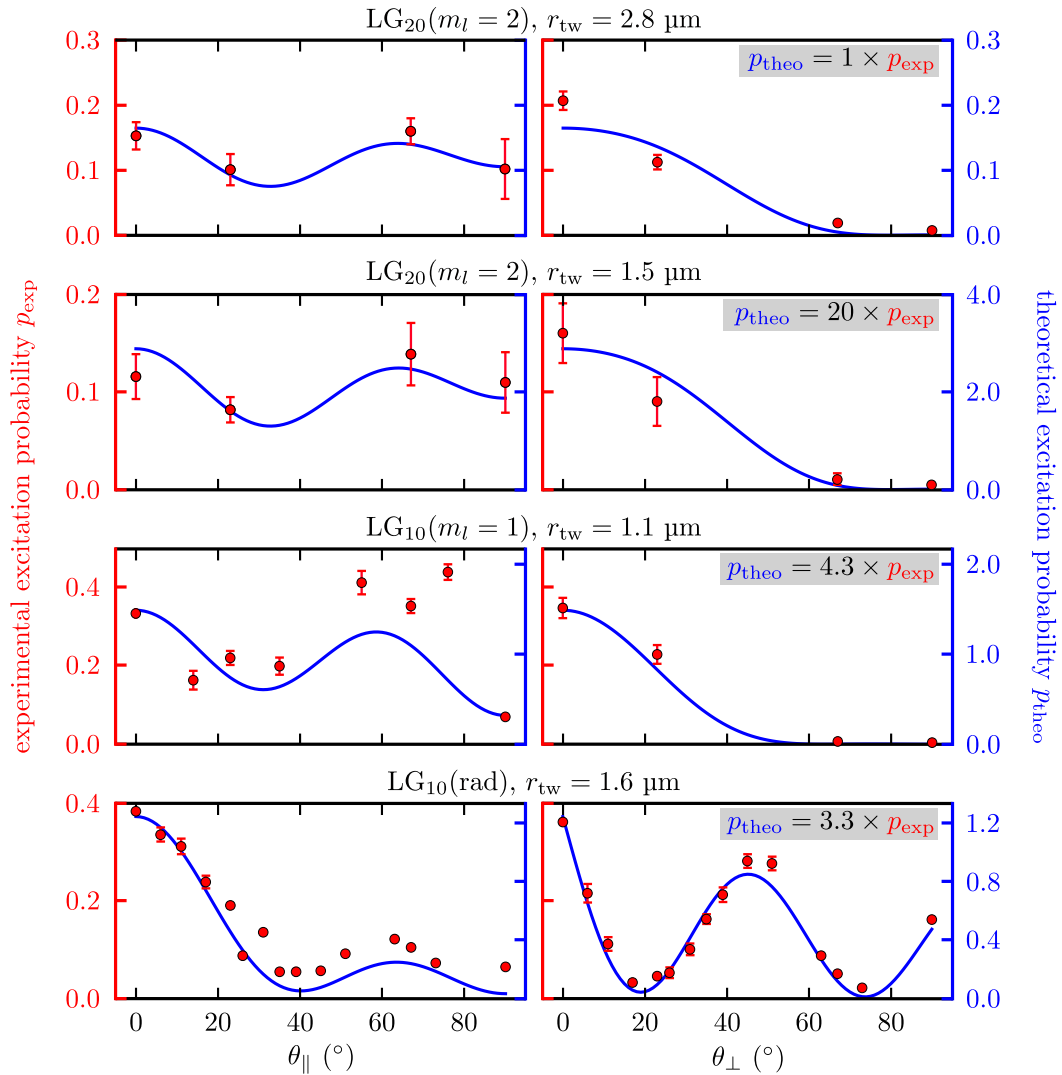


Figure 4.15: **Angular dependence of excitation probability** for the Laguerre-Gaussian beams presented in table 4.3. For each of the beams, the dependence on the magnetic field orientation as defined in figure 4.12 is shown, characterized by the two angles θ_{\parallel} and θ_{\perp} with respect to the beam propagation vector. The red points are the experimental data, given with statistical uncertainties. The blue curves are obtained from theory [178], calculated using the experimental parameters given in table 4.3 and an ion spatial spread $\sigma_{\text{spread}} = 100$ nm. While a good qualitative agreement is found, there is a varying discrepancy in the scaling for the different beams. The scaling is given for each beam in a gray box. For the $\text{LG}_{10}(\text{rad})$ mode, identical curves for the two angles would be expected. However, an admixture of 4 % of the LG_{00} mode, discussed in figure 4.13, lifts the degeneracy. No data is shown for the $\text{LG}_{10}(\text{az})$ beam as the excitation probability is too low to perform clock operation. This is in agreement with theory, which predicts a vanishing transition rate for all magnetic field orientations for the azimuthally polarized beam.

vortex mode	vortex plate(s)	r_{tw} (μm)	P (mW)	t_{pulse} (ms)
LG ₂₀ ($m_l = 2$)	2× SPP	2.8(1)	10.0(3)	50
LG ₂₀ ($m_l = 2$)	2× SPP	1.5(1)	6.5(3)	40
LG ₁₀ ($m_l = 1$)	SPP	1.1(1)	0.20(2)	30
LG ₁₀ (rad)	VR	1.6(1)	0.20(3)	30
LG ₁₀ (az)	VR	2.0(1)	7.9(3)	50

Table 4.3: **Experimental parameters of the vortex beams** employed for the assessment of the angular dependence of the excitation probability. The radius of the ring of maximum intensity is given by r_{tw} . To generate the vortex beams, spiral phase plates (SPPs) and vortex retarder (VR) are used.

The experimentally assessed excitation probabilities are compared to theory as shown in figure 4.15. The blue theoretical curves are calculated [178] using the experimental parameters in table 4.3 and an ion spatial spread of $\sigma_{\text{spread}} = 100$ nm. The magnetic field dependence is in good agreement, however, there are discrepancies in the scaling between experiment and theory, which is still an open point of discussion.

For the LG₁₀(rad) mode with radial polarization, symmetry in the plane orthogonal to beam propagation vector would be expected. However, the admixture of the LG₀₀ beam of 4 %, already discussed in figure 4.13, lifts the degeneracy and results in different dependencies of the transition strength for θ_{\parallel} and θ_{\perp} . For the LG₁₀(az) mode, no data is shown as the excitation probability is too low to perform clock operation. This is in agreement with theory, which predicts a vanishing transition rate for all magnetic field orientations for the azimuthally polarized beam.

The proof-of-principle experiment for the excitation of an electric octupole transition with twisted light confirms theoretical predictions to a large extent. It has been shown that vortex beams provide an additional parameter to tune the interaction of the ion with an electromagnetic field. Moreover, suppression of the light shift has been demonstrated, which is currently under good control employing advanced interrogation schemes such as Rabi-controlled hyper-Ramsey spectroscopy, but might also be dealt with using twisted light in the future. Further investigations of vortex beams require an optical setup that is more rigid and exhibits less optical aberrations in order to reduce limitations due to pointing instabilities and residual electromagnetic fields.

Chapter 5

Summary and outlook

In this thesis, advances of the $^{171}\text{Yb}^+$ single-ion clocks at PTB have been reported, that are employed for high-precision spectroscopy. Several frequency comparisons with both the $^2\text{S}_{1/2} \rightarrow ^2\text{D}_{3/2}$ electric quadrupole (E2) and the $^2\text{S}_{1/2} \rightarrow ^2\text{F}_{7/2}$ electric octupole (E3) transition of the $^{171}\text{Yb}^+$ ion have been presented and their evaluation in terms of searches for new physics discussed: The frequencies of the Yb1(E3) and the Yb2(E3) clocks show an agreement within their combined fractional uncertainty of 4.2×10^{-18} . An analysis of the data for a potential Lorentz violation in the electron sector has improved previous limits by about two orders of magnitude. The relative uncertainty of the E3/E2 transition frequency ratio has been reduced by one order of magnitude to 3.4×10^{-17} . The electric octupole transition frequency has been measured with two caesium fountains at PTB with 80 mHz uncertainty, representing the most accurate value for an optical frequency to date. From the E3/E2 transition frequency ratio and the absolute measurements of the E3 transition frequency, the constraints on temporal variations of the fine structure constant and the proton-to-electron mass ratio have been tightened by factors of about 20 and 2, respectively. The first direct measurement of the frequency ratio of the $^{171}\text{Yb}^+$ E3 transition and the ^{87}Sr lattice clock transition has been discussed, yielding one of the most accurate frequency ratios between different clock species, with a fractional uncertainty of 2.5×10^{-17} . Clock operation on a microwave transition involving the hyperfine levels of the Yb^+ excited clock state $^2\text{F}_{7/2}$ has been demonstrated, which can be employed for tests of local Lorentz invariance.

Performing frequency comparisons for the search of new physics is an ongoing project. In particular the analysis of a frequency ratio with respect to temporal drifts of fundamental constants improves as the time span between individual measurements increases. In combination with reduced systematic uncertainties of the clocks, regular frequency comparisons will enable more rigorous tests of fundamental physics in the next few years. The current robustness of clock operation results in a high availability for frequency measurements. The E2 and E3 transition frequencies are endorsed by the International Committee for Weights and Measures as secondary representations of the SI second, and contributions of the Yb^+ clocks at PTB to the calibration of international atomic time (TAI) are pursued. Reports for such contributions are in preparation.

The development and characterization of the new Yb^+ single-ion clock system Yb3 at PTB has been presented. It features gold-coated endcap electrodes, low-loss fused silica insulators, and vacuum viewports with large optical access. In comparison with the previous trap version Yb1, improvements such as a reduction of the ion motional heating rate by a factor of 25 have been demonstrated. Varying dc electric stray fields of Yb3 are currently limiting clock comparisons to the low 10^{-17} relative uncertainty level and shall be avoided with an interchange of the physics package. Subsequently, a reduction of main contributions to the systematic uncertainty and more precise frequency comparisons of the E3 transition at the low 10^{-18} level will be pursued.

The clock instabilities of Yb1 and Yb3 have been investigated. A significant contribution to the local oscillator phase noise at the ion position has been attributed to unstabilized free paths of the probe laser beam on the optical table. A novel phase stabilization scheme improves the laser stability at the ion position by about a factor of two to a flicker frequency noise of $\sigma_{\text{FF}} = 3.4(3) \times 10^{-16}$. At the same time, the scheme suppresses shifts related to phase deviations such as AOM chirps. A single servo instability of $7.8 \times 10^{-16} / \sqrt{\tau/s}$ for Rabi pulses of 500 ms length has been obtained. The reduction of unstabilized laser paths is further pursued to better exploit the stability of the single-crystal silicon cavity, to which the clock laser is stabilized.

Relevant atomic parameters of both the E2 and E3 transition have been investigated in detail. Measurements of the electric quadrupole moments $\Theta(^2D_{3/2}) = 1.95(1)ea_0^2$ and $\Theta(^2F_{7/2}) = -0.0297ea_0^2$ are used to obtain the sensitivity of the transitions to electric field gradients. A zero-crossing point of the scalar differential polarizability of the E3 transition has been measured at 681.2(5) nm, which represents a magic wavelength. A relation between transition strength and laser intensity has been obtained for the E3 transition, from which a natural lifetime of the excited $^2F_{7/2}$ state of 1.58(7) years has been inferred. More precise knowledge of the atomic parameters enables the reduction of systematic uncertainties. For instance, the static scalar differential polarizability $\Delta\alpha_S^{\text{dc}}$ of both the E2 and E3 transition can be measured with high precision using infrared laser radiation and a $^{88}\text{Sr}^+$ ion with low uncertainty in $\Delta\alpha_S^{\text{dc}}$ as a sensor for laser intensity. Thereby, a reduction of the blackbody radiation shift uncertainty by an order of magnitude is expected.

Novel interrogation methods have been discussed, facilitating the control or suppression of specific systematic frequency shifts: A coherent suppression method for tensorial shifts has been presented, relying on a rotation of the magnetic field vector during the dark time of a Ramsey sequence. A suppression of the electric quadrupole shift by a factor of 260 has been demonstrated. With autobalanced Ramsey spectroscopy another interrogation scheme has been introduced, which provides immunity to aberrations of the pulses in a Ramsey sequence. Finally, the excitation of an electric octupole transition with twisted light, i.e. with the ion placed in the dark center of a Laguerre-Gaussian beam featuring orbital angular momentum, has been demonstrated for the first time. The ac Stark shift present during plane wave excitation has been reduced by about a factor of five for excitation with twisted light. Further improvements are expected with reduced optical aberrations and a better pointing stability of the beam.

The single-ion clocks based on the endcap trap design at PTB are complemented by another system currently taken into operation: a multi-species clock employing a linear trap for the simultaneous trapping of $^{171}\text{Yb}^+$ and $^{88}\text{Sr}^+$. At the current status, coherent excitation of the E2 transitions of both ion species

has been achieved, and clock operation with a single Sr ion has been performed. With a multi-species clock, novel interrogation methods can be devised. The Sr^+ E2 transition at 674 nm is close to the magic wavelength of the Yb^+ E3 transition and can be used for sideband cooling, facilitating ground-state cooling of a Sr^+ ancillary ion during clock operation on the Yb^+ ion. Thereby, interrogation of the sympathetically cooled Yb^+ ion is not compromised by motional heating, as both ions remain close to the motional ground state during the Ramsey dark time.

To conclude, the thesis has provided an insight into recent advances with single-ion Yb^+ clocks. However, this covers merely a tiny fraction of the progress in the field of high-precision measurements. Regarding only the atomic clock sector, vast advances are reported with many different systems such as highly-charged ions, nuclear clock transitions, multi-ion strings or atoms in optical lattices. As the network of atomic clocks is constantly expanded and the performance of these systems is continuously improved, frequency comparisons between atomic clocks will carry on to provide significant contributions to searches for new physics in the future.

Bibliography

- [1] *Unsere Masseinheiten: das Internationale Einheitensystem (SI)*, Switzerland: Federal Institute of Metrology (METAS), 2019.
- [2] M. Battaglieri, A. Belloni, A. Chou, P. Cushman, B. Echenard, R. Essig, *et al.*, arXiv:1707.04591v1 (2017).
- [3] F. Arute, K. Arya, R. Babbush, D. Bacon, J. C. Bardin, R. Barends, *et al.*, Nature **574**, 505 (2019).
- [4] E. Gibney, Nature **587**, 342 (2020).
- [5] L. Essen, Vistas Astron. **11**, 45 (1969).
- [6] M. Planck, Ann. Phys. **306**, 69 (1900).
- [7] T. Fortier and E. Baumann, Commun. Phys. **2** (2019).
- [8] M. Knoop, N. Madsen, and R. C. Thompson, *Trapped charged particles, A graduate textbook with problems and solutions*, Advanced textbooks in physics (World Scientific Publishing Europe Ltd and World Scientific Publishing Co. Pte. Ltd, London and Singapore, 2016).
- [9] U. Sterr, T. Legero, T. Kessler, H. Schnatz, G. Grosche, O. Terra, *et al.*, in Time and Frequency Metrology II, edited by T. Ido and D. T. Reid, SPIE Proceedings (2009), 74310A.
- [10] W. M. Itano, J. C. Bergquist, J. J. Bollinger, J. M. Gilligan, D. J. Heinzen, F. L. Moore, *et al.*, Phys. Rev. A **47**, 3554 (1993).
- [11] A. D. Ludlow, M. M. Boyd, J. Ye, E. Peik, and P. O. Schmidt, Rev. Mod. Phys. **87**, 637 (2015).
- [12] K. Beloy, M. I. Bodine, T. Bothwell, S. M. Brewer, S. L. Bromley, J.-S. Chen, *et al.*, Nature **591**, 564 (2021).

- [13] M. Takamoto, I. Ushijima, N. Ohmae, T. Yahagi, K. Kokado, H. Shinkai, *et al.*, *Nat. Photonics* **14**, 411 (2020).
- [14] R. Schwarz, S. Dörscher, A. Al-Masoudi, E. Benkler, T. Legero, U. Sterr, *et al.*, *Phys. Rev. Research* **2**, 033242 (2020).
- [15] J. Lodewyck, S. Bilicki, E. Bookjans, J.-L. Robyr, C. Shi, G. Vallet, *et al.*, *Metrologia* **53**, 1123 (2016).
- [16] R. Hobson, W. Bowden, A. Vianello, A. Silva, C. F. A. Baynham, H. S. Margolis, *et al.*, *Metrologia* **57**, 065026 (2020).
- [17] H. Kim, M.-S. Heo, W.-K. Lee, C. Y. Park, H.-G. Hong, S.-W. Hwang, *et al.*, *Jpn. J. Appl. Phys.* **56**, 050302 (2017).
- [18] Q. Gao, M. Zhou, C. Han, S. Li, S. Zhang, Y. Yao, *et al.*, *Sci. Rep.* **8**, 8022 (2018).
- [19] M. Pizzocaro, F. Bregolin, P. Barbieri, B. Rauf, F. Levi, and D. Calonico, *Metrologia* **57**, 035007 (2020).
- [20] S. Hannig, L. Pelzer, N. Scharnhorst, J. Kramer, M. Stepanova, Z. T. Xu, *et al.*, *Rev. Sci. Instrum.* **90**, 053204 (2019).
- [21] P. Dubé, J. E. Bernard, and M. Gertszov, *Metrologia* **54**, 290 (2017).
- [22] C. F. A. Baynham, R. M. Godun, J. M. Jones, S. A. King, P. B. R. Nisbet-Jones, F. Baynes, *et al.*, *J. Mod. Opt.* **65**, 585 (2018).
- [23] R. Kaewuam, T. R. Tan, K. J. Arnold, S. R. Chanu, Z. Zhang, and M. D. Barrett, *Phys. Rev. Lett* **124**, 083202 (2020).
- [24] N. Ohtsubo, Y. Li, K. Matsubara, N. Nemitz, H. Hachisu, T. Ido, *et al.*, *Hyperfine Interact.* **240**, 39 (2019).
- [25] R. Tyumenev, M. Favier, S. Bilicki, E. Bookjans, R. Le Targat, J. Lodewyck, *et al.*, *New J. Phys.* **18**, 113002 (2016).
- [26] A. P. Kulosa, D. Fim, K. H. Zipfel, S. Rühmann, S. Sauer, N. Jha, *et al.*, *Phys. Rev. Lett.* **115**, 240801 (2015).
- [27] Y. Huang, H. Guan, P. Liu, W. Bian, L. Ma, K. Liang, *et al.*, *Phys. Rev. Lett.* **116**, 013001 (2016).
- [28] A. Golovizin, E. Fedorova, D. Tregubov, D. Sukachev, K. Khabarova, V. Sorokin, *et al.*, *Nat. Commun.* **10**, 1724 (2019).

- [29] C. W. Chou, D. B. Hume, T. Rosenband, and D. J. Wineland, *Science* **329**, 1630 (2010).
- [30] B. J. Bloom, T. L. Nicholson, J. R. Williams, S. L. Campbell, M. Bishof, X. Zhang, *et al.*, *Nature* **506**, 71 (2014).
- [31] I. Ushijima, M. Takamoto, M. Das, T. Ohkubo, and H. Katori, *Nat. Photonics* **9**, 185 (2015).
- [32] T. L. Nicholson, S. L. Campbell, R. B. Hutson, G. E. Marti, B. J. Bloom, R. L. McNally, *et al.*, *Nat. Commun.* **6**, 6896 (2015).
- [33] N. Huntemann, C. Sanner, B. Lipphardt, Chr. Tamm, and E. Peik, *Phys. Rev. Lett.* **116**, 063001 (2016).
- [34] N. Nemitz, T. Ohkubo, M. Takamoto, I. Ushijima, M. Das, N. Ohmae, *et al.*, *Nat. Photonics* **10**, 258 (2016).
- [35] W. F. McGrew, X. Zhang, R. J. Fasano, S. A. Schaeffer, K. Beloy, D. Nicolodi, *et al.*, *Nature* **564**, 87 (2018).
- [36] C. Sanner, N. Huntemann, R. Lange, Chr. Tamm, E. Peik, M. S. Safronova, *et al.*, *Nature* **567**, 204 (2019).
- [37] S. M. Brewer, J.-S. Chen, A. M. Hankin, E. R. Clements, C. W. Chou, D. J. Wineland, *et al.*, *Phys. Rev. Lett.* **123**, 033201 (2019).
- [38] S. Dörscher, N. Huntemann, R. Schwarz, R. Lange, E. Benkler, B. Lipphardt, *et al.*, *Metrologia* **58**, 015005 (2021).
- [39] R. Lange, N. Huntemann, J. M. Rahm, C. Sanner, H. Shao, B. Lipphardt, *et al.*, *Phys. Rev. Lett.* **126**, 011102 (2021).
- [40] D. J. Wineland, C. Monroe, W. M. Itano, D. Leibfried, B. E. King, and D. M. Meekhof, *J. Res. Natl. Inst. Stand. Technol.* **103**, 259 (1998).
- [41] C. F. Roos, *Controlling the quantum state of trapped ions*, PhD Thesis, Leopold-Franzens-Universität Innsbruck, 2000.
- [42] N. Huntemann, *High-Accuracy Optical Clock Based on the Octupole Transition in $^{171}\text{Yb}^+$* , PhD Thesis, Gottfried Wilhelm Leibniz Universität Hannover, 2014.
- [43] W. Paul, *Rev. Mod. Phys.* **62**, 531 (1990).

- [44] M. Abdel-Hafiz, P. Ablewski, A. Al-Masoudi, H. Á. Martínez, P. Balling, G. Barwood, *et al.*, arXiv:1906.11495v2 (2019).
- [45] É. Mathieu, *J. Math. Pures Appl.*, 137 (1868).
- [46] D. J. Bate, K. Dholakia, R. C. Thompson, and D. C. Wilson, *J. Mod. Opt.* **39**, 305 (1992).
- [47] B. Stein, *Contributions to a Yb⁺ single-ion optical frequency standard*, PhD Thesis, Gottfried Wilhelm Leibniz Universität Hannover, 2010.
- [48] D. J. Berkeland, J. D. Miller, J. C. Bergquist, W. M. Itano, and D. J. Wineland, *J. Appl. Phys.* **83**, 5025 (1998).
- [49] C. Blockley, D. F. Walls, and H. Risken, *Europhys. Lett.* **17**, 509 (1992).
- [50] D. J. Wineland, C. Monroe, W. M. Itano, B. E. King, D. Leibfried, D. M. Meekhof, *et al.*, *Fortschr. Phys.* **46**, 363 (1998).
- [51] H. G. Dehmelt, *Bull. Am. Phys. Soc.* **20**, 60 (1975).
- [52] S. Bernadotte, A. J. Atkins, and C. R. Jacob, *J. Chem. Phys.* **137**, 204106 (2012).
- [53] M. Fox, *Quantum optics, An introduction*, Vol. 15, Oxford master series in physics. Atomic, optical, and laser physics (Oxford University Press, Oxford and New York, 2007).
- [54] T. R. Tan, R. Kaewuam, K. J. Arnold, S. R. Chanu, Z. Zhang, M. S. Safronova, *et al.*, *Phys. Rev. Lett.* **123**, 063201 (2019).
- [55] E. R. Clements, M. E. Kim, K. Cui, A. M. Hankin, S. M. Brewer, J. Valencia, *et al.*, *Phys. Rev. Lett.* **125**, 243602 (2020).
- [56] R. W. P. Drever, J. L. Hall, F. V. Kowalski, J. Hough, G. M. Ford, A. J. Munley, *et al.*, *Appl. Phys. B* **31**, 97 (1983).
- [57] E. D. Black, *Am. J. Phys.* **69**, 79 (2001).
- [58] D. G. Matei, T. Legero, S. Häfner, C. Grebing, R. Weyrich, W. Zhang, *et al.*, *Phys. Rev. Lett.* **118**, 263202 (2017).
- [59] Chr. Tamm, S. Weyers, B. Lipphardt, and E. Peik, *Phys. Rev. A* **80**, 043403 (2009).
- [60] N. F. Ramsey, *Phys. Rev.* **76**, 996 (1949).

- [61] N. F. Ramsey, *Phys. Rev.* **78**, 695 (1950).
- [62] V. I. Yudin, A. V. Taichenachev, C. W. Oates, Z. W. Barber, N. D. Lemke, A. D. Ludlow, *et al.*, *Phys. Rev. A* **82**, 011804 (2010).
- [63] N. Huntemann, B. Lipphardt, M. Okhapkin, Chr. Tamm, E. Peik, A. V. Taichenachev, *et al.*, *Phys. Rev. Lett.* **109**, 213002 (2012).
- [64] W. W. Chow, S. W. Koch, and M. Sargent, *Semiconductor-Laser Physics* (Springer Berlin Heidelberg, Berlin, Heidelberg, 1994).
- [65] R. Lange, N. Huntemann, C. Sanner, H. Shao, B. Lipphardt, Chr. Tamm, *et al.*, *Phys. Rev. Lett.* **125**, 143201 (2020).
- [66] C. Sanner, N. Huntemann, R. Lange, Chr. Tamm, and E. Peik, *Phys. Rev. Lett.* **120**, 053602 (2018).
- [67] R. Blatt, H. Schnatz, and G. Werth, *Phys. Rev. Lett.* **48**, 1601 (1982).
- [68] R. Blatt, R. Casdorff, V. Enders, W. Neuhauser, and P. E. Toschek, “New Frequency Standards Based on Yb^+ ”, in *Frequency standards and metrology*, edited by A. de Marchi (Springer Berlin Heidelberg, Berlin, Heidelberg, 1989), pp. 306–311.
- [69] A. S. Bell, P. Gill, H. A. Klein, A. P. Levick, Chr. Tamm, and D. Schnier, *Phys. Rev. A* **44**, R20 (1991).
- [70] S. Olmschenk, D. Hayes, D. N. Matsukevich, P. Maunz, D. L. Moehring, K. C. Younge, *et al.*, *Phys. Rev. A* **80**, 022502 (2009).
- [71] T. M. Hoang, Y.-Y. Jau, R. Overstreet, and P. D. D. Schwindt, *Phys. Rev. A* **101**, 022705 (2020).
- [72] Chr. Tamm, D. Engelke, and V. Böhner, *Phys. Rev. A* **61**, 612 (2000).
- [73] Chr. Tamm, N. Huntemann, B. Lipphardt, V. Gerginov, N. Nemitz, M. Kazda, *et al.*, *Phys. Rev. A* **89**, 023820 (2014).
- [74] M. Roberts, P. Taylor, G. P. Barwood, P. Gill, H. A. Klein, and W. R. C. Rowley, *Phys. Rev. Lett.* **78**, 1876 (1997).
- [75] N. Huntemann, M. Okhapkin, B. Lipphardt, S. Weyers, Chr. Tamm, and E. Peik, *Phys. Rev. Lett.* **108**, 090801 (2012).
- [76] N. Yu and L. Maleki, *Phys. Rev. A* **61**, 022507 (2000).

- [77] V. V. Flambaum and V. A. Dzuba, *Can. J. Phys.* **87**, 25 (2009).
- [78] M. Brownnutt, M. Kumph, P. Rabl, and R. Blatt, *Rev. Mod. Phys.* **87**, 1419 (2015).
- [79] G. Poulsen, Y. Miroshnychenko, and M. Drewsen, *Phys. Rev. A* **86**, 051402(R) (2012).
- [80] J. Keller, T. Burgermeister, D. Kalincev, A. Didier, A. P. Kulosa, T. Nordmann, *et al.*, *Phys. Rev. A* **99**, 013405 (2019).
- [81] J. R. P. Angel and P. G. H. Sandars, *Proc. R. Soc. Lond. A* **305**, 125 (1968).
- [82] W. M. Itano, *J. Res. Natl. Inst. Stand. Technol.* **105**, 829 (2000).
- [83] I. I. Sobelman, *Atomic Spectra and Radiative Transitions*, Second Edition, Vol. 12, Springer Series on Atoms+Plasmas (Springer, Berlin and Heidelberg, 1992).
- [84] S. G. Porsev and A. Derevianko, *Phys. Rev. A* **74**, 020502(R) (2006).
- [85] C. F. A. Baynham, E. A. Curtis, R. M. Godun, J. M. Jones, P. B. R. Nisbet-Jones, P. E. G. Baird, *et al.*, arXiv:1801.10134v2 (2018).
- [86] P. Dubé, A. A. Madej, M. Tibbo, and J. E. Bernard, *Phys. Rev. Lett.* **112**, 173002 (2014).
- [87] M. Doležal, P. Balling, P. B. R. Nisbet-Jones, S. A. King, J. M. Jones, H. A. Klein, *et al.*, *Metrologia* **52**, 842 (2015).
- [88] K. J. Arnold, R. Kaewuam, A. Roy, T. R. Tan, and M. D. Barrett, *Nat. Commun.* **9**, 1650 (2018).
- [89] Y. Huang, H. Guan, M. Zeng, L. Tang, and K. Gao, *Phys. Rev. A* **99**, 011401(R) (2019).
- [90] J. Keller, H. L. Partner, T. Burgermeister, and T. E. Mehlstäubler, *J. Appl. Phys.* **118**, 104501 (2015).
- [91] R. M. Godun, P. B. R. Nisbet-Jones, J. M. Jones, S. A. King, L. A. M. Johnson, H. S. Margolis, *et al.*, *Phys. Rev. Lett.* **113**, 210801 (2014).
- [92] H. C. J. Gan, G. Maslennikov, K.-W. Tseng, T. R. Tan, R. Kaewuam, K. J. Arnold, *et al.*, *Phys. Rev. A* **98**, 032514 (2018).

- [93] S. H. Autler and C. H. Townes, *Phys. Rev.* **100**, 703 (1955).
- [94] C. N. Cohen-Tannoudji, “The Autler-Townes Effect Revisited”, in *Amazing light*, edited by R. Y. Chiao (Springer New York, New York, NY, 1996), pp. 109–123.
- [95] T. Schneider, *Optical Frequency Standard with a Single $^{171}\text{Yb}^+$ Ion*, PhD Thesis, Gottfried Wilhelm Leibniz Universität Hannover, 2005.
- [96] K. V. P. Latha, C. Sur, R. K. Chaudhuri, B. P. Das, and D. Mukherjee, *Phys. Rev. A* **76**, 062508 (2007).
- [97] D. K. Nandy and B. K. Sahoo, *Phys. Rev. A* **90**, 050503(R) (2014).
- [98] N. Batra, B. K. Sahoo, and S. De, *Chinese Phys. B* **25**, 113703 (2016).
- [99] X.-T. Guo, Y.-M. Yu, Y. Liu, and B.-B. Suo, *Chinese Phys. B* **29**, 053101 (2020).
- [100] S. G. Porsev, M. S. Safronova, and M. G. Kozlov, *Phys. Rev. A* **86**, 022504 (2012).
- [101] T. Rosenband, D. B. Hume, P. O. Schmidt, C. W. Chou, A. Brusch, L. Lorini, *et al.*, *Science* **319**, 1808 (2008).
- [102] A. M. Hankin, E. R. Clements, Y. Huang, S. M. Brewer, J.-S. Chen, C. W. Chou, *et al.*, *Phys. Rev. A* **100**, 033419 (2019).
- [103] D. Kleppner, R. F. C. Vessot, and N. F. Ramsey, *Astrophys. Space Sci.* **6**, 13 (1970).
- [104] A. Einstein, *Ann. Phys.* **340**, 898 (1911).
- [105] S. Herrmann, F. Finke, M. LülF, O. Kichakova, D. Puetzfeld, D. Knickmann, *et al.*, *Phys. Rev. Lett.* **121**, 231102 (2018).
- [106] P. Delva, N. Puchades, E. Schönemann, F. Dilssner, C. Courde, S. Bertone, *et al.*, *Phys. Rev. Lett.* **121**, 231101 (2018).
- [107] T. E. Mehlstäubler, G. Grosche, C. Lisdat, P. O. Schmidt, and H. Denker, *Rep. Prog. Phys.* **81**, 064401 (2018).
- [108] L. Timmen, *Absolute gravity measurements at station PTB Braunschweig "alte Gleiswaage" with the Hannover gravity meter FG5X-220 in June 2018*, Internal report, Institute of Geodesy, Leibniz University Hanover, 2018.

- [109] H. Denker, N. Lindenthal, L. Timmen, and S. Weyers, *Report on leveling and GNSS results for stations on the PTB campus*, Internal report, Institute of Geodesy, Leibniz University Hanover, PTB, 2014.
- [110] H. Denker, L. Timmen, C. Voigt, S. Weyers, E. Peik, H. S. Margolis, *et al.*, *J. Geod.* **92**, 487 (2018).
- [111] M. Kazda, V. Gerginov, N. Huntemann, B. Lipphardt, and S. Weyers, *IEEE Trans. Ultrason. Ferroelectr. Freq. Control* **63**, 970 (2016).
- [112] S. Falke, H. Schnatz, J. S. R. V. Winfred, T. Middelman, S. Vogt, S. Weyers, *et al.*, *Metrologia* **48**, 399 (2011).
- [113] S. Weyers, V. Gerginov, M. Kazda, J. Rahm, B. Lipphardt, G. Dobrev, *et al.*, *Metrologia* **55**, 789 (2018).
- [114] M. K. Gaillard, P. D. Grannis, and F. J. Sciulli, *Rev. Mod. Phys.* **71**, S96 (1999).
- [115] M. S. Safronova, D. Budker, D. DeMille, D. F. J. Kimball, A. Derevianko, and C. W. Clark, *Rev. Mod. Phys.* **90**, 025008 (2018).
- [116] C. M. Will, *Living Rev. Relativ.* **17**, 4 (2014).
- [117] G. M. Tino, L. Cacciapuoti, S. Capozziello, G. Lambiase, and F. Sorrentino, *Prog. Part. Nucl. Phys.* **112**, 103772 (2020).
- [118] D. Colladay and V. A. Kostelecký, *Phys. Rev. D* **55**, 6760 (1997).
- [119] D. Colladay and V. A. Kostelecký, *Phys. Rev. D* **58**, 116002 (1998).
- [120] V. A. Kostelecký and N. Russell, *Rev. Mod. Phys.* **83**, 11 (2011).
- [121] M. A. Hohensee, N. Leifer, D. Budker, C. Harabati, V. A. Dzuba, and V. V. Flambaum, *Phys. Rev. Lett.* **111**, 050401 (2013).
- [122] T. Pruttivarasin, M. Ramm, S. G. Porsev, I. I. Tupitsyn, M. S. Safronova, M. A. Hohensee, *et al.*, *Nature* **517**, 592 (2015).
- [123] E. Megidish, J. Broz, N. Greene, and H. Häffner, *Phys. Rev. Lett.* **122**, 123605 (2019).
- [124] C. J. A. P. Martins, *Rep. Prog. Phys.* **80**, 126902 (2017).
- [125] M. R. Wilczynska, J. K. Webb, M. Bainbridge, J. D. Barrow, S. E. I. Bosman, R. F. Carswell, *et al.*, *Sci. Adv.* **6**, eaay9672 (2020).

- [126] B. M. Roberts, P. Delva, A. Al-Masoudi, A. Amy-Klein, C. Bærentsen, C. F. A. Baynham, *et al.*, *New J. Phys.* **22**, 093010 (2020).
- [127] H. A. Fürst, C.-H. Yeh, D. Kalincev, A. P. Kulosa, L. S. Dreissen, R. Lange, *et al.*, *Phys. Rev. Lett.* **125**, 163001 (2020).
- [128] V. A. Dzuba, V. V. Flambaum, M. S. Safronova, S. G. Porsev, T. Pruttivarasin, M. A. Hohensee, *et al.*, *Nat. Phys.* **12**, 465 (2016).
- [129] V. A. Kostelecký and J. D. Tasson, *Phys. Rev. D* **83**, 016013 (2011).
- [130] V. A. Kostelecký and C. D. Lane, *Phys. Rev. D* **60**, 116010 (1999).
- [131] B. Altschul, *Phys. Rev. D* **74**, 083003 (2006).
- [132] N. Huntemann, B. Lipphardt, Chr. Tamm, V. Gerginov, S. Weyers, and E. Peik, *Phys. Rev. Lett.* **113**, 210802 (2014).
- [133] V. A. Dzuba and V. V. Flambaum, *Phys. Rev. D* **95**, 015019 (2017).
- [134] Bureau International des Poids et Mesures, *Le Système international d'unités / The International System of Units*, 9th edition 2019 [SRS: Appendix 2, for $^{171}\text{Yb}^+(\text{E}3)$: https://www.bipm.org/utils/common/pdf/mep/171Yb+_642THz_2015.pdf].
- [135] F. Riedel, A. Al-Masoudi, E. Benkler, S. Dörscher, V. Gerginov, C. Grebing, *et al.*, *Metrologia* **57**, 045005 (2020).
- [136] C. Grebing, A. Al-Masoudi, S. Dörscher, S. Häfner, V. Gerginov, S. Weyers, *et al.*, *Optica* **3**, 563 (2016).
- [137] J. Leute, N. Huntemann, B. Lipphardt, Chr. Tamm, P. B. R. Nisbet-Jones, S. A. King, *et al.*, *IEEE Trans. Ultrason. Ferroelectr. Freq. Control* **63**, 981 (2016).
- [138] T. H. Dinh, A. Dunning, V. A. Dzuba, and V. V. Flambaum, *Phys. Rev. A* **79**, 054102 (2009).
- [139] V. V. Flambaum, *Phys. Rev. Lett.* **97**, 092502 (2006).
- [140] J. Guéna, M. Abgrall, D. Rovera, P. Rosenbusch, M. E. Tobar, Ph. Laurent, *et al.*, *Phys. Rev. Lett.* **109**, 080801 (2012).
- [141] W. F. McGrew, X. Zhang, H. Leopardi, R. J. Fasano, D. Nicolodi, K. Beloy, *et al.*, *Optica* **6**, 448 (2019).

- [142] N. Ashby, T. E. Parker, and B. R. Patla, *Nat. Phys.* **14**, 822 (2018).
- [143] N. Nemitz, T. Gotoh, F. Nakagawa, H. Ito, Y. Hanado, T. Ido, *et al.*, *Metrologia* **58**, 025006 (2021).
- [144] R. Shaniv, R. Ozeri, M. S. Safronova, S. G. Porsev, V. A. Dzuba, V. V. Flambaum, *et al.*, *Phys. Rev. Lett.* **120**, 103202 (2018).
- [145] E. R. Andrew, *Int. Rev. Phys. Chem.* **1**, 195 (1981).
- [146] H. S. Margolis, G. Huang, G. P. Barwood, S. N. Lea, H. A. Klein, W. R. C. Rowley, *et al.*, *Phys. Rev. A* **67**, 032501 (2003).
- [147] M. M. Boyd, *High Precision Spectroscopy of Strontium in an Optical Lattice: Towards a New Standard for Frequency and Time*, PhD Thesis, JILA, 2007.
- [148] N. Akerman, N. Navon, S. Kotler, Y. Glickman, and R. Ozeri, *New J. Phys.* **17**, 113060 (2015).
- [149] H. Lehmitz, J. Hattendorf-Ledwoch, R. Blatt, and H. Harde, *Phys. Rev. Lett.* **62**, 2108 (1989).
- [150] E. Biémont and P. Quinet, *Phys. Rev. Lett.* **81**, 3345 (1998).
- [151] M. Roberts, P. Taylor, G. P. Barwood, W. R. C. Rowley, and P. Gill, *Phys. Rev. A* **62**, 020501 (2000).
- [152] R. Lange, A. A. Peshkov, N. Huntemann, Chr. Tamm, A. Surzhykov, and E. Peik, arXiv:2107.11229 (2021).
- [153] E. Peik, G. Hollemann, and H. Walther, *Phys. Rev. A* **49**, 402 (1994).
- [154] V. Letchumanan, M. A. Wilson, P. Gill, and A. G. Sinclair, *Phys. Rev. A* **72**, 012509 (2005).
- [155] T. Rosenband, P. O. Schmidt, D. B. Hume, W. M. Itano, T. M. Fortier, J. E. Stalnaker, *et al.*, *Phys. Rev. Lett.* **98**, 220801 (2007).
- [156] H. Shao, Y. Huang, H. Guan, C. Li, T. Shi, and K. Gao, *Phys. Rev. A* **95**, 053415 (2017).
- [157] M. Yasuda and H. Katori, *Phys. Rev. Lett.* **92**, 153004 (2004).
- [158] B. B. Jensen, H. Ming, P. G. Westergaard, K. Gunnarsson, M. H. Madsen, A. Brusch, *et al.*, *Phys. Rev. Lett.* **107**, 113001 (2011).

- [159] S. S. Hodgman, R. G. Dall, L. J. Byron, K. G. H. Baldwin, S. J. Buckman, and A. G. Truscott, *Phys. Rev. Lett.* **103**, 053002 (2009).
- [160] N. Huntemann, *private communication*, Physikalisch-Technische Bundesanstalt, 2021.
- [161] V. A. Dzuba and V. V. Flambaum, *Phys. Rev. A* **93**, 052517 (2016).
- [162] B. Fawcett and M. Wilson, *At. Data Nucl. Data Tables* **47**, 241 (1991).
- [163] S. Franke-Arnold, *Phil. Trans. R. Soc. A* **375**, 20150435 (2017).
- [164] Y. Shen, X. Wang, Z. Xie, C. Min, X. Fu, Q. Liu, *et al.*, *Light Sci. Appl.* **8**, 90 (2019).
- [165] J. F. S. Brachmann, W. S. Bakr, J. Gillen, A. Peng, and M. Greiner, *Opt. Express* **19**, 12984 (2011).
- [166] A. Ramanathan, K. C. Wright, S. R. Muniz, M. Zelan, W. T. Hill, C. J. Lobb, *et al.*, *Phys. Rev. Lett.* **106**, 130401 (2011).
- [167] T. Kuga, Y. Torii, N. Shiokawa, T. Hirano, Y. Shimizu, and H. Sasada, *Phys. Rev. Lett.* **78**, 4713 (1997).
- [168] L. Veissier, A. Nicolas, L. Giner, D. Maxein, A. S. Sheremet, E. Giacobino, *et al.*, *Opt. Lett.* **38**, 712 (2013).
- [169] C. T. Schmiegelow, J. Schulz, H. Kaufmann, T. Ruster, U. G. Poschinger, and F. Schmidt-Kaler, *Nat. Commun.* **7**, 12998 (2016).
- [170] G. F. Quinteiro, F. Schmidt-Kaler, and C. T. Schmiegelow, *Phys. Rev. Lett.* **119**, 253203 (2017).
- [171] A. A. Peshkov, D. Seipt, A. Surzhykov, and S. Fritzsche, *Phys. Rev. A* **96**, 023407 (2017).
- [172] A. Afanasev, C. E. Carlson, C. T. Schmiegelow, J. Schulz, F. Schmidt-Kaler, and M. Solyanik, *New J. Phys.* **20**, 023032 (2018).
- [173] S. A.-L. Schulz, A. A. Peshkov, R. A. Müller, R. Lange, N. Huntemann, Chr. Tamm, *et al.*, *Phys. Rev. A* **102**, 012812 (2020).
- [174] M. Massari, G. Ruffato, M. Gintoli, F. Ricci, and F. Romanato, *Appl. Opt.* **54**, 4077 (2015).
- [175] S. C. McEldowney, D. M. Shemo, R. A. Chipman, and P. K. Smith, *Opt. Lett.* **33**, 134 (2008).

- [176] M. Padgett, J. Courtial, and L. Allen, *Phys. Today* **57**, 35 (2004).
- [177] Y. Chen, Z.-X. Fang, Y.-X. Ren, L. Gong, and R.-D. Lu, *Appl. Opt.* **54**, 8030 (2015).
- [178] A. A. Peshkov, *private communication*, Physikalisch-Technische Bundesanstalt (institute: Fundamental physics for metrology), 2021.

Danksagung

Am Aufbau von Yb1 hängt ein kleiner, mittlerweile deutlich in die Jahre gekommener Zettel mit folgender Aufschrift:

Ytterbium, from Ytterby, Sweden; discovered 1907
This element is still little more than
a laboratory curiosity.

Aus: A Periodic Table of
The Elements,
Time-Life Books 1987

Anfang der 90er Jahre wurden die ersten Ergebnisse zu gefangenen und lasergekühlten Yb-Ionen an der PTB veröffentlicht. Rund 25 Jahre später, im Frühjahr 2016, titelte die PTB in einer Pressemitteilung

“Die Ytterbium-Einzelionenuhr der PTB ist weltweit
die genaueste Uhr ihrer Art [...]”.

Im September desselben Jahres wurde ich als Doktorand in das Yb-Team aufgenommen, in dem sich über die vielen Jahre ein ausgezeichnet organisiertes und mit reichhaltiger Expertise ausgestattetes Arbeitsumfeld etabliert hat. Ich habe größten Respekt vor der hervorragenden Arbeit, die die Kollegen an der PTB seit Jahrzehnten leisten. Dadurch wurde mir die Möglichkeit gegeben, die Welt der Quantenphysik auf allerhöchstem Niveau kennenzulernen und eigene wissenschaftlich relevante Beiträge zu liefern. Einige der Kollegen, die die Atomuhren der PTB über viele Jahre mitentwickelt haben, haben mich auch während der gesamten Doktorandenzeit begleitet und unterstützt.

Allen voran gilt mein Dank Nils Huntemann, der mich als hilfsbereiter und tatkräftiger Mentor bei den Arbeiten inner- und außerhalb des Labor unterstützt hat und bei dem ich zu jeder Zeit ein offenes Ohr für Diskussionen gefunden habe. Seiner Leidenschaft, Neugier und seinem immerwährenden Engagement ist maßgeblich der aktuelle Fortschritt und die Weiterentwicklung der Yb⁺ Uhren zu verdanken.

Ebenso möchte ich mich bei Christian Sanner bedanken, der in den ersten zwei Jahren meiner Doktorandenzeit einen großen Beitrag zur Betreuung geleistet hat. Zu Beginn noch nicht tiefgreifend mit der Quantenphysik vertraut, fühlte ich mich gerade in dieser Anfangszeit regelmäßig starker mentaler Beschleunigung ausgesetzt und Christian stellte einen fast schon meditativen Ruhepol zum Sortieren der Gedanken bereit.

Bei Fragen rund um Elektronik steht Burghard Lipphardt mit Rat und Tat zur Seite. Er trägt maßgeblich dazu bei, dass unser Labor auf eine große Bandbreite exzellenter Elektronikkomponenten aus eigener Fertigung zurückgreifen kann. Gleichzeitig ist er auch noch der “beste Frequenzkammdompteur der Welt”¹ und ermöglicht uns damit unter anderem die Durchführung diverser Uhrenvergleiche. Die Zusammenarbeit im Labor ist stets eine wahre Freude!

Bei Ekkehard Peik bedanke ich mich für die großartige Unterstützung, insbesondere für die Betreuung der Doktorarbeit, und die vielfältigen Möglichkeiten, die mir als Doktorand offenstanden. Dazu gehört der Besuch vieler hochkarätiger Konferenzen oder die Teilnahme an renommierten Workshops wie der Winter School in Les Houches.

Christian Tamm ist von Anfang an bei der Entwicklung der optischen Yb-Frequenznormale an der PTB dabei und hat das Fundament für die heutigen Arbeiten geliefert. Bei Fragen habe ich bei Christian stets eine offene Tür und gute Ratschläge vorgefunden. Auch die kritischen Rückmeldungen und Diskussionen zu Abstracts und Veröffentlichungen waren immer sehr hilfreich!

Die Yb-Arbeitsgruppe ist in den letzten Jahren einem fortlaufenden Wandel unterzogen und einige Kollegen haben mich ein Stück auf dem Weg meiner Doktorandenzeit begleitet. Ich bedanke mich bei Moustafa Abdel Hafiz, Hu Shao, Jiehang Zhang, Melina Filzinger und Martin Steinel für die gute Zusam-

¹Christian Sanner, private comm.

menarbeit innerhalb und außerhalb des Labors.

Ohne die großartige Unterstützung des Fachbereichs wären die Yb-Uhren heute nicht so gut aufgestellt, wie sie es sind. Danke an die zahlreichen unterstützenden Arbeiten im Bereich Elektronik von vielen wertgeschätzten Kollegen, darunter Christof Hellmann, Niklas Kuhrmeyer, Marius Jathe und Andreas Hoppmann. Gleichmaßen gilt dieser Dank den Kollegen der mechanischen Werkstatt, Martin Menzel und Thomas Leder.

Während meiner Doktorandenzeit habe ich mit vielen Kollegen aus anderen Arbeitsgruppen zusammengearbeitet und gute Ergebnisse sind aus diesen Kollaborationen entstanden. Ich bedanke mich insbesondere bei den Kollegen der Caesium-Fontänen, Stefan Weyers und Johannes Rahm, den Kollegen vom Thorium, Johannes Thielking, David-Marcel Meier und Maksim Okhapkin, den Kollegen der Strontium-Gitteruhr, Roman Schwarz, Sören Dörscher und Christian Lisdat, den Kollegen, die uns das Signal der Silizium-Cavity zur Verfügung stellen, Thomas Legero, Erik Benkler und Uwe Sterr, den Theorie-Kollegen für die gemeinsamen Arbeiten zur Oktupol-Anregung, Anton Peshkov, Sabrina Schulz und Andrey Surzhykov, sowie den zahlreichen Kollegen im QUEST Institut.

Weiterhin bedanke ich mich für die freundliche Unterstützung und die Betreuung der Doktorarbeit bei Piet Schmidt und für die bereitwillige Übernahme der Gutachtertätigkeit bei Hartmut Häffner.

Ganz klar, diese Dissertation ist das Ergebnis eines großen Gemeinschaftsprojekts, in das die Erfahrung, das Wissen und die Leidenschaft vieler wertgeschätzter Kollegen eingeflossen sind. Doch vollständiger Fokus auf Wissenschaft und Forschung sind nur möglich, wenn einem das private Umfeld mit Rat, Tat und Verständnis zur Seite steht. Ich bedanke mich bei meiner gesamten Familie dafür, dass sie der Work-Life-Balance immer wieder auf der Life-Seite Gewicht verliehen und mir über all die Jahre meiner wissenschaftlichen Ausbildung Rückhalt und Kraft gegeben haben. Meine größte Dankbarkeit gilt dabei meinen Eltern, Annett und Jürgen Lange:

Ohne eure uneingeschränkte Unterstützung in allen Lebenslagen wäre diese Arbeit nie entstanden – Danke!

Curriculum Vitae

Personal data

Name	Richard Lange
Born	September 4, 1991 in Berlin, Germany
Nationality	German

Educational Background and Work Experience

07/2021 – today	Postdoctoral researcher at Physikalisch-Technische Bundesanstalt, Braunschweig, Germany
09/2016 – 06/2021	Ph.D. student at Physikalisch-Technische Bundesanstalt, Braunschweig, Germany
10/2014 – 08/2016	Study of physics (M.Sc.) at Freie Universität Berlin, Germany; Master thesis at the German Aerospace Center in Stuttgart, Germany (10/2015 – 08/2016)
10/2011 – 08/2014	Study of physics (B.Sc.) at Freie Universität Berlin, Germany; Bachelor thesis at Volkswagen AG in Wolfsburg, Germany (03/2014 – 08/2014)
08/2002 – 06/2011	Grammar school “Bertha-von-Suttner-Oberschule” in Berlin, Germany (Graduation: general higher education entrance qualification)
08/1998 – 06/2002	Primary school “Platanengrundschule” in Berlin, Germany

Awards and honors

09/2020	Helmholtz Prize (category “fundamental research”)
04/2019	Student poster award of the Joint Conference of the IEEE IFCS & EFTF
09/2010	Student award of the German Physical Society

Publications

- *Autobalanced Ramsey Spectroscopy*,
C. Sanner, N. Huntemann, R. Lange, Chr. Tamm, E. Peik, Phys. Rev. Lett. **120**, 053602 (2018), DOI: 10.1103/PhysRevLett.120.053602
- *Laser-controlled adaptive optics for beam quality improvements in a multi-pass thin-disk amplifier*,
R. Lange, D. Kolbe, Optics Letters **43**, 3453 (2018),
DOI: 10.1364/OL.43.003453
- *Optical clock comparison for Lorentz symmetry testing*,
C. Sanner, N. Huntemann, R. Lange, Chr. Tamm, E. Peik, M. S. Safro-
nova, S. G. Porsev, Nature **567**, 204 (2019),
DOI: 10.1038/s41586-019-0972-2
- *Generalized excitation of atomic multipole transitions by twisted light modes*,
S. A.-L. Schulz, A. A. Peshkov, R. A. Müller, R. Lange, N. Huntemann,
Chr. Tamm, E. Peik, A. Surzhykov, Phys. Rev. A **102**, 012812 (2020),
DOI: 10.1103/PhysRevA.102.012812
- *Search for transient variations of the fine structure constant and dark matter using fiber-linked optical atomic clocks*,
B. M. Roberts, P. Delva, A. Al-Masoudi, A. Amy-Klein, C. Bærentsen,
C. F. A. Baynham, E. Benkler, S. Bilicki, S. Bize, W. Bowden, J. Calvert,
V. Cambier, E. Cantin, E. A. Curtis, S. Dörscher, M. Favier, F. Frank,
P. Gill, R. M. Godun, G. Grosche, C. Guo, A. Hees, I. R. Hill, R. Hob-
son, N. Huntemann, J. Kronjäger, S. Koke, A. Kuhl, R. Lange, T. Le-
gero, B. Lipphardt, C. Lisdat, J. Lodewyck, O. Lopez, H. S. Margolis,

H. Álvarez-Martínez, F. Meynadier, F. Ozimek, E. Peik, P.-E. Pottie, N. Quintin, C. Sanner, L. de Sarlo, M. Schioppo, R. Schwarz, A. Silva, U. Sterr, Chr. Tamm, R. Le Targat, P. Tuckey, G. Vallet, T. Waterholter, D. Xu, P. Wolf, *New J. Phys.*, **22**, 093010 (2020),

DOI: 10.1088/1367-2630/abaace

- *Coherent Suppression of Tensor Frequency Shifts through Magnetic Field Rotation,*

R. Lange, N. Huntemann, C. Sanner, H. Shao, B. Lipphardt, Chr. Tamm, E. Peik, *Phys. Rev. Lett.* **125**, 143201 (2020),

DOI: 10.1103/PhysRevLett.125.143201

- *Coherent Excitation of the Highly Forbidden Electric Octupole Transition in $^{172}\text{Yb}^+$,*

H. A. Fürst, C.-H. Yeh, D. Kalincev, A. P. Kulosa, L. S. Dreissen, R. Lange, E. Benkler, N. Huntemann, E. Peik, T. E. Mehlstäubler, *Phys. Rev. Lett.* **125**, 163001 (2020), DOI: 10.1103/PhysRevLett.125.163001

- *Improved Limits for Violations of Local Position Invariance from Atomic Clock Comparisons,*

R. Lange, N. Huntemann, J. M. Rahm, C. Sanner, H. Shao, B. Lipphardt, Chr. Tamm, S. Weyers, E. Peik, *Phys. Rev. Lett.* **126**, 011102 (2021),

DOI: 10.1103/PhysRevLett.126.011102

- *Optical frequency ratio of a $^{171}\text{Yb}^+$ single-ion clock and a ^{87}Sr lattice clock,*

S. Dörscher, N. Huntemann, R. Schwarz, R. Lange, E. Benkler, B. Lipphardt, U. Sterr, E. Peik, C. Lisdat, *Metrologia* **58**, 015005 (2021),

DOI: 10.1088/1681-7575/abc86f



Herausgeber:

Physikalisch-Technische Bundesanstalt
ISNI: 0000 0001 2186 1887

Presse und Öffentlichkeitsarbeit

Bundesallee 100
38116 Braunschweig

Telefon: (05 31) 592-93 21
Telefax: (05 31) 592-92 92
www.ptb.de

Vertrieb:

Fachverlag NW in der
Carl Schünemann Verlag GmbH

Zweite Schlachtpforte 7
28195 Bremen

Telefon: (04 21) 369 03-0
Telefax: (04 21) 369 03-63
www.schuenemann-verlag.de